STRUCTURAL STUDIES, ELASTIC AND PHOTOELASTIC PROPERTIES OF LEAD PHOSPHATE, BARIUM PHOSPHATE AND LEAD BARIUM PHOSPHATE GLASSES

by

Milad Rezazadeh

Submitted in partial fulfillment of the requirements
for the degree of Master of Science

at

Dalhousie University
Halifax, Nova Scotia
August 2020

Table of Contents

List of Tables . . . . **v**

List of Figures . . . . **vi**

Abstract . . . . **ix**

List of Abbreviations and Symbols Used . . . . **x**

Acknowledgements . . . . **xii**

Chapter 1 Introduction **1**

1.1 Overview 1

1.2 Thesis structure 3

Chapter 2 Background **6**

2.1 Definition of Glass 6

2.2 Structural Theories of Glass Formation 7

2.3 Role of Oxides in Glass 8

2.4 Structure of Phosphate glass 10

2.5 Binary phosphate glasses 11

2.6 Crystalline Phases 12

2.7 Elastic Properties of Glass 18
  2.7.1 Glass Topology 18
  2.7.2 Elastic modulii 19
  2.7.3 Glass Topology and Elastic Properties 21

2.8 Photoelasticity 22

2.9 The Stress-Optic Coefficient 23

2.10 Theories of Photoelasticity 25
  2.10.1 Mueller's Theory of Photoelasticity 25

2.11 Zwanziger's Empirical Model 25

Chapter 3 Experimental Techniques 27

3.1 Introduction 27

3.2 Glass preparation 27

3.3 X-ray Diffraction 29

3.4 Elemental Analysis 30
  3.4.1 Electron probe micro-analyzer 31

3.5 Density 33

3.6 Elastic Properties 34
  3.6.1 Ultrasonic Echography Method (USE) 35

3.7 Solid-state nuclear magnetic resonance (ssNMR) 36
  3.7.1 Magic Angle Spinning 36
  3.7.2 Spin Echo 38
  3.7.3 The Carr-Purcell-Meiboom-Gill (CPMG) Pulse Sequence . . . 39
  3.7.4 The WCPMG Pulse Sequence 40
  3.7.5 Ultra-wideline NMR 41

3.8 Refractive Index 41

3.9 Stress Optic Measurement 41

Chapter 4 Structural studies, elastic and photoelastic properties 44

4.1 Introduction 44

4.2 Glass preparation 44

4.3 X-ray Diffraction 44

4.4 Elemental Analysis 46

4.5 Density measurements 47

4.6 Solid-State Nuclear Magnetic Resonance 51
  4.6.1 ^{31}P Nuclear Magnetic Resonance Spectroscopy 51
  4.6.2 ^{207}Pb Nuclear Magnetic Resonance Spectroscopy 59

4.7 Elastic properties 69

4.8 Optical and Photoelastic properties 78
  4.8.1 Refractive Index Measurement 78
  4.8.2 Stress Optic Measurement 78
  4.8.3 Empirical model of photoelasticity 80

Chapter 5 Conclusions and Future Work **83**
5.1 Future Work 85
Bibliography **87**
5.2 Appendix A Copyright Permission 94

List of Tables

1.1 The nominal compositions and their abbreviated names 3

2.1 The d/N_c ratio and the sign of C 26

4.1 Mass in grams of the reagents used 45

4.2 Melting time and temperature as well as the annealing temperature in a ternary and binary glass families. 45

4.3 Comparison between experimental and nominal compositions . 47

4.4 ρ and V_m of the binary and ternary samples 47

4.5 ρ and V_m of crystalline compounds 50

4.6 ^{31}P isotropic chemical shifts and their fraction 56

4.7 Deconvolution of about all ^{207}Pb WCPMG NMR spectra 67

4.8 The glass compositions and elastic properties of all samples . . 70

4.9 The glass compositions and index of refraction 78

4.10 The glass compositions and the stress optic coefficient 80

4.11 Bond length d, cation-anion coordination number N_c, and d/N_c ratio for oxide components of glasses in this work 81

4.12 The glass compositions, predicted and experimental sign of the stress-optic coefficient 82

List of Figures

1.1 Composition diagram 4

2.1 The volume-temperature diagram for a glass and a crystal . . 7

2.2 A schematic representation of the two-dimensional crystalline vs amorphous structure 8

2.3 A schematic representation of the NBO formation through the introduction of NaO to SiO_2-Na_2O glass system 9

2.4 Phosphate tetrahedra sites 10

2.5 Crystal structure of BaP_2O_6 13

2.6 Crystal structure of $Ba_2P_2O_7$ 14

2.7 Crystal structure of PbP_2O_6 15

2.8 Crystal structure of $Pb_2P_2O_7$ 16

2.9 Crystal structure of $BaPbP_2O_7$ 17

2.10 A schematic diagram representing the physical meaning of Poisson ratio 20

3.1 Schematic of the Bragg diffraction 30

3.2 Schematic of Rowland circle 32

3.3 Schematic of Density measurement 34

3.4 MAS and Static comparision 37

3.5 Spin echo 38

3.6 CPMG pulse sequence 39

3.7 Representation of the experimental apparatus to measure C . 43

4.1 X-ray diffraction patterns of random four glasses 46

4.2 Comparison between experimental and nominal compositions . 48

4.3 V_m of all samples as a function of PbO 49

4.4 Deconvoluted ^{31}P NMR spectra of $(PbO)_{0.60}(P_2O_5)_{0.40}$ 51
4.5 Deconvoluted ^{31}P NMR spectra of $(PbO)_{0.55}(P_2O_5)_{0.45}$ 52
4.6 Deconvoluted ^{31}P NMR spectra of $(PbO)_{0.50}(P_2O_5)_{0.50}$ 52
4.7 Deconvoluted ^{31}P NMR spectra of $(PbO)_{0.40}(BaO)_{0.10}(P_2O_5)_{0.50}$ 53
4.8 Deconvoluted ^{31}P NMR spectra of $(PbO)_{0.30}(BaO)_{0.20}(P_2O_5)_{0.50}$ 53
4.9 Deconvoluted ^{31}P NMR spectra of $(PbO)_{0.20}(BaO)_{0.30}(P_2O_5)_{0.50}$ 54
4.10 Deconvoluted ^{31}P NMR spectra of $(PbO)_{0.10}(BaO)_{0.40}(P_2O_5)_{0.50}$ 54
4.11 Deconvoluted ^{31}P NMR spectra of $(BaO)_{0.50}(P_2O_5)_{0.50}$ 55
4.12 Deconvoluted ^{31}P NMR spectra of $(BaO)_{0.55}(P_2O_5)_{0.45}$ 55
4.13 ^{31}P NMR spectra of all compositions 58
4.14 Deconvoluted ^{207}Pb NMR spectra of $(PbO)_{0.60}(P_2O_5)_{0.40}$ . . . 60
4.15 Deconvoluted ^{207}Pb NMR spectra of $(PbO)_{0.55}(P_2O_5)_{0.45}$ . . . 61
4.16 Deconvoluted ^{207}Pb NMR spectra of $(PbO)_{0.50}(P_2O_5)_{0.50}$ . . . 62
4.17 Deconvoluted ^{207}Pb NMR spectra of $(PbO)_{0.40}(BaO)_{0.10}(P_2O_5)_{0.50}$ 63
4.18 Deconvoluted ^{207}Pb NMR spectra of $(PbO)_{0.30}(BaO)_{0.20}(P_2O_5)_{0.50}$ 64
4.19 Deconvoluted ^{207}Pb NMR spectra of $(PbO)_{0.20}(BaO)_{0.30}(P_2O_5)_{0.50}$ 65
4.20 Deconvoluted ^{207}Pb NMR spectra of $(PbO)_{0.10}(BaO)_{0.40}(P_2O_5)_{0.50}$ 66
4.21 The ^{207}Pb WCPMG NMR spectra for all samples containing 50% mol P_2O_5 content 68
4.22 v_L and v_T as a function of PbO content 71
4.23 Variation of elastic moduli(GPa) as a function of PbO content (mol%) in binary and ternary compositions. 72
4.24 Variation of Bulk modulus as a function of V_m 73
4.25 Variation of shear modulus G as a function V_m 74
4.26 Variation of Young's modulus E as a function of V_m 75
4.27 Variation of Poisson ratio as a function of V_m 76
4.28 Variation of Poisson ratio as a function of PbO content (mol%) in binary and ternary compositions. 77

4.29 Phase shift as a function of applied stress from all trials for $(PbO)_{0.60}(P_2O_5)_{0.40}$ glass composition 79

4.30 Variation of C as a function of PbO content 81

5.1 Permission to reproduce Figure 2.3 94

5.2 Permission to reproduce Figure 3.4 and Figure 3.7 95

Abstract

The investigation of the atomic structure of glass and its corresponding crystals not only allows us to interpret its elastic and photoelastic properties, but it also allows us to predict the properties of glass which have not been produced yet or are toxic to synthesize.

In order to find a correlation between elastic and photoelastic properties with the composition and atomic structure, a series of ternary $(PbO)_x(BaO)_{50-x}(P_2O_5)_{50}$ (x=10 to 50 mol%) as well as binary $(PbO)_x(P_2O_5)_{100-x}$ (x=50 to 60 mol%) and $(BaO)_x(P_2O_5)_{100-x}$ (x=50 to 55 mol%) compositions have been synthesized via traditional melt quenching techniques and their compositions were verified through wavelength-dispersive spectroscopy (WDS). The local environment of lead and phosphorus as well as the glass atomic structure were investigated with ^{31}P and ^{207}Pb solid-state nuclear magnetic resonance (ssNMR) spectroscopy and derived molar volume from density measurements.

The longitudinal and transverse wave velocities (v_L and v_T) were determined using Ultrasonic Echography Method (USE). The experimental density values along with the v_L and v_T were then used to calculate the elastic properties in each series of glass compositions: the longitudinal, bulk, shear, and Young's moduli as well as Poisson ratio. Refractive indices, the sign and value of stress optic coefficient (C) were measured via Abbe refractometer, PS-100 Polariscope and the Senarmont compensator method, respectively. The reliability of the empirical model of photoelasticity was tested and discussed.

List of Abbreviations and Symbols Used

B_i	Relative dielectric impermeability
C_{ijkl}	Elastic stiffness tensor
M_i	Molar mass
N_c	Cation's coordination number
T_2	the transverse, or spin-spin relaxation time
T_g	Glass transition Temperature
T_m	Melting temperature
V_f	Atomic packing density
V_m	Molar volume
Δn	Birefringence
ϵ	Strain
λ	Wavelength
ν	Poisson ratio
ρ	Density
σ	Mechanical stress, chemical shielding
τ_w	Pulse duration
υ_L	Longitudinal velocity
υ_T	Transverse velocity
BO	Bridging oxygen
C	Stress optic coefficient
CPMG	Carr-Purcell Meiboom-Gill
CSA	Chemical shift anisotropy
d	Cation-oxygen bond length
E	Young's modulus
EA	Elemental analysis
EDS	Energy-dispersive spectroscopy
EPMA	Electron probe micro-analyzer

FID	Free-induction Decay
G	Shear modulus
I	spin quantum number
K	Bulk modulus
MAS	Magic Angle Spinning
n	Refractive index
NBO	Non-bridging oxygen
P	Pressure
ssNMR	Solid-State Nuclear Magnetic Resonance
T	Temperature
USE	Ultrasonic Echography Method
V	Volume
VOCS	Variable offset cumulative spectrum
WCPMG	WURST Carr-Purcell Meiboom-Gill
WDS	Wavelength-dispersive spectroscopy
WURST	Wideband, uniform rate, smooth truncation
x	Molar fraction of additive

Acknowledgements

First and foremost, I wish to express my sincere gratitude to my supervisor Prof. Josef Zwanziger and his wife Prof. Urlike Werner-Zwanziger for their guidance and support throughout my graduate studies at Dalhousie University. Their patience, motivation as well as the opportunity they gave me to join their team and work on truly challenging and intriguing research projects, is highly appreciated.

In addition to my supervisor, I would like to thank my committee member, Prof. Mark Obrovac for his encouragement and critical suggestions.

My sincere thanks also goes to past and present members of the Zwanziger group which include Chris Sutherland, Abbey Jenkins, Dr. Alex Paterson, Dr. Mounesha Garaga Nagendrachar and Dr. Tsanka Todorova.

I wish to thank all the staff and scientists at Dalhousie who have contributions in my graduate studies: Dr. Jennifer MacDonald, Dr. Joshua Bates, Andy George, Cathy Ryan, Dan MacDonald, Mike Boutilier, Todd Carter and many others.

Last but not least, I would like to pay special thanks to my wife, my parents, as well as my sister, for their support, love, patience and encouragement throughout my life.

Chapter 1

Introduction

1.1 Overview

This dissertation describes an investigation of the atomic structure, elastic and photoelastic properties of binary $(PbO)_x(P_2O_5)_{100-x}$ (x=50 to 60 mol%) and binary $(BaO)_x(P_2O_5)_{100-x}$ (x=50 to 55 mol%) as well as ternary $(PbO)_x(BaO)_{50-x}(P_2O_5)_{50}$ (x=10 to 50 mol%) glasses, with the primary aim being to understand the effect of replacement of Pb with Ba on the aforementioned properties.

Phosphate-based oxide glasses have been studied extensively for many years for various reasons such as their low melting temperature, high thermal expansion coefficient, low glass transition temperature, high transparency, high refractive indices, high electric conductivity and low optical dispersion [1–6]. These unique functional properties make them excellent candidates in comparison to their silicate and borate counterparts for a wide range of technological applications such as: biomaterials, solid-state lasers, ionic conductors, optical fibers, radiation shield glasses and glass-to-metal sealing applications [7–11]. However, poor chemical durability and their high hygroscopic and volatile nature have long constrained their performance [6, 12]. These shortcomings are rooted in the formation of phosphoric acid when phosphorus structural units with non-bridging oxygen atoms (NBOs) are exposed to moisture [13].

There is a strong correlation between physiochemical properties and molecular-level structure of phosphate-based oxide glasses. Therefore, numerous studies have been conducted to improve the physical properties and chemical durability of phosphate glasses by introducing one or more oxides such as PbO, Al_2O_3, ZnO, Fe_2O_3, *etc* into the P_2O_5 network system [5, 14, 15].

Recent studies have revealed that PbO in lead phosphate glasses not only modifies the chemical durability, but in addition, the heavy Pb atoms give rise to high shielding properties against nuclear radiation [16]. For this reason, several studies have been conducted to probe the complexity of the lead phosphate structure and other unique properties of this particular system [1, 6, 17, 18]. Furthermore, researchers have not limited themselves to only binary lead phosphate glasses. Often other oxide additives such as Al_2O_3, WO_3, Sb_2O_3, Sm_2O_3, In_2O_3 and ZnO to lead phosphate glasses have gained their attention. This interest is rooted in the unique physical, chemical, optical and electrical properties that each of the oxides bring to this system [1, 5, 12, 14, 16, 19].

An investigation of lead-barium-aluminum phosphate glasses showed that high polarizability and a large size of Pb^{2+} and Ba^{2+} cations, result in strong bonding to NBOs in the phosphate chain which significantly improves their corrosion resistance, index of refraction, infrared performance and visible properties [5]. Moreover, lead barium phosphate glasses have been shown to have better transparency and radiation shielding in comparison to commonly used alkali lead silicate glasses which makes them excellent candidates as radiation shielding glasses [20]. It has also been proven that the substitution of BaO with PbO in $xBaO.(50-x)PbO.50P_2O_5$ glasses increases their electric conductivity which was interpreted based on different roles of Pb^{2+} and Ba^{2+} in the structure [21]. Although the incorporation of PbO and BaO can bring about unique practical properties to phosphate network, there are currently no investigations on the structure and elasticity of ternary lead barium phosphate glasses.

Zwanziger *et al.* in 2007 proposed an empirical model which can predict a photoelastic response of glass [22]. The reliability of the model was verified for binary lead phosphate and ternary lead barium phosphate glasses by Galbraith *et al.* in 2016 [23, 24]. However, due to the volatility of P_2O_5, it is essential to perform an elemental analysis to confirm the nominal composition of all phosphate-based glasses which have not been reported before. Moreover, the photoelastic properties of lead phosphate and lead barium phosphate glasses were predicted based on the low coordination number of Pb-O (3 or 4) which was not confirmed with ^{207}Pb ssNMR at that time.

Table 1.1 lists the glass nominal compositions as well as their abbreviated names which are studied in this dissertation. Figure 1.1 shows the composition diagram of the glass samples studied in this dissertation, as well as the glass forming ranges (represented by blue arrows) of the binary compositions [25, 26]. The range of compositions for ternary glasses was chosen specifically to study the effect of the replacement of Pb by Ba on properties. While Pb^{2+} and Ba^{2+} would appear superficially to have similar chemical properties, it is known that Pb^{2+} may participate in covalent bonding under some circumstances while Ba^{2+} does not. Thus the primary interest here was to hold the phosphate content of a glass constant while replacing Pb^{2+} with Ba^{2+} systematically and investigating how the properties correlated with the bonding types. The range of compositions for binary glasses was chosen to further explore the structure of binary phosphate-based glasses at high concentration of PbO and BaO content. In this dissertation we also aim to answer the following questions: a) Is there a correlation between glass structures, compositions and their elastic and photoelastic properties? and b) Is the empirical model able to predict the sign of C accurately?

Table 1.1: The nominal compositions studied in this dissertation as well as their abbreviated names.

Compositions	Short Names
$(PbO)_{60}(P_2O_5)_{40}$	60Pb40P
$(PbO)_{55}(P_2O_5)_{45}$	55Pb45P
$(PbO)_{50}(P_2O_5)_{50}$	50Pb50P
$(PbO)_{40}(BaO)_{10}(P_2O_5)_{50}$	40Pb10Ba50P
$(PbO)_{30}(BaO)_{20}(P_2O_5)_{50}$	30Pb20Ba50P
$(PbO)_{20}(BaO)_{30}(P_2O_5)_{50}$	20Pb30Ba50P
$(PbO)_{10}(BaO)_{40}(P_2O_5)_{50}$	10Pb40Ba50P
$(BaO)_{50}(P_2O_5)_{50}$	50Ba50P
$(BaO)_{55}(P_2O_5)_{45}$	55Ba45P

1.2 Thesis structure

This dissertation has five chapters, including this introduction.

In the second chapter, general background information is provided. This includes fundamental background information about the definition, formation, and the structure of glass followed by a particular focus on relevant phosphate-based crystals and glass. Moreover, the elastic and photoelastic properties of glass and its correlation to the structure of different glass systems are reviewed in the second part of this chapter.

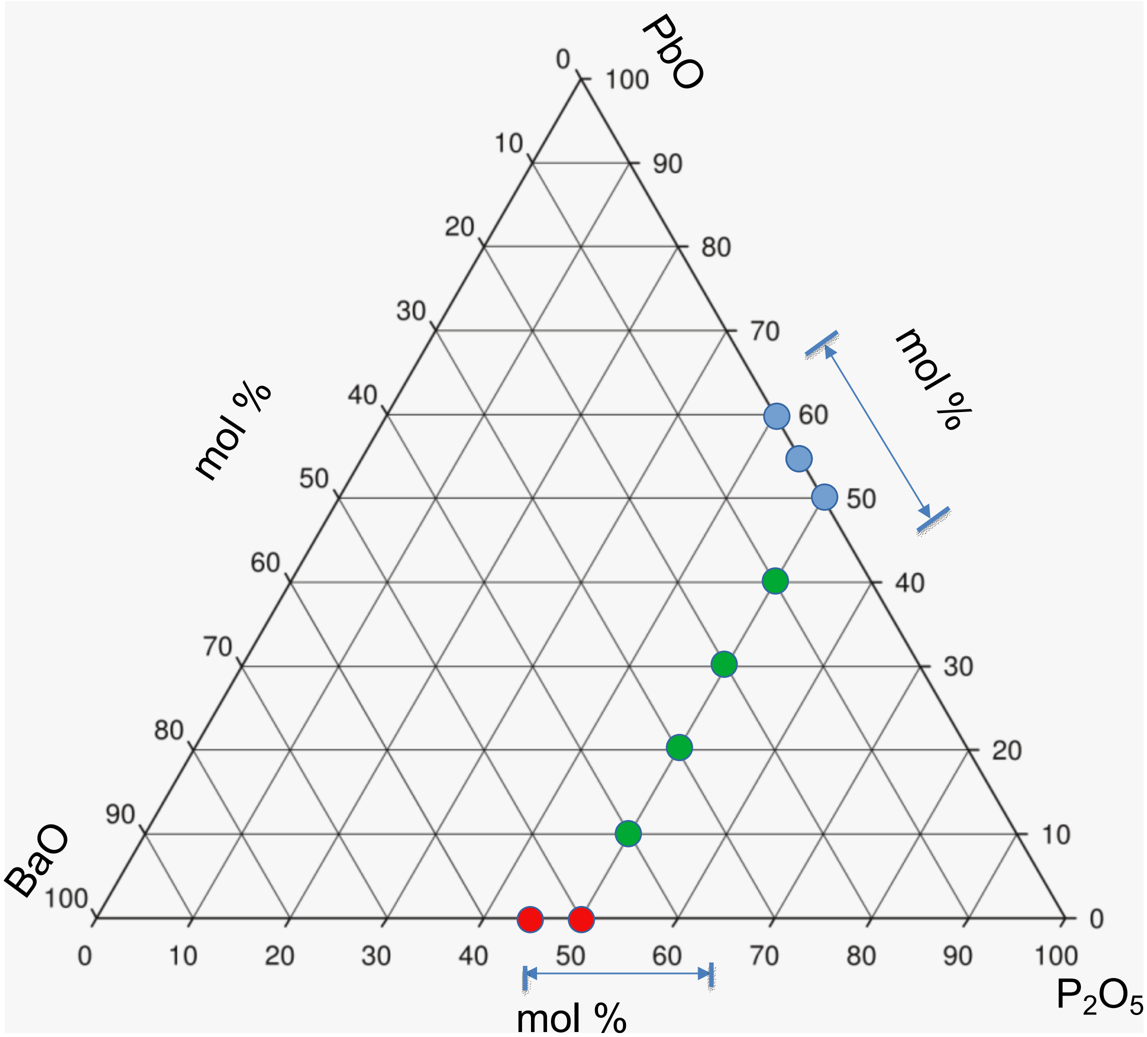

Figure 1.1: Composition diagram of the glass samples studied in this dissertation, as well as the glass forming ranges (represented by blue arrows) of the binary compositions [25, 26]. Red dots: BaO-P_2O_5 binary compositions; blue dots: PbO-P_2O_5 binaries; green dots: BaO-PbO-P_2O_5 ternaries

This chapter broadly represents the origin of the aforementioned goals of this study.

The theory and implementation of each experimental technique that has been used in this study is described in the third chapter. Specific experimental details of glass preparation, elemental analysis, density measurements, the ultrasonic method, advance solid-state nuclear magnetic resonance (ssNMR) spectroscopy and photoelastic properties are provided.

In the fourth chapter, the experimental results for ternary lead barium phosphate glasses as well as binary lead phosphate and barium phosphate glasses are presented and discussed. To begin, glass preparation techniques, x-ray diffraction technique and an elemental analysis of random compositions are presented to verify their amorphous nature and compositions. This is followed by density measurements and the molar volume values derived from them. Thereafter, structural studies of our glass systems performed by ssNMR spectroscopy are provided and interpreted in detail. Finally, the elastic and photoelastic properties of a series of compositions which were determined with the aid of ultrasonic techniques and several optical techniques are presented and interpreted.

In the last chapter, the overall results are discussed with the purpose of finding the correlation between structure and properties of our glass systems.

Chapter 2

Background

Glass is omnipresent in many aspects of our daily lives. It can be used in packaging (bottles), construction (windows), telecommunication (fiber-optic cables) and medical applications (emetic and bioactive glass), to name a few. To foster its applications, it is crucial to have a deep understanding of its structure. The first goal of this dissertation is to find the correlation between the structure and elastic properties of binary and ternary glasses containing a combination of PbO, BaO, and P_2O_5. The second target is to determine the photoelastic properties of our glass samples and confirm the reliability of the empirical model based on our results. This chapter covers the basic principles of glass structure along with its properties, which is essential in understanding the following chapters.

2.1 Definition of Glass

Glass can be defined as an amorphous solid or a solid with a liquid-like structure [27]. For any material to be considered a glass, there are two main conditions that need to be satisfied. Firstly, it has to have long-range disorder of its atomic arrangements [27]. As a consequence of the first condition, it will have isotropic properties in the absence of internal and external stresses. Secondly, it has to exhibit a unique time and composition-dependent glass transformation behavior, which is characterized by the glass transition temperature T_g [27, 28].

To have a clearer picture of the glass transformation behavior, it is important to first understand how to make crystal vs glass. Crystals are typically obtained by cooling of the melt gradually below its melting temperature T_m. However, in the glass making procedure, molten glass remains liquid even below its melting temperature, where it is called “super-cooled”. This behavior continues with a change in volume followed by a drastic rise in viscosity to the point that atoms can no longer rearrange to their equilibrium structure (see Figure 2.1) [28].

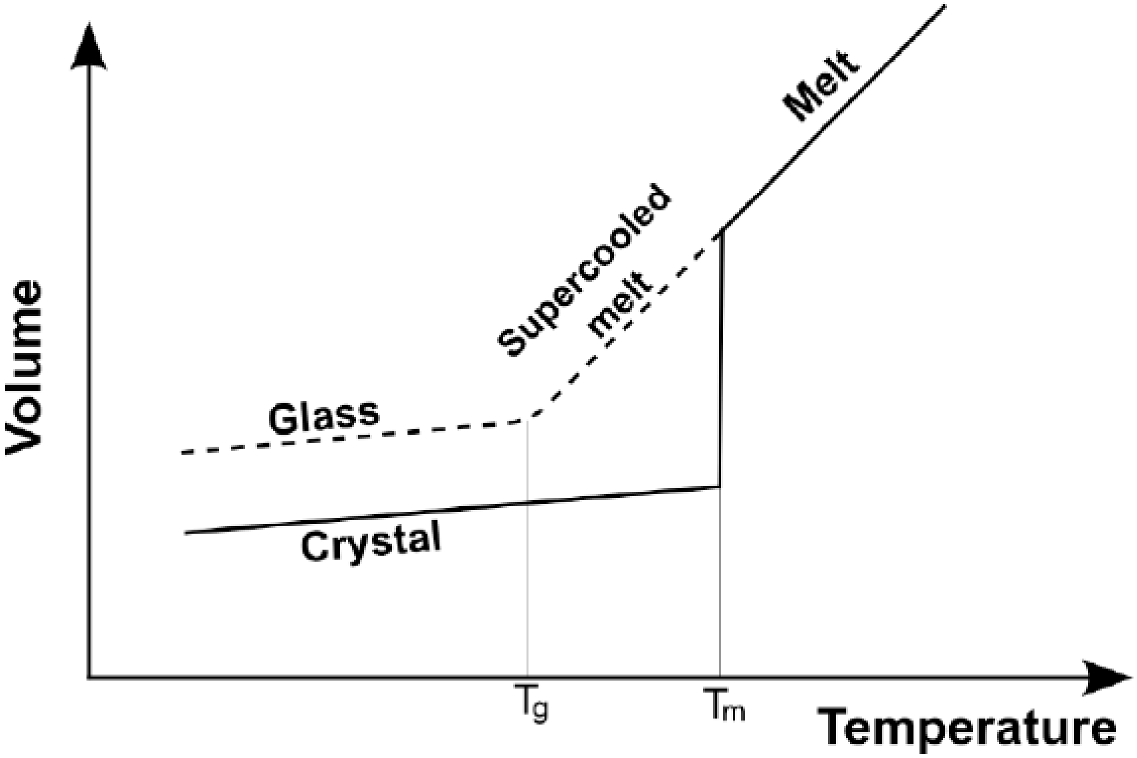

Figure 2.1: The volume-temperature diagram for a glass and a crystal [29].

2.2 Structural Theories of Glass Formation

Several theories have been proposed to explain glass structure, which are based on factors such as atomic coordination number, bonding rules, electronegativity, bond strength and so on [27].

The most popular and well-accepted theory about glass structure at least for oxides, was published by Zachariasen in 1932 [30]. This theory is known as the random network theory [30]. In the random network theory, glass and its corresponding crystal are considered to be formed by the same short range structural units. However, in a crystal, structural units repeat in a unique pattern; while, in glass, they are randomly distributed (see Figure 2.2).

In the random network theory, Zachariasen proposed that the glass compound AnOm (A is a cation, O is an oxygen anion, m and n are integers) can be formed under the following four conditions:

1. An oxygen atom cannot be linked to more than two cations;

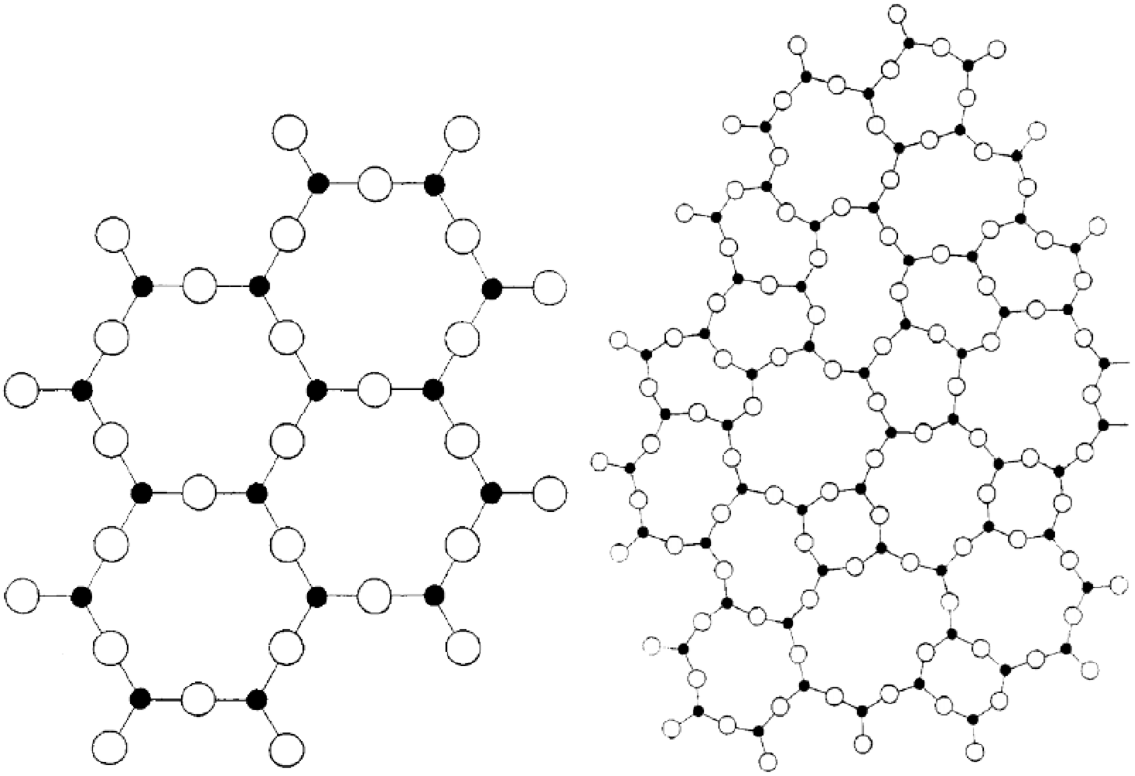

Figure 2.2: A schematic representation of a two-dimensional crystalline structure (left) and a amorphous structure (right) of an oxide A_2O_3 [30].

2. The cation's coordination number must be small (bonded to two or three oxygen atoms);
3. The cation-oxygen polyhedra in 3D structure are only linked via their corners rather than their edges or faces; and
4. At least three corners of each polyhedra are required to be shared.

2.3 Role of Oxides in Glass

According to the aforementioned conditions by Zachariasen, oxides can be categorized into three main groups. The first group belongs to some oxides of AO_2, A_2O_3 and A_2O_5 formula which each alone can form glass. These oxides are known as glass network formers. SiO_2, B_2O_3, and GeO_2 are the most common glass network formers which can form a glass as a pure oxide.

The second category includes oxides of the formula A_2O and AO which cannot form a glass on their own. However, they can participate in a glass network composed of the glass network former. These oxides are known as a glass network modifier. They are mostly incorporated into the glass network by the addition of non-bridging oxygen (NBO) atoms to modify their structure and properties [27]. One of the most common glass network modifiers is Na_2O. In binary SiO_2-Na_2O glass system, Na_2O acts as a glass network modifier by breaking the long silicon-oxygen chains and transforming one bridging oxygen (BO) into two NBOs (see Figure 2.3) [29]. This will lead to a significant reduction in glass viscosity as well as the melting temperature.

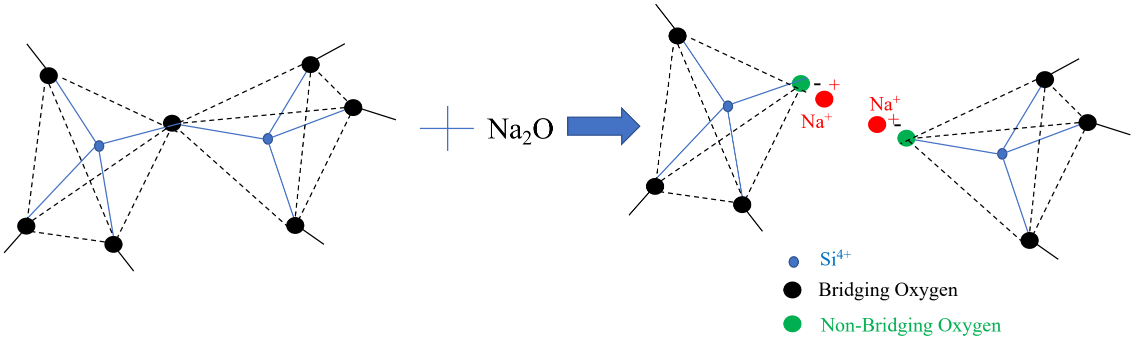

Figure 2.3: A schematic representation of the non-bridging oxygen formation through the introduction of NaO to SiO_2-Na_2O glass system. Reprinted and modified with permission from Dr. Vincent Martin [31].

The final category belongs to oxides which can either act as a glass network former or a glass network modifier based on their concentration or their interaction with other oxides. This group of oxides are known as glass network intermediates. PbO and Al_2O_3 are one of the most common glass network intermediates. In lead borate glass, PbO acts as a glass network modifier through ionic Pb - O bonds with a coordination number of around 6 or 7 at low content. However, at high concentration, it will act as a glass network former through the formation of a covalent Pb-O bonds with the coordination number of 3 or 4 [32, 33].

2.4 Structure of Phosphate glass

The structure of crystalline and non-crystalline phosphates are comprised of PO_4 tetrahedra which are linked through their corners to build a chain-like configuration [3]. This configuration is based on the formation of sp^3 hybrid orbitals by the phosphorus outer electrons ($3s^2 3p^3$), of which the fifth electron can from a strong π-bond with an oxygen 2p electron [34]. Various phosphate anions can be formed by PO_4 tetrahedra through their covalent BO bonds.

The notation Q^n is used to classify the PO_4 tetrahedra, where n denotes the number of BOs per tetrahedron (see Figure 2.4). The structure of phosphate glass can be classified based on their compositions in the following order [2]:

- Cross-linked network of Q^3 tetrahedra as found in glass with very high P_2O_5 content.
- Polymer-like metaphosphate chains of Q^2 tetrahedra.
- Glass based on small pyrophosphate (Q^1) and orthophosphate (Q^0) anions.

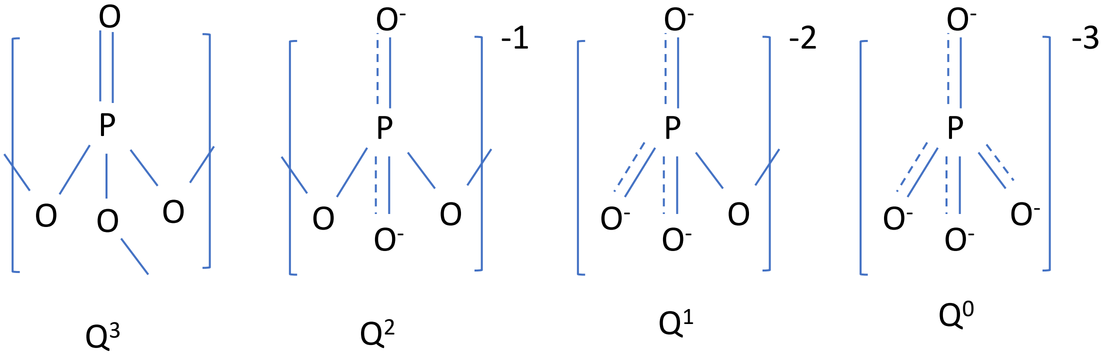

Figure 2.4: Classification of the PO_4 tetrahedral sites which can exist in phosphate glasses. Reprinted and modified from Richard K. Brow [2].

The structure of complex glass systems such as ternary glasses can not be fully resolved without comprehensive knowledge of the binary glass. For this reason, it is necessary to first understand the binary phosphate glass and crystal structures.

2.5 Binary phosphate glasses

Pure P_2O_5 is comprised of the PO_4 tetrahedra which are linked together to build a three-dimensional random network structure. The introduction of modifying oxide(s) to this structure breaks up the PO_4 tetrahedra network by the creation of the NBOs in exchange for the BOs. These NBOs coordinate with the cations through the weaker ionic bonds. In binary phosphate glasses, the depolymerization of the phosphate network with the addition of A_2O (or AO) can be expressed by the following pseudo-reaction described in Van Wazer's model [35]:

For $x \leq 0.50$, $\quad 2\,Q^3 + A_2O \longrightarrow 2\,Q^2 + A_2O$,

For $0.5 < x \leq 0.67$, $\quad 2\,Q^2 + A_2O \longrightarrow 2\,Q^1 + A_2O$.

Van Wazer's model predicts that before the formation of the Q^1 species, all of the Q^3 sites should be converted to the Q^2 sites. In binary $(A_2O)_x(P_2O_5)_{(1-x)}$ glass systems at $x = 0.50$, all of the chains and rings built by the PO_4 tetrahedra should be in the Q^2 sites form. Then, at $x > 0.50$, Q^1 species start to form, along with the termination of Q^2 units. The proportion of different Q^n sites in binary phosphate glass systems was predicted as a function of modifying oxide by Van Wazer's model [35]:
For $0 \leq x < 0.5$,

$$f_{Q^3} = \frac{1-2x}{1-x}, \tag{2.1}$$

$$f_{Q^2} = \frac{x}{1-x}. \tag{2.2}$$

For $0.5 \leq x < 0.67$,

$$f_{Q^2} = \frac{2-3x}{1-x}, \tag{2.3}$$

$$f_{Q^1} = \frac{2x-1}{1-x}. \tag{2.4}$$

For $0.67 \leq x < 0.75$,

$$f_{Q^1} = \frac{3-4x}{1-x}, \tag{2.5}$$

$$f_{Q^o} = \frac{3x-2}{1-x}. \tag{2.6}$$

One of the most common experimental techniques to determine the Q^n distribution is the ^{31}P magic angle spinning (MAS) ssNMR. Based on the previous studies on ultraphosphate (x < 0.5) and alkali polyphosphate (x > 0.5), Van Wazer's model prediction of the Q^n distribution was experimentally confirmed [2, 36–38].

2.6 Crystalline Phases

In order to have a starting point understanding of the glass atomic structure and properties, crystals of similar composition were surveyed from previous studies and compared to each other. Several crystalline compounds are present in the BaO.P_2O_5 phase diagram of which two (BaP_2O_6 and BaP_2O_7) were selected to be compared to their corresponding glasses [26].

The first crystal of interest is barium metaphosphate, BaP_2O_6, which has monoclinic space group, $P2_1$/n (Z = 4), with unit cell dimensions of a = 9.695, b = 6.906, c = 7.522 $\mathring{A}$; $\beta = 94.75$ °; $V_{cell} = 501.9\mathring{A}^3$ [39]. The crystal structure of BaP_2O_6 is displayed in Figure 2.5. It has a single crystallographic Ba^{2+} site, two P^{5+} sites and six O^{2-} sites. In the BaP_2O_6 crystal structure, the incorporation of barium ions break up the PO_4 tetrahedra network by the creation of NBOs which can coordinate with the cations through the weaker ionic bonds. The phosphate network mostly consists of polymer-like metaphosphate chains of Q^2 species with a small fraction of Q^3 units. Barium ions represent an ionic environment which are coordinated to 8 oxygen atoms as [BaO_8] between phosphate chains.

The next crystal of interest from the BaO.P_2O_5 system is barium pyrophosphte, $Ba_2P_2O_7$, which is formed in higher BaO content (more than 50 mol%). $Ba_2P_2O_7$ has orthorhombic crystal structure, *Pnma* (Z = 4), with cell dimensions of a = 9.2875, b = 5.6139 , c = 13.8064 $\mathring{A}$; $V_{cell} = 719.85\mathring{A}^3$ [40]. This crystal structure is comprised of two distinct crystallographic Ba^{2+} sites, two P^{5+} sites and five O^{2-} sites (See Figure 2.6). The addition of BaO in the BaO.P_2O_5 system above 50 mol% results in the creation of more NBOs with an increase in the Ba-O coordination number from [BaO_8] to [BaO_9]. Therefore, the average length of the phosphate chains becomes shorter and shorter until the structure is comprised of diphosphate anions ([P_2O_7]) (See Figure 2.6). In this crystal, the phosphate network consists of two Q^1 units linked by a common bridging oxygen.

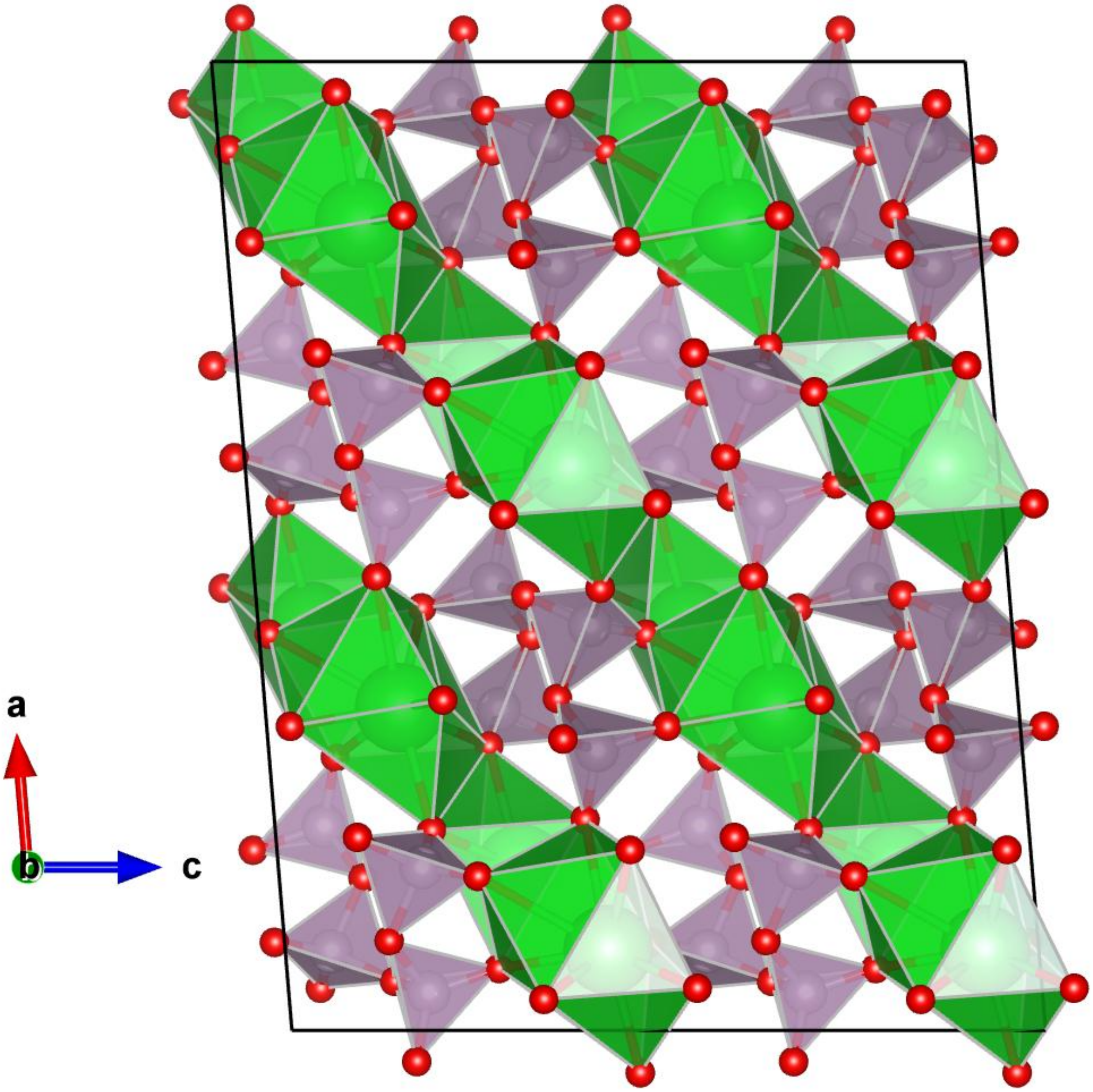

Figure 2.5: The room-temperature crystal structure of BaP_2O_6 [39]. The presented view is down the crystallographic b axis with a 2 x 2 x 2 super cell. $[BaO_8]$ polyhedra are colored green while $[PO_4]$ tetrahedra are colored purple.

Among all the crystalline compounds presented in the $PbO.P_2O_5$ phase diagram, two of them (PbP_2O_6 and PbP_2O_7) correspond to our glass compositions [25].

PbP_2O_6 has monoclinic space group, $P2_1/c$ (Z = 8), with unit cell dimensions of a = 7.29, b = 7.95 , c = 17.28 $\mathring{A}$; $\beta = 90.5°$; $V_{cell} = 1001.43 \mathring{A}^3$ [41]. Figure 2.7 displays the crystal structure of PbP_2O_6 which has two distinct crystallographic Pb^{2+} sites, four P^{5+} sites and twelve O^{2-} sites.

In PbP_2O_6 structure, Pb^{2+} ions break up the PO_4 tetrahedra network by the creation of NBOs which coordinate with the cations through the weaker ionic bonds.

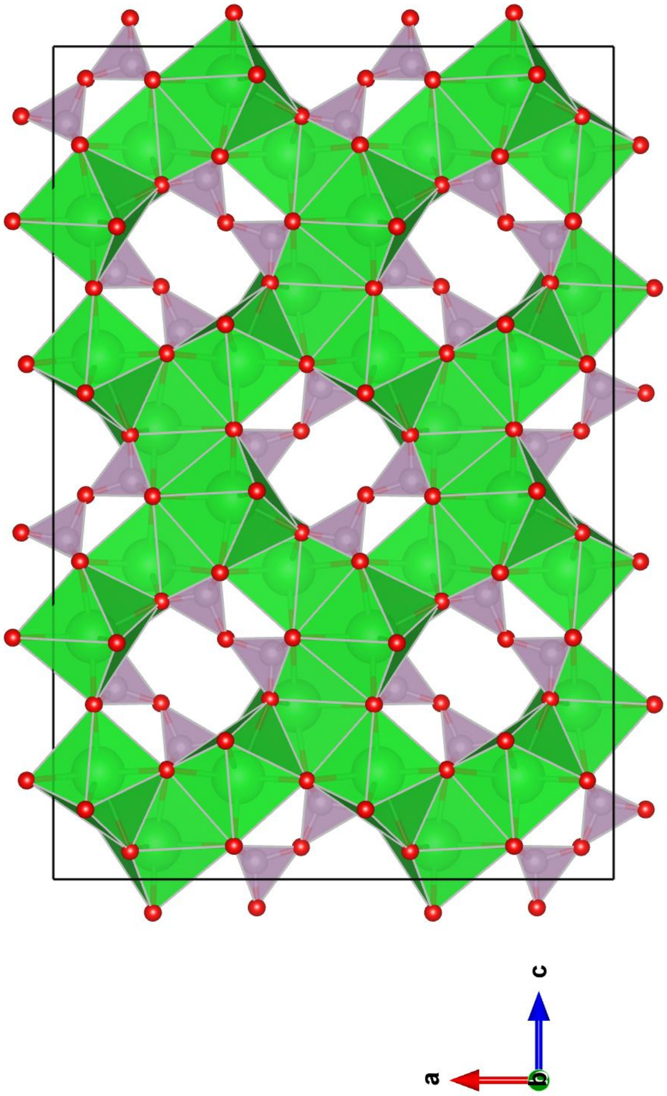

Figure 2.6: The room-temperature crystal structure of $Ba_2P_2O_7$ [40]. The presented view is down the crystallographic b axis with a 2 x 2 x 2 super cell. $[BaO_9]$ polyhedra are colored green while $[PO_4]$ tetrahedra are colored purple.

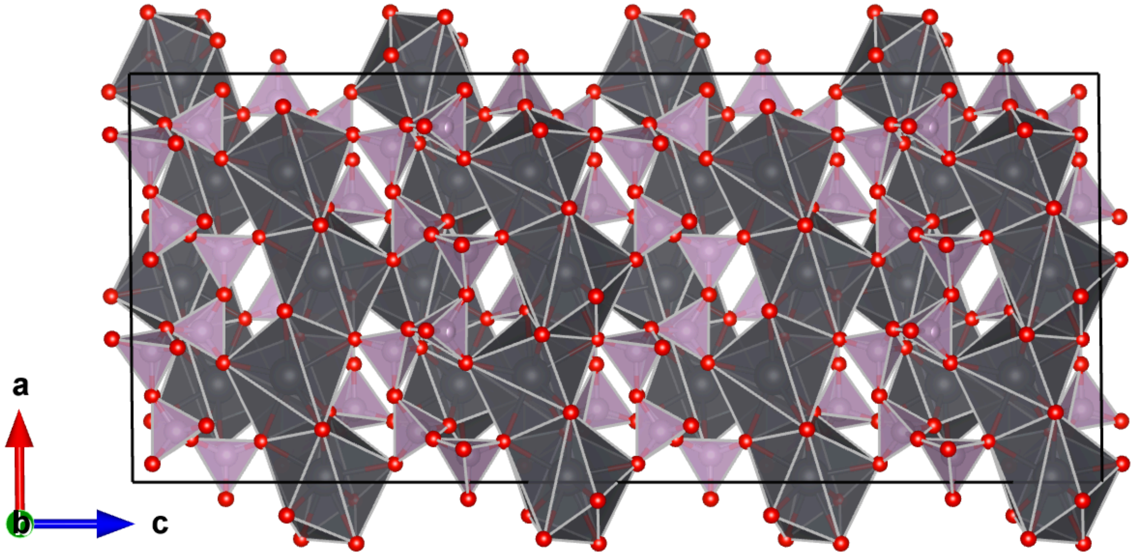

Figure 2.7: The room-temperature crystal structure of PbP_2O_6 [41]. The presented view is down the crystallographic b axis with a 2 x 2 x 2 super cell. [PbO_6] and [PbO_7] polyhedra are colored grey while [PO_4] tetrahedra are colored purple.

PbP_2O_6 consists of long chains and rings of PO_4 tetrahedra with an ionic environment of lead atoms which are coordinated to 6 or 7 oxygen atoms as [PbO_6] or [PbO_7] between phosphate chains. In this structure, the network mostly consists of polymer-like metaphosphate chains of Q^2 species with a small fraction of Q^3 units.

Another crystal from the $PbO.P_2O_5$ system is lead pyrophosphate, $Pb_2P_2O_7$, which has a high PbO content (more than 50 mol%). $Pb_2P_2O_7$ has triclininc space group , $P\overline{1}$ (Z = 4), with unit cell dimensions of a = 6.914, b = 6.966 , c = 12.751 $\mathring{A}$; α = 96.82, β = 91.14, γ = 89.64°; V_{cell} = 609.65$\mathring{A}^3$ [42]. This crystal structure is comprised of four distinct crystallographic Pb^{2+} sites, four P^{5+} sites and fourteen O^{2-} sites (See Figure 2.8). The addition of PbO in the $PbO.P_2O_5$ system above 50 mol% results in the creation of more NBOs with an increase in the lead coordination number from [PbO_6] and [PbO_7] to [PbO_8] and [PbO_9]. Therefore, the average length of the phosphate chains becomes shorter and shorter until the structure is comprised of diphosphate anions ([P_2O_7]) which is made up of two tetrahedral PO_4 groups sharing an oxygen atom (See Figure 2.8). The structure network is comprised of two Q^1 units linked by a common bridging oxygen.

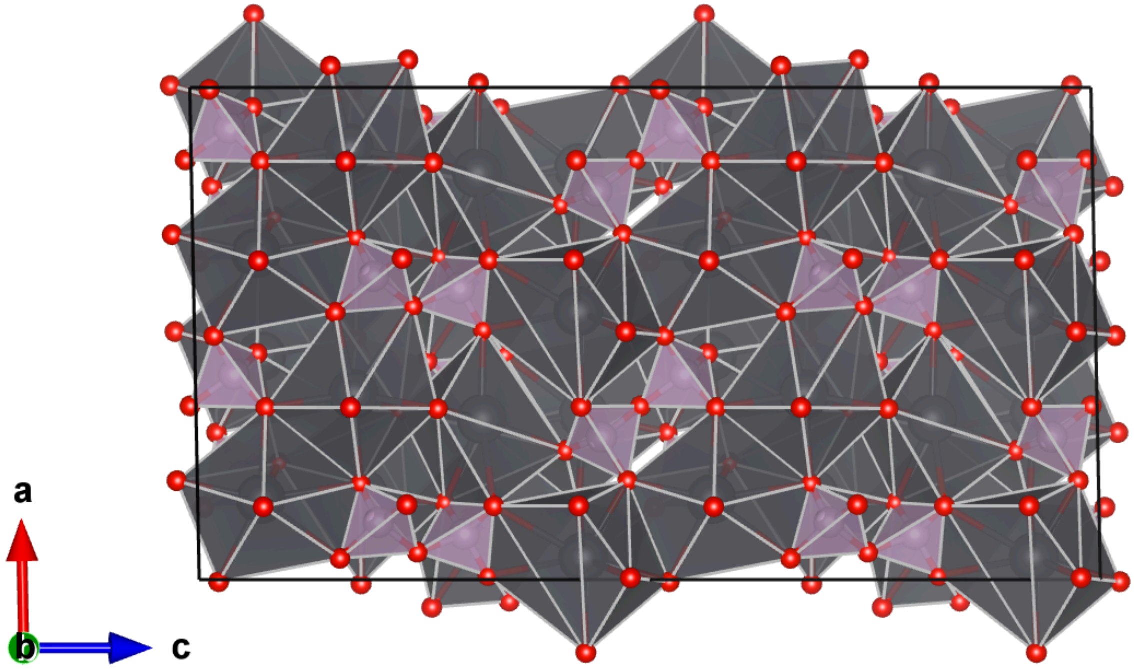

Figure 2.8: The room-temperature crystal structure of $Pb_2P_2O_7$ [42]. The presented view is down the crystallographic b axis with a 2 x 2 x 2 super cell. [PbO_8] and [PbO_9] polyhedra are colored grey while [PO_4] tetrahedra are colored purple.

The $BaPbP_2O_7$ crystal structure has been found to have similar structural features to our ternary lead barium phosphate glass compositions. $BaPbP_2O_7$ has an orthorhombic unit cell, *Pnmb* (Z = 4), with unit cell dimensions of a = 5.594, b = 9.108 , c = 13.426 $\AA$; $V_{cell} = 684.06 \AA^3$ [43]. This crystal structure is comprised of one distinct crystallographic Pb^{2+} site, one Ba^{2+} site, two P^{5+} sites and five O^{2-} sites (See Figure 2.9).

In $BaPbP_2O_7$ crystal structure, Pb^{2+} and Ba^{2+} cations terminate the PO_4 tetrahedra network by the creation of NBOs to the point until the length of the phosphate chains and rings becomes shorter and shorter until the structure is comprised of diphosphate anions ([P_2O_7]) surrounded by [PbO_6] and [BaO_8] polyhedra. This phosphate network is comprised of two Q^1 units linked by a common bridging oxygen.

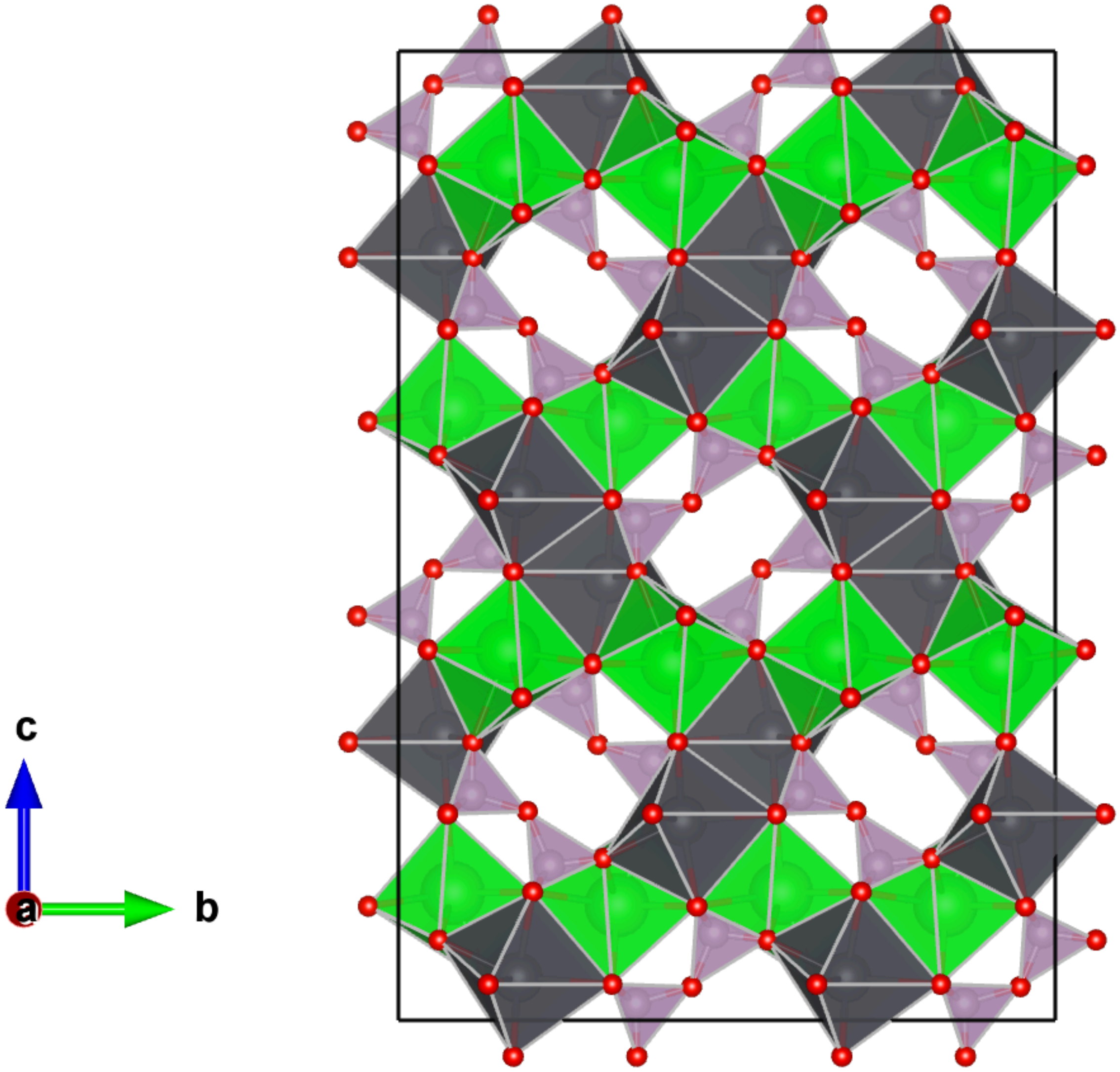

Figure 2.9: The room-temperature crystal structure of $BaPbP_2O_7$ [43]. The presented view is down the crystallographic a axis with a 2 x 2 x 2 super cell. [PbO_6] polyhedra are colored grey, [BaO_8] polyhedra are colored green and [PO_4] tetrahedra are colored purple.

2.7 Elastic Properties of Glass

Glass materials play a prominent role in numerous technological and industrial applications. However, their brittleness to high thermal or mechanical stress has always limited their roles. Therefore, novel approaches toward producing stronger and more damage resistant glass, as well as new methods of measuring their elastic properties have been highlighted extensively in recent years [44]. Here we overview the structural features believed to be important in glass elasticity.

2.7.1 Glass Topology

There are various parameters responsible for mechanical behavior in any material. Among them, the microstructure of single and polycrystalline materials (grain boundaries) along with their structural defects (e.g., stacking faults) are found to be most responsible. However, it should also be noted that glass does not possess a long-range order in an atomic organization or microstructure to control its mechanical properties. Therefore, the topology of the disordered glass network such as the degree of polymerization, channel formation, structural dimensionality, and packing density are found to be responsible for its mechanical properties [45].

The degree of polymerization can be defined by the number of glass former bonds forming the glass network system, such as Si-O-Si bonds in pure silica. The addition of network modifier(s) creates NBOs which leads to a termination of the network connectivity. Furthermore, the introduction of modifier(s) can change its structural dimensionality from a three-dimensional network to a two-dimensional chain-like structure. It was also shown that a sufficient amount of modifier content can create ion channels which can ease the way of ionic diffusion throughout its structure [46].

Atomic packing density (V_f) is defined as the theoretical volume occupied by atoms vs. free volume. V_f can be calculated by assigning volume to each ion ($\frac{4}{3}\pi R_i^3$) and comparing the total to the molar volume [47]:

$$V_f = \frac{1}{V_m} \sum_i N_A x_i \frac{4}{3} \pi R_i^3, \tag{2.7}$$

where V_m is the molar volume, N_A is Avogadro's number and R_i is the Shannon-Prewitt ionic radius corresponding to the expected coordination number in oxide crystals [48]. It should be noted that the ionic radii in glass is assumed to be identical with its corresponding crystal [47]. It was also found that V_f and network dimensionality are inversely correlated for various types glass systems [45].

2.7.2 Elastic modulii

Young's modulus E, is one of the elastic properties which predicts the stiffness of solids by determining the relationship between stress σ, and strain ϵ, in the linear elasticity regime under uniaxial compression or tension [49]. Within the linear elasticity regime, the relationship between stress and strain is described by Hooke's law. Therefore, stress is proportional to strain and the deformation is reversible [49]. Young's modulus can be calculated by use of the following equation based on the linear portion of the stress-strain curve:

$$E = \frac{\sigma}{\epsilon} = \frac{\frac{F}{A}}{\frac{\Delta L}{L_o}}, \tag{2.8}$$

where F is the exerted force on a solid, A is the area of the cross-section perpendicular to the applied force, ΔL is the amount of change in the length of a solid and lastly L_o represents the initial length of a solid. Glass materials are considered elastic and obey Hooke's law well below their glass transition temperatures.

Poisson ratio ν, is another elastic property which is defined as the negative ratio of transverse contraction strain, to axial stretched strain, in the direction of applied force [45]. Poisson ratio is dimensionless, and represents the resistance of a solid to volume change with respect to its shape change [45] (see Figure 2.10).

Poisson ratio can be calculated by the following equation which is visualized in Figure 2.10.

$$\nu = -\frac{\epsilon_t}{\epsilon_l} = -\frac{\frac{\Delta W}{W}}{\frac{\Delta L}{L}}, \tag{2.9}$$

where ϵ_t is the transverse contraction strain, ϵ_l is the longitudinal extension strain, L is the length and W is the width of an object. Poisson ratio and Young's modulus of inorganic glass are found to be extending from 0.1 to 0.4 and from 5 to 180 GPa, respectively [45].

Bulk modulus K, is the third elastic property. K is described as the resistance of the object to uniform compression. In another words, K can be defined as the relative reduction in the volume of an object while the infinitesimal pressure applied

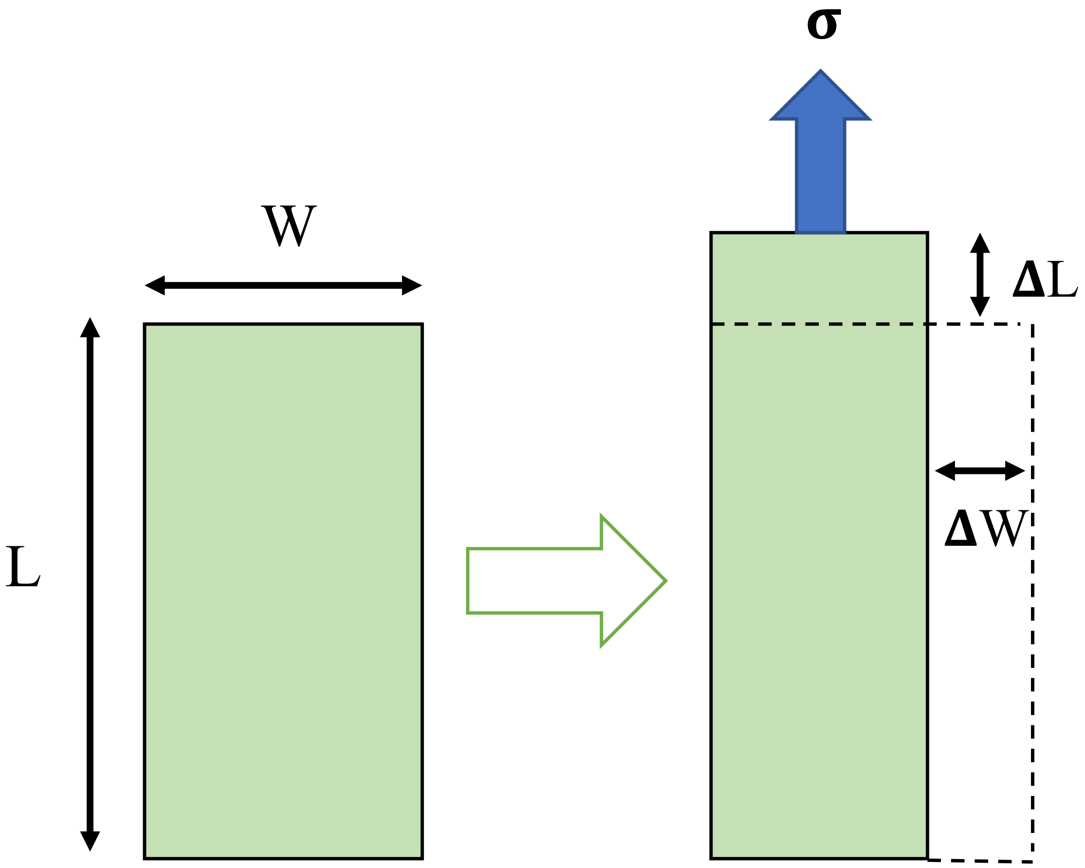

Figure 2.10: A schematic diagram representing the physical meaning of Poisson ratio.

on that object increases. The bulk modulus can be defined by the following equation:

$$K = -V\left(\frac{\partial P}{\partial V}\right)_T, \tag{2.10}$$

where V is the volume, P is pressure and T is the temperature.

Shear modulus, G, is the last elastic property which is defined as the response of an object to shear stress [49]. It is also defined as the ratio of shear stress to the shear strain [49]. With the knowledge of two elastic moduli, the remaining two can be calculated.

2.7.3 Glass Topology and Elastic Properties

Elastic properties of glass are found to be correlated with its atomic organization [45]. Glass atomic organization including its inter-atomic bonding energy, coordination number, polymerization degree and atomic packing density are all found to be accountable for its elastic behaviors [45]. It is therefore essential to investigate the atomic organization of glass, not only to interpret the elastic properties of the known glass, but also to predict the ones that have not been produced yet or are unsafe to synthesize. The atomic-scale or short- to medium range order studies of glass can be conducted with the aid of ssNMR, X-ray or neutron scattering, Raman spectroscopy and in some cases, atomic force microscopy.

The physio-chemical nature of the inter-atomic bonds is one of the parameters which was mentioned earlier to be responsible for the glass mechanical behavior. Unfortunately, the inter-atomic bond distance, along with the coordination number and the directionality of each atom in glass structure is usually unknown. Therefore, elastic properties of glass are mostly interpreted based on the estimated inter-atomic bonding energies and cationic field strength [50]. Another major parameter which needs to be taken into account for the interpretation of the elasticity data is the atomic packing density or molar volume (V_m).

Young's modulus has been found to be intimately related to both the average inter-atomic bond energy and the volume density of bonds [44]. In mechanical design, the specific stiffness of glass can be obtained via either bond strength or by filling the free volume (inter-molecular space) through the addition of different sized modifier(s) [44]. The type and strength of the bonds in a glass network structure can significantly influence its elastic properties. For instance, the addition of modifiers in silicate and phosphate glasses creates NBOs through the termination of Si-O-Si and P-O-P bonds, which results in an increase in E and K [44].

On a molecular scale, Poisson ratio ν, the atomic packing density and glass network dimensionality have all been found to be strongly correlated [45]. Atomic packing density increases monotonically with Poisson ratio which is also verified within certain chemical compositions. Therefore, atomic packing density values can be estimated based on the ν. It is also worth mentioning that due to the lack of accuracy in actual atomic radii, the exact value of atomic packing density cannot be calculated.

Makishima and Mackenzie proposed a linear trend between ν and V_f for glasses of similar systems ($\nu = 0.5$ - $\frac{1}{7.2V_f}$) [51]. However, in a global review by Tanguy Rouxel, a sigmoidal-like trend between ν and V_f was proposed, which is more complex.

The Poisson ratio has also been found to be correlated to the glass network dimensionality or the number of BO in each glass-forming cation n_{BO} (or the average coordination number). Based on the experimental data reviewed by Tanguy Rouxel, ν decreases monotonically while n_{BO} is decreasing [45]. For instance, amorphous silica exhibits a small Poisson ratio ($\nu = 0.15$) due to its highly cross-linked structure with four BO per glass-forming atom (3D network). On the contrary, chain-based chalcogenide glass have a higher Poisson ratio ($\nu = 0.3$). Additionally, B_2O_3 and P_2O_5 glasses with $n_{BO} = 3$ (P is coordinated to five oxygen with P = O double bond and three BO atoms) have a Poisson ratio around 0.3 [52]. This trend was also observed within given chemical systems which is more noticeable when modifiers with very different valencies or coordination numbers replace one for the other.

2.8 Photoelasticity

Glass is isotropic in a homogeneous and stress-free state, thus properties are the same in all directions. Consequently, optical properties of glass including its index of refraction are the same in all directions [27]. However, the isotropy of glass can be broken under the application of mechanical stress, which leads to a different index of refraction in the extraordinary and ordinary directions. The difference between extraordinary and ordinary refractive indices is the phenomenon known as birefringence. The stress induced birefringence is called photoelasticity or the pizezo-optic effect. Photoelasticity is also an experimental technique which describes the stress and strain distribution of a material.

The stress distribution can be observed through a polariscope in the form of fringe patterns [53]. There are various types of polariscopes which are designed for different purposes; however, linear polarizers and quarter-wave plates are the main components of all of them. The Senarmont method of compensation is considered to be the simplest technique to measure the stress optic coefficient (C) of a glass [54]. The complete description of this method is provided in section 3.9.

2.9 The Stress-Optic Coefficient

The difference between two refractive indices along the extraordinary axis, n_e, and in the ordinary plane, n_o is given in the following equation:

$$\Delta n = n_e - n_o, \tag{2.11}$$

where Δn is the birefringence. This difference is proportional to applied mechanical stress, σ, by the following equation:

$$\Delta n = C\sigma, \tag{2.12}$$

where C is the constant of proportionality which is known as the Stress optic coefficient and its unit is Brewsters ($1B = 1 \times 10^{-12} Pa^{-1}$).

When there are different refractive indices in three cartesian directions x_1, x_2 and x_3, their relative magnitude and directions can be described by an ellipsoid called the indicatrix. The indicatrix is given by:

$$\frac{x_1^1}{n_1^2} + \frac{x_2^1}{n_2^2} + \frac{x_3^1}{n_3^2} = 1, \tag{2.13}$$

where n_1, n_2 and n_3 are refractive indices in three cartesian directions. B_i is the relative dielectric impermeability which can be defined as $B_i = \frac{1}{n_i^2}$. Hence, equation 2.13 can be rewritten as:

$$B_1 x_1^2 + B_2 x_2^2 + B_3 x_3^2 = 1. \tag{2.14}$$

The stress-induced birefringence can also be described by the elasto-optic tensor elements p_{ijkl} and piezo-optic tensor elements π_{ijrs}. These fourth-ranked tensors relate the applied stress or strain to the change in the inverse of dielectric constant which is given in the following equations:

$$\Delta B_{ij} = \pi_{ijrd}\sigma_{rs} = p_{ijkl}s_{kl}, \tag{2.15}$$

$$B_{ij} = (\frac{1}{n^2})_{ij} = (\frac{1}{\epsilon})_{ij}, \tag{2.16}$$

where B_{ij} is the inverse dielectric tensor, σ_{rs} and s_{kl} are the stress and strain tensor, respectively [27, 55]. The stress and strain tensor elements are related to each other by the following equation:

$$p_{ijkl} = \pi_{ijrs}C_{rskl}, \tag{2.17}$$

where C_{rskl} is the elastic tensor.

Due to fact that glass has isotropic properties, only three elements of elasto-optic and piezo-optic tensor elements are non-zero, of which two are independent. They can be related to each other by the following relationships:

$$2p_{44} = p_{11} - p_{12}, \tag{2.18}$$

$$2\pi_{44} = \pi_{11} - \pi_{12}. \tag{2.19}$$

The change in the refractive index (n) is small for small stresses. Therefore, the equation 2.15 can be simplified for a uniaxial stress as follows:

$$\Delta B_e = \frac{1}{n_e^2} - \frac{1}{n^2} = \frac{n^2 - n_e^2}{n_e^2 n^2} = \frac{(n - n_e)(2n)}{n^4} = \pi_{11}\sigma_3, \tag{2.20}$$

so that,

$$(n - n_e) = \frac{n^3}{2}\pi_{11}\sigma_3. \tag{2.21}$$

In the same way:

$$\Delta B_o = \frac{1}{n_o^2} - \frac{1}{n^2} = \frac{n^2 - n_o^2}{n_o^2 n^2} = \frac{(n - n_o)(2n)}{n^4} = \pi_{12}\sigma_3, \tag{2.22}$$

so that,

$$(n - n_o) = \frac{n^3}{2}\pi_{12}\sigma_3. \tag{2.23}$$

Consequently, the stress-optic coefficient, birefringence and piezo-optical elements can all be related to each other and expressed by following equations:

$$\Delta n = n_e - n_o = -\frac{n^3}{2}(\pi_{11} - \pi_{12})\sigma_3 = C\sigma_3, \tag{2.24}$$

$$C = -n^3\pi_{44}, \tag{2.25}$$

Or,

$$C = -\frac{n^3}{2G}p_{44}, \tag{2.26}$$

where G is the shear elastic modulus ($G = C_{44}$).

The stress-optic coefficient can have positive, negative or zero values based on the glass composition. Most common glass network formers such as silicates, borates and phosphates express positive C. Heavy modifier oxides can induce negative birefringence which gives rise to a reduction in C values. These modifiers include lead, bismuth, thallium, tin and antimony oxides.

2.10 Theories of Photoelasticity

2.10.1 Mueller's Theory of Photoelasticity

Mueller's theory was proposed by Mueller in 1938. It indicates that the photoelastic response of glass under the application of stress originates from two factors [56]. The first factor is the displacement of atoms in the lattice structure, which is known as the lattice effect. The second factor is the polarization of the electronic cloud corresponding to each atom in the structure, which is known as the atomic effect. According to Mueller's theory, the stress-optic coefficient decreases with the lattice effect while it increases with the atomic effect.

Mueller also states that if a tensile stress applies to a cation-oxygen chain (a cation is bonded to a BO and NBO), the chain will extend toward the direction of the stress. This elongation is a result of the high polarizability of the oxygen atoms. In this case, the BO experiences a much higher deformation in comparison to the NBO [57]. Therefore, the NBO reduces the stress-optic coefficient whereas the BO increases it, according to Mueller's theory. It can also be concluded that in order to minimize the stress-optic coefficient or produce a zero-stress optic glass, the glass structure must contain the maximum number of NBOs.

2.11 Zwanziger's Empirical Model

The focal point of this model is to describe the stress-optic response of glass based on the chemical bonding environment (anion-cation bond length), d, and the coordination number, N_c, of its constituents [58]. Glass with a high d/N_c ratio was shown to have a negative stress-optic coefficient, whereas glass with a low d/N_c ratio was shown to have a positive stress-optic coefficient. The d/N_c ratio has been calculated for various compounds with known stress-optic coefficient signs, some of which are listed in Table 2.1, compiled by Guignard *et al.* [58].

For glasses with $(d/N_c) > 0.5\ \mathring{A}$, C is typically negative, whereas glasses with $(d/N_c) \leq 0.5\ \mathring{A}$ have positive C. Therefore, the composition of positive, negative and zero stress-optic glasses can be obtained by using the following formula:

$$\sum_i x_i(\frac{d}{N_c})_i \approx 0.5\ \mathring{A}, \tag{2.27}$$

Table 2.1: The d/N_c ratio and the sign of C for compounds compiled by Guingard *et al.* [58].

Compound	d/N_c ($\AA$)	Sign of C
Tl_2O	0.84	-
PbO	0.58	-
Bi_2O_3	0.55	-
BaO	0.46	+
SiO_2	0.40	+
P_2O_5	0.38	+

where d is the cation-oxygen bond length, N_c is the cation coordination number of the ith compound and x_i is the molar fraction of the ith oxide in glass. Zero stress-optic glass ($C = 0$ Brewster) can be obtained when the overall sum of the components is approximately equal to 0.5 $\AA$ [58].

The empirical model thus far is consistent with known glass families and it is able to predict the sign of C and zero-stress optic compositions [23, 24, 32, 58, 59]. However, it is not able to estimate the magnitude of C. Furthermore, the value of d and N_c were estimated in some cases, but have yet to be confirmed by structural studies such as ssNMR.

Chapter 3

Experimental Techniques

3.1 Introduction

This chapter briefly describes the basics and background information of the experimental techniques implemented in this study in the following order: glass preparation, x-ray diffraction, elemental analysis, density measurements, elastic properties, solid-state nuclear magnetic resonance (ssNMR), refractive index and stress optic measurement.

3.2 Glass preparation

All of the glasses in this study were synthesized via a traditional melt-quenching technique through the following steps:

1. Mixing and grinding the stoichiometric amounts of reagents in a porcelain mortar and pestle.
2. Calcining the mixture in the oven below the reagents' melting temperature to remove gaseous by-products.
3. Melting the calcined powder in a platinum crucible inside the furnace.
4. Rapidly pouring the molten glass into a mold (also called quenching).
5. Annealing the quenched glass inside an oven at a temperature below the glass transition temperature to eliminate internal stress.

The first series of binary and ternary glass in this study was produced by the following reagents:

- Ammonium phosphate monobasic ($NH_4H_2PO_4$, $\geq 98\%$, Sigma-Aldrich) as the source of the P_2O_5.

- Barium carbonate ($BaCO_3$, ACS reagent, $\geq$ 99%, Sigma-Aldrich) as the source of BaO.

- Lead(ll) oxide (PbO, powder, $<$ 10 μm, ReagentPlus, $\geq$ 99.9%, Sigma-Aldrich) as the source of PbO.

The stoichiometric amounts of the aforementioned reagents were mixed in the porcelain mortar and pestle and then transferred to the platinum crucible. After that, powder samples were first calcined at 550^{o}C followed by another calcination at 850^{o}C based on their compositions for 22 and 24 hours, respectively. The by-product gases including NH_3, H_2O and CO_2 were removed during the calcination procedure through the following reactions:

$NH_4H_2PO_4(s) \longrightarrow HPO_3(s) + NH_3(g)\uparrow + H_2O(g)\uparrow$

$BaCO_3(s) \longrightarrow BaO(s) + CO_2(g)\uparrow$

After the calcination procedure, binary lead and barium phosphate glasses were melted at 1000^{o}C for 1 hour and 1200^{o}C for 2 hours, respectively. The ternary lead barium phosphates were melted at 1050-1200^{o}C for 2 hrs based on their compositions. The calcination, melting time and temperature were selected based on the previous investigation in our group by Justine Galbraith on the same glass compositions [23, 24]. The molten glasses were quenched into a steel mold on a brass plate which was preheated to around 200^oC to prevent them from fracture due to their high thermal stress. After being cast, glasses were transferred quickly to an oven for the annealing procedure. Binary lead and barium phosphate glasses were annealed at 150^{o}C and 450-550^{o}C, respectively. The ternary glass compositions were all annealed at 400^{o}C and cooled down slowly to room temperature.

The annealing procedure relaxes a glass from the residual thermal stress which might cause a fracture while being cut or polished. Therefore, all of our samples were checked to be fully relaxed from the residual thermal stress with a light table. If glass has residual internal stress, the rainbow fringe lines can be observed between two cross polarizers, due to inhomogeneous index of refraction throughout the sample.

Some of the experimental techniques such as elemental analysis and optical measurements require glass with a flat polished surface. For that reason, all of the samples were cut (removing any bubbles or crystalline top layer) with a low-speed saw

(Buehler IsoMet, using a Lapcraft diamond saw blade) to have a square base of around $10 \times 10mm^2$ with a height of the sample $>$ 1 mm. Finally, two faces of glass were polished with 1200 grit silicon carbide paper followed by diamond paste of decreasing grain sizes (30 micron, 15 micron, 9 micron, 6 micron, 3 micron and 1 micron, MetaDi polishing compounds, Buehler).

After performing the elemental analysis on our first series of glasses, the experimental compositions were not in good agreement with the nominal compositions. The discrepancies were ascribed to the volatile nature of P_2O_5. To elaborate, P_2O_5 mass loss can occur during the calcination procedure of $BaCO_3$, specifically for glasses with high BaO mol% contents. Therefore, the P_2O_5 experimental composition in most of the glasses were around 7% off from the nominal compositions. To overcome these issues, the calcination procedure for $BaCO_3$ was avoided by using pure barium oxide (BaO, 99.99% trace metals basis, Sigma-Aldrich) as a source of BaO. Furthermore, the melting temperature and time were optimized and a Pt crucible with a lid was utilized in producing the second series of glasses with the same compositions.

3.3 X-ray Diffraction

X-ray powder diffraction is a powerful technique used in the identification of crystalline phases. In this work, this technique was used to confirm that an amorphous structure was achieved and the samples were free from crystalline compounds. Bragg's law is mostly used to describe the diffraction of wavelength λ from parallel atomic planes (separated by distance d). Equation 3.1 defines Bragg's law and Figure 3.1 shows a diffraction from parallel atomic planes based on Bragg's condition.

$$n\lambda = 2d\sin\theta, \tag{3.1}$$

where n is a positive integer and θ is a scattering angle. In this method, X-rays are generated from a Cu Kα source and collimated via a divergence slit. After that, the sample is bombarded by the emitted X-rays and the diffracted X-rays from the sample are collected by a detector after being passed through receiving slit. Diffracted X-rays also pass through a monochromator which is typically a single crystal with a known d-distance (only detect specific wavelengths) prior to detection. The intensity of diffracted X-rays and the diffraction angle (2θ) are plotted against each other to give

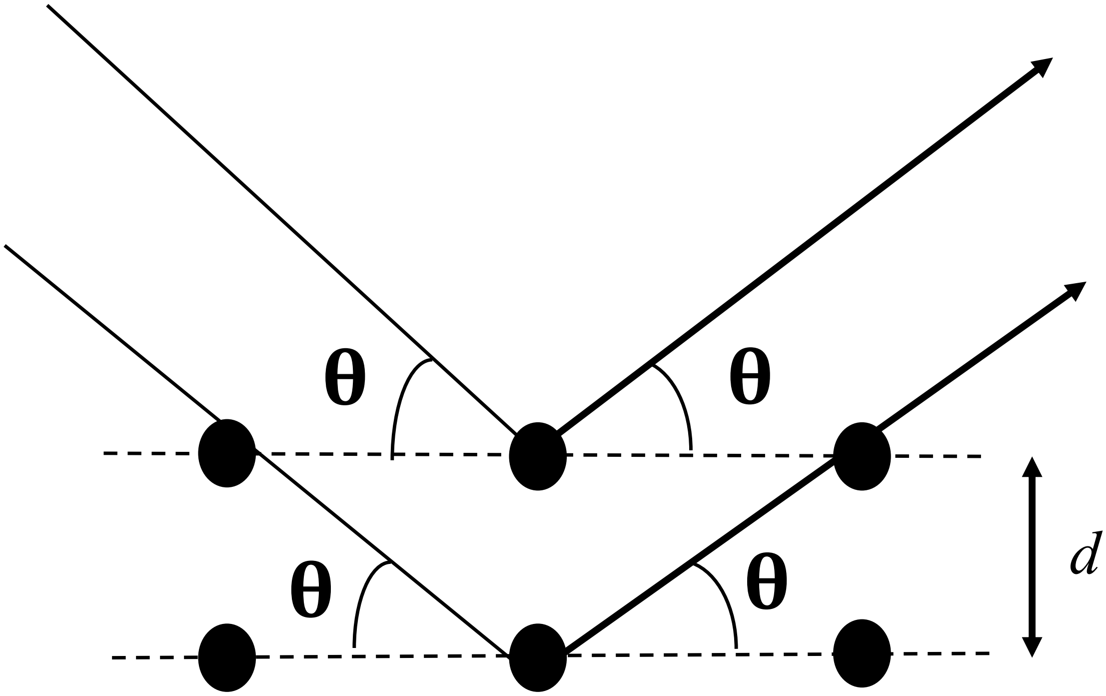

Figure 3.1: Schematic diagram showing the Bragg diffraction from two parallel planes of atoms separated by distance d. If the path length difference between reflected beams is an integer multiple of the wavelength λ (equal to $2d\sin\theta$), the interference is constructive.

a diffraction pattern which is unique for each structure. All diffraction measuremnets in this study were conducted using Siemens D500 equipped with a Cu anode, X-ray tube and monochromator. Angular steps of 0.04 and dwell times of 1s have been used in this work.

3.4 Elemental Analysis

Elemental Analysis (EA) is one of the most crucial techniques when it comes to glass investigations. Since there are a lot of contamination sources which can alter a glass composition as it is melting, accurate EA is always highly recommended before other experiments. A common source of contamination is the type of crucible used for synthesizing glass. For example, silica or alumina can be easily incorporated into a glass composition if they are used as crucibles. Other sources of contamination can be due to the hygroscopic and volatile nature of some oxides (e.g., P_2O_5, B_2O_3) at high temperature which can be reduced by using a lid and low melting temperature if possible. Therefore, EA allows glass scientists to have an accurate sense of compositions, optimize their glass making procedure and derive a trend between structural and physical properties of glasses based on their compositions.

There are various types of EA techniques used in order to acquire quantitative and/or qualitative data of glass composition. Due to specific type of glass composition used in this study, an electron probe micro-analyzer (EPMA) was chosen to characterize the elemental composition of our samples.

3.4.1 Electron probe micro-analyzer

EPMA provides a non-destructive quantitative elemental analysis of solids, including crystalline and non-crystalline minerals. This method implements characteristic X-rays which are released by the sample to diagnose and measure the concentration of elements. EPMA is equipped with different detectors that allow both energy-dispersive and wavelength-dispersive spectroscopy (EDS and WDS).

In this method, free electrons are first produced by heating a tungsten filament to high temperature. Then with the use of a strong voltage (typically 15-20 keV) and a series of magnetic lenses, the low-energy electrons are focused into a high energy and well-collimated electron beam. After that, the sample is bombarded by the primary electron beam. Throughout the bombardment, the sample interacts with the electron beam in various ways to generate: secondary electrons, Auger electrons, back-scattered electrons, low energy light and X-rays [60]. The X-ray is the most important scattering for EPMA. When the primary electron beam reaches the core electrons in the sample, it can displace the core electron and leave a hole behind. This hole is then replaced by an electron from a higher energy level and emits energy in the form of photons (a characteristic X-ray and secondary electron) [61]. Due to the fact that each element has a unique set of X-ray emissions, EPMA is able to distinguish the elements in a given specimen. All the released X-rays from the sample can be separated based on either their energy or wavelength, that is, EDS and WDS, respectively.

In EDS, the detector is a semiconductor block which is able to count the number of electrons entering into its conduction band from an emitted X-ray. Emitted X-rays

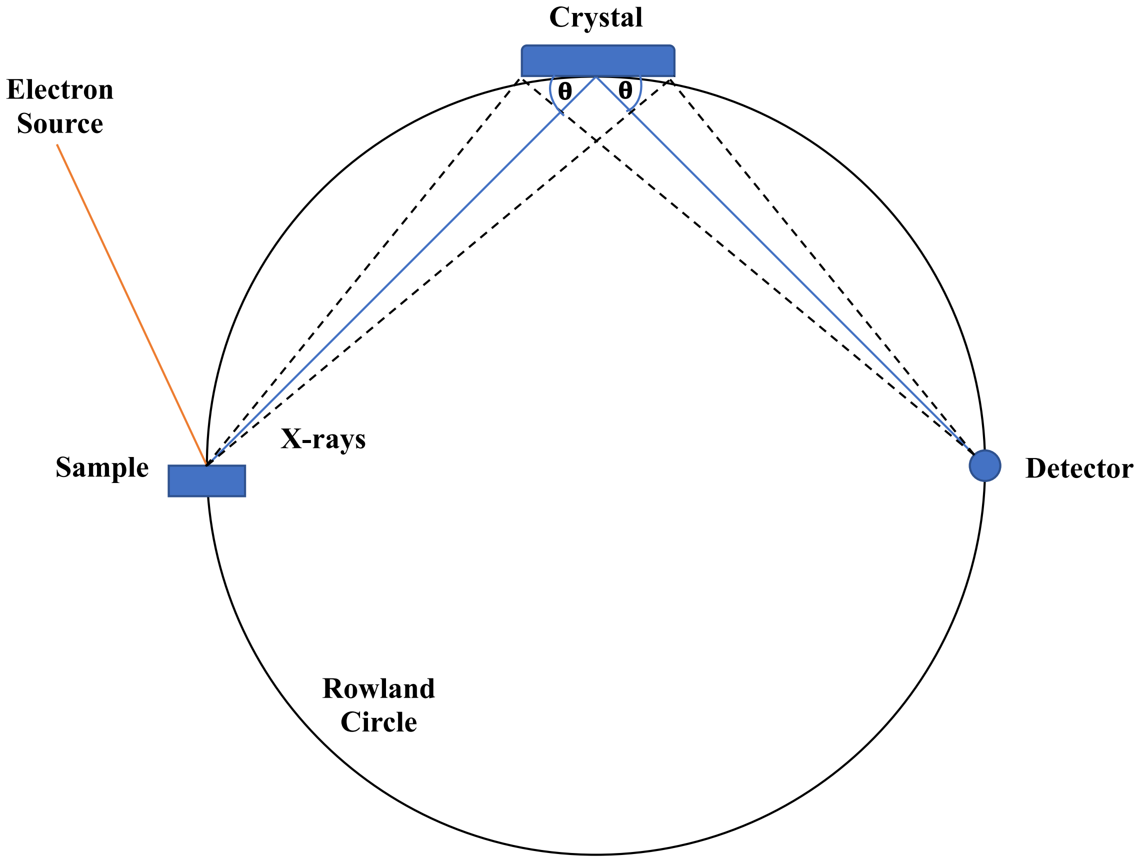

Figure 3.2: Schematic diagram showing a sample, analytical crystal and detector on the circumference of a Rowland circle.

can be determined and separated based on their energy [62]. However, in WDS, specific X-rays are detected and separated based on their wavelengths [63]. Consequently, analytical crystals are implemented to filter X-rays with respect to Bragg's law (See equation(3.1) and Figure 3.1) [64]. In order to pass multiple characteristic X-rays to the detector at the same time, several different analytical crystals simultaneously rotate on Rowland's circle (See Figure 3.2).

WDS wavelength resolution outweighs the energy resolution in EDS, which not only facilitate the elemental selectivity but also reduces the detection limitation. EDS collection times are significantly faster than WDS times since WDS cannot analyze different elements simultaneously [63]. However, EDS data interpretation suffers from a substantial overlap between peaks of similar energies for different elements. Thus, identification of elements and the quantification of their abundance require a sophisticated deconvolution procedure. Furthermore, the EDS detector is equipped with a beryllium window which attenuates X-rays emitted from the lighter elements such as boron [62]. Therefore, due to the fact that oxygen is considered to be a light element for EDS and due to the higher precision and less uncertainty of WDS, we chose WDS to analyze and quantify the elements presented in our samples.

WDS data in this investigation was collected by Dr. Dan MacDonald in the Department of Earth and Environmental Sciences at Dalhousie University; JEOL JXA-8200 Superprobe was utilized with a 15kV running voltage along with the proper standards for ZAF correction. All of the glasses were polished to 1μm and coated with carbon prior to the experiment. The electron beam spot size of 5 μm was used to avoid the electron damage which can lead to unreasonable results. Generally, five to ten data points are required to have a robust confidence of each elemental weight percent. Ten data points were obtained for each samples via quantitative point analysis which has errors of 0.2-1 mol% (calculated from the standard deviation of the mean).

3.5 Density

Density (ρ) is a very important physical property in the investigation of glass. The densities of all samples in this study were measured via Archimedes' principle. This method was performed using a Mettler Toledo density kit, absolute ethanol and an analytical balance. Based on this method, the density of a given sample can be obtained by measuring the mass of the sample in air (m_{air}), the mass of the sample in liquid (m_{liquid}) and the density of the liquid (ρ_{liquid}).

The density of the sample (ρ_{sample}) is then calculated by the following equation:

$$\rho_{sample} = \rho_{liquid}\left(\frac{m_{air}}{m_{air} - m_{liquid}}\right). \tag{3.2}$$

The mass of the sample in the air is recorded by placing the sample on the scoop which is installed on an analytical balance (See Figure 3.3). The mass of the sample in liquid is measured by placing the sample on the bottom scoop which is immersed in the liquid. The liquid used in this study was absolute ethanol due to the hygroscopic nature of phosphate-based glass. Its temperature dependent density was collected from the literature values [65]. The accuracy of the set-up was calibrated by measuring the density of the fused quartz ($\rho = 2.20 g.cm^{-3}$). The density of each glass was measured three times showing an acceptable error $< 1\%$.

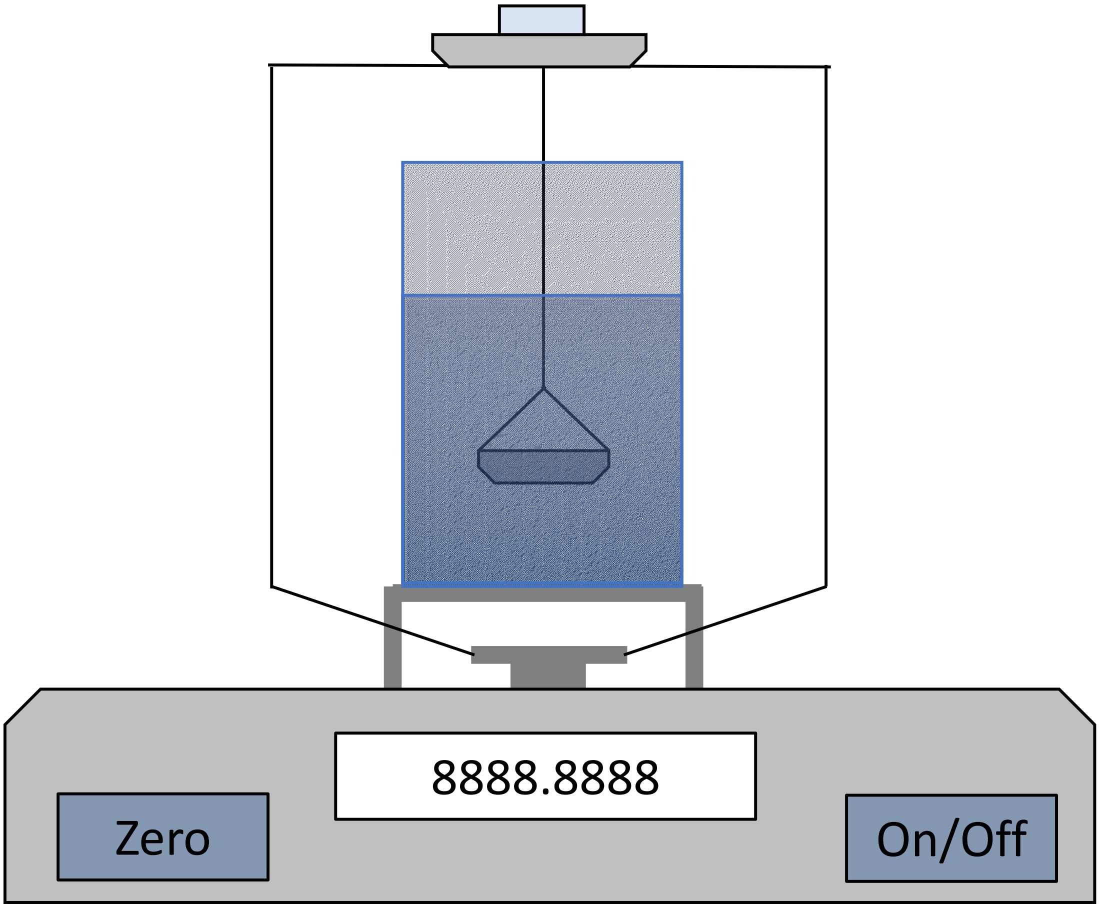

Figure 3.3: Schematic of the density measurement set-up.

An alternative way to present density data is molar volume (V_m). V_m is the volume which one mole of glass occupies. Therefore, V_m of all samples were calculated using the acquired data based on the following equation [27]:

$$V_m = \frac{\sum_i x_i M_i}{\rho}, \tag{3.3}$$

where ρ is the density of the glass calculated by Archimedes principle, x_i is the mole fraction and M_i is the molar mass of the oxide components in the prepared glass samples.

3.6 Elastic Properties

Elastic properties are the quantities that represent the deformation resistance of a material under the application of stress within the elastic region [66]. Within the elastic region, the material will regress to its original shape when the stress is reduced. The amount of strain s (deformation) is proportional to the applied stress σ, according to Hooke's law in the linear-elastic region. Due to the directional dependency of stress and strain, a tensor equation is required to explain this behavior as follows [67]:

$$\sigma_{ij} = C_{ijkl} s_{kl}, \tag{3.4}$$

where C_{ijkl} is the elastic stiffness tensor (the elastic constants) of the material. Based on the symmetric nature of the elastic stiffness tensor, its order can be reduced by Voigt notation [68]. Due to the isotropic properties of glass, there are only three non-zero tensor elements, of which only two are independent:

$$C_{44} = \frac{1}{2}(C_{11} - C_{12}). \tag{3.5}$$

Elastic moduli of a material include the Young's modulus E, the shear modulus G, the bulk modulus K and the Poisson's ratio ν. The elastic moduli of an isotropic material are related to the elastic tensor elements by the following equations:

$$C_{11} = \frac{E(1-\nu)}{(1+\nu)(1-2\nu)}, \tag{3.6}$$

$$C_{12} = \frac{E\nu}{(1+\nu)(1-2\nu)}, \tag{3.7}$$

$$C_{44} = G = \frac{E}{2(1+\nu)}. \tag{3.8}$$

The shear, bulk and Young's modulus of glass are on the order of GPa. The Young's modulus and Poisson's ratio extend from 5 to 180 GPa and 0.1 to 0.4, respectively [45].

3.6.1 Ultrasonic Echography Method (USE)

The elastic moduli of a glass can be determined via different methods such as Brillouin scattering (BS), mechanical vibration and the Ultrasonic Echography Method (USE). USE is one of the most convenient techniques used in glass studies [27]. USE takes advantage of the fact that the elastic moduli are related to the speed of sound in isotropic materials such as glass. In order to determine the elastic moduli, the longitudinal velocity (v_L) and transverse velocity (v_T) need to be obtained. v_L and v_T can be obtained by measuring the total travel time of the wave (t) of the polished sample with a known thickness (d), using a thickness gauge. The gauge was calibrated with stainless steel and glass of a known thickness and velocities. Each measurement was repeated at least five times with a standard error of $< 1\%$. Accuracy of the measurements rely on several factors such as the thickness of the glass (less than 1 mm), inhomogeneity of samples (cracks and bubbles), calibration procedure and so on. The elastic moduli can be calculated using both longitudinal and transverse velocities through the following equations [27]:

$$\nu = \frac{1-2(\frac{v_T}{v_L})^2}{2-2(\frac{v_T}{v_L})^2}, \tag{3.9}$$

$$E = \frac{\rho v_T^2(3v_L^2 - 4v_T^2)}{v_L^2 - v_T^2}, \tag{3.10}$$

$$G = \rho v_T^2, \tag{3.11}$$

$$K = \rho\left(v_L^2 - \frac{4}{3}v_T^2\right). \tag{3.12}$$

3.7 Solid-state nuclear magnetic resonance (ssNMR)

Solid-state NMR spectroscopy is a method of probing the structure of glass. In this study, ^{31}P and ^{207}Pb ssNMR were used to probe the local environment of phosphorous and lead, due to the fact that their chemical shielding reflects the underlying structure. The following information is based on the assumption that the reader has basic knowledge of NMR spectroscopy. This section focuses on the aspects of ssNMR which have relevance to this study.

3.7.1 Magic Angle Spinning

Magic angle spinning (MAS) is one of the most widely used techniques in the field of ssNMR. Due to the various interactions in ssNMR such as the quadrupole interaction for $I > 1/2$ and the anisotropy of chemical shielding, the NMR spectra of solids suffer from line broadening. A number of interactions contain the second Legendre polynomial:

$$P_2(\cos\theta_m) = \frac{1}{2}(3\cos^2\theta_m - 1) = 0. \tag{3.13}$$

At magic angle, which is approximately $\theta_m = 54.74^o$ [69], $\cos\theta_m = \frac{1}{\sqrt{3}}$ and the term $P_2(\cos\theta_m)$ is equal to zero. Therefore, the chemical shift anisotropy (CSA), dipolar

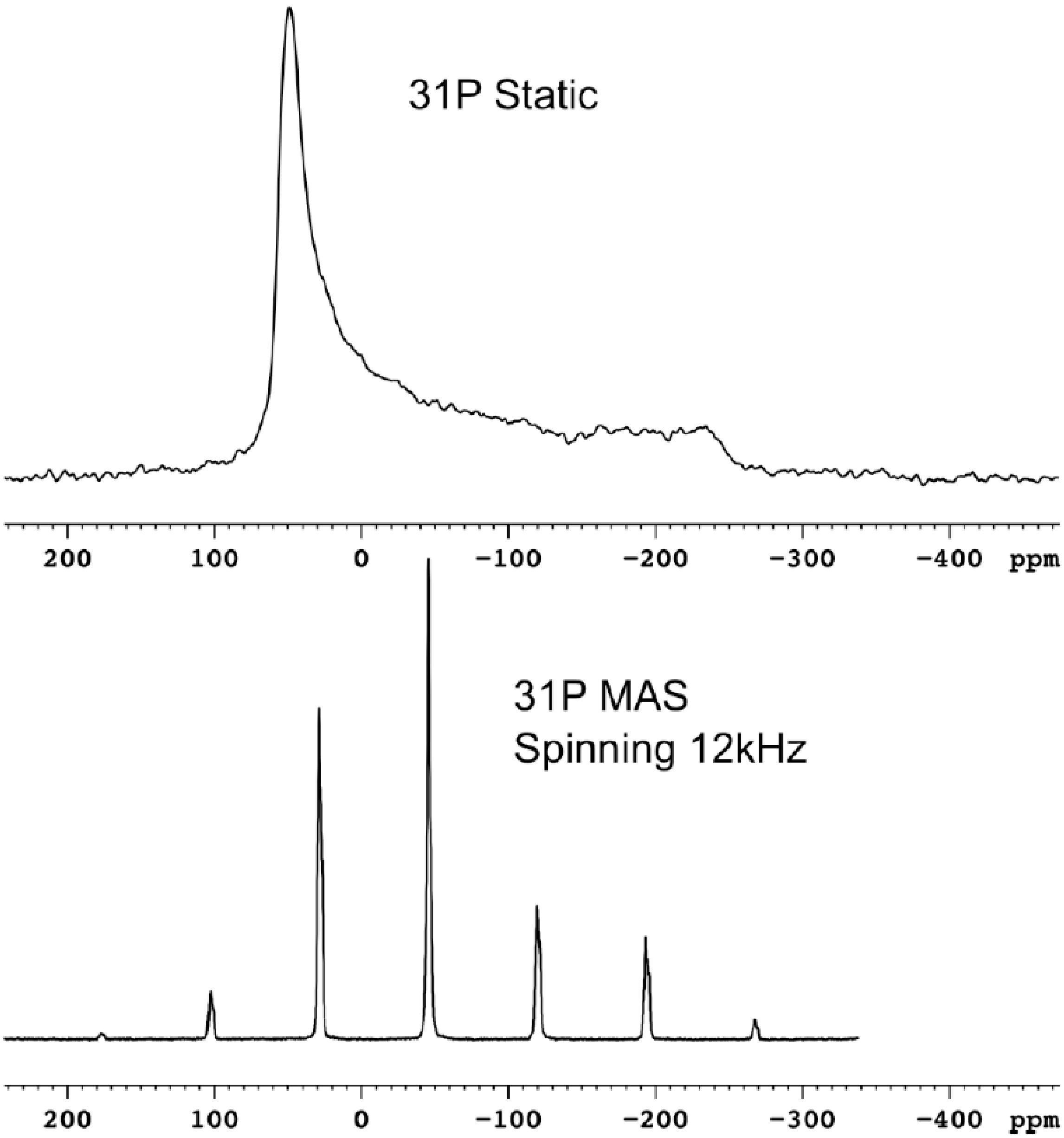

Figure 3.4: Comparison of Static and MAS ^{31}P NMR spectra for P_2O_5. Reprinted with the permission from Dr. Vincent Martin [31].

coupling and first-order quadrupolar interactions are eliminated by using MAS. CSA of ^{31}P spectra is very large in glasses (hundreds of ppm) [70]. The application of MAS results in the splitting of the broad ^{31}P peak into narrow sidebands and the enhancement of resolution (see Figure 3.4).

This technique involves loading the solid sample (usually powder) into a cylindrical container, called a rotor (typically ZrO_2), and then rapidly spinning at an

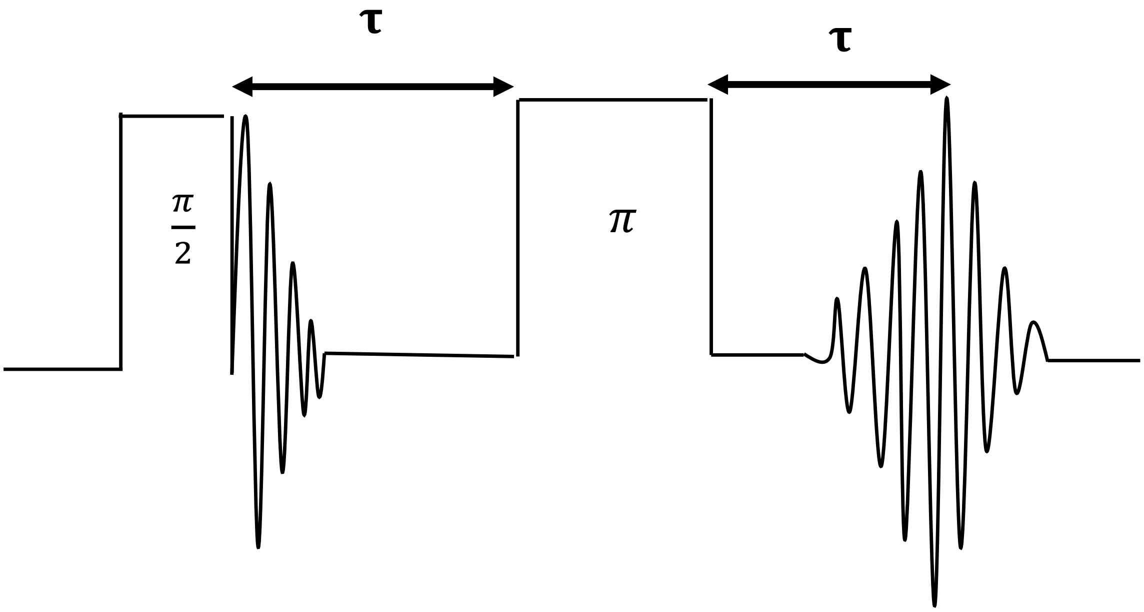

Figure 3.5: Schematic diagram of two successive r.f. pulses. The first pulse generates the FID and the second one creates the spin echo.

aforementioned angle along its symmetry axis. The spinning speed depends on the size of the rotors.

3.7.2 Spin Echo

Even though the main interest of NMR spectroscopy is to take advantage of the relaxation times, there are always other factors such as the inhomogeneous magnetic field that lead to a decay in FID. The inhomogeneity of the static magnetic field causes different spins to precess with different rates. This results in a phase difference and a loss of the transverse magnetization. Furthermore, the beginning of the FID contains so much information which can be distorted due to the dead time problem such as coil-ringing. To overcome these issues, FID can move away from the end of the r.f. pulse by the application of an echo pulse sequence (see Figure 3.5), which was implemented by Erwin Hahn in 1950 [71].

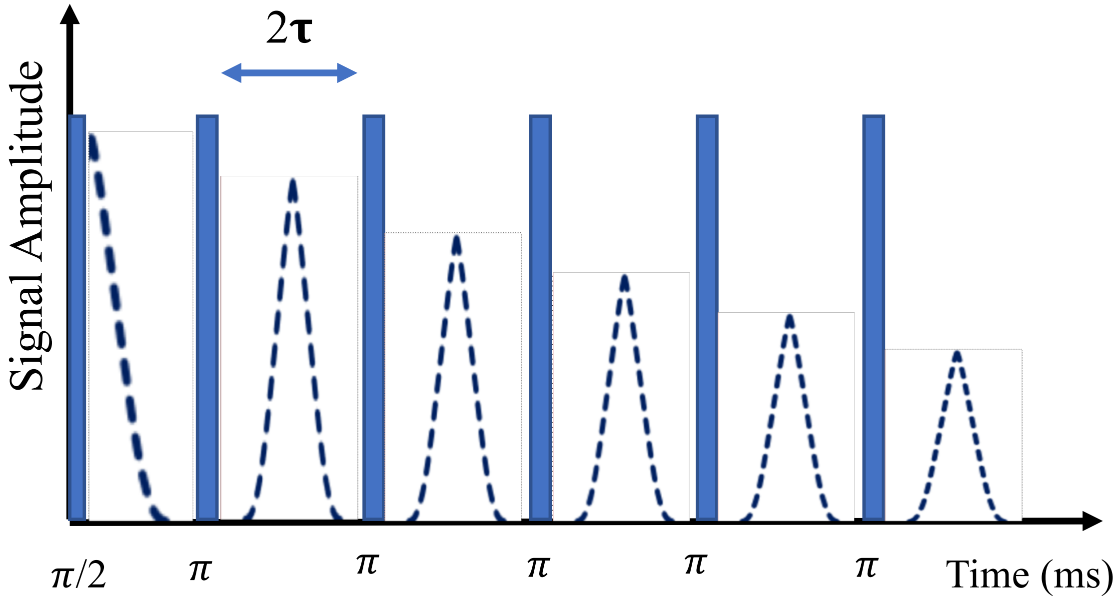

Figure 3.6: Schematic diagram of the CPMG pulse sequence

The introduction of second 180^o pulse refocuses the certain dephased components of the original FID into the spin echo which is generated after τ time of the second pulse. This experiment is also useful for measuring the spin-spin relaxation time (T_2).

3.7.3 The Carr-Purcell-Meiboom-Gill (CPMG) Pulse Sequence

Although the Hahn echo pulse sequence prevent the loss of transverse magnetization and fix the phasing issues, the are still some limitations to this technique. For instance, there is a possibility of random diffusions between spins under the homogeneous magnetic field. This diffusion can lead to an additional loss of spin echo amplitude away from the relaxation. This is more dominant for nuclei with large T_2 such as ^{125}Te. This issue was initially addressed by Carr and Purcell in 1954 [72] and further explored by Meiboom and Gill [73]. The sequence application π pulses after the first $\pi/2$ excitation pulse (known as CPMG pulse sequence) was introduced to neglect the diffusion effect (see Figure 3.6). In this method, a ”train” of spin echoes are generated by repeatedly refocusing the magnetization. After each excitation, the magnitude of the spin echo decays due to the transverse relaxation.

After the Fourier Transformation of the train of echoes, a spectrum consisting of "spikelets" can be obtained. The spacing of the echoes control the density of the spikelets and the intensity of the spikelets delineate the powder pattern of the spectrum. On the one hand, the resolution of the spectrum can be enhanced by the application of more densely packed spikelets with a greater delay between echoes. On the other hand, the greater delay between echoes causes the reduction of the total number of echoes collected. Therefore, echo spacing need to be carefully chosen to have a balance of signal and resolution.

3.7.4 The WCPMG Pulse Sequence

The WCPMG pulse sequence was first implemented by O'Dell and Schurko in 2008 [74]. The WCPMG is the execution of a wideband, uniform rate and smooth truncation (WURST) pulses with the same pulse sequence in CPMG. WURST pulses were initially introduced by Kupce and Freeman in 1995 [75, 76]. WURST pulses have rounded-end cylinder shapes in comparison to the square pulses in CPMG. The time-dependent amplitude (ω_1(t)) and the phase (ϕ) of a WURST-N pulse are given by the following equations:

$$\omega_1(t) = \omega_{max}\left(1- \mid \cos(\frac{\pi t}{\tau_w}) \mid^N \right), \tag{3.14}$$

$$\phi(t) = \pm 2\pi \left\{ \left(\nu_{off} + \frac{\Delta}{2}\right)t - \left(\frac{\Delta}{2\tau_w}\right)t^2 \right\}, \tag{3.15}$$

where ω_{max} is the maximum radio frequency (r.f.) amplitude, τ_w is the pulse duration, N is the number that determines the overall shape of the pulse, Δ is the total frequency sweep width of the pulse and ν_{off} is the offset frequency of the sweep center. The exponent N is typically between 20 and 80. The larger the N number, the sharper and more square truncated the pulse will be. The phase modulation enables the frequency to sweep in both positive (low to high frequencies) and negative (high to low frequencies) directions to provide the homogeneous excitation. In conclusion, the introduction of WURST pulses to CPMG results in lower signal-to-noise ratios, greater bandwidth and greater net integrated intensity. Therefore, the number of collected echoes slightly decrease due to the longer pulse length. This results in faster acquisition time for homogeneous spectral collection in comparison to CPMG pulse sequence.

3.7.5 Ultra-wideline NMR

The chemical shift anisotropy (CSA), dipolar coupling and first-order quadrupolar interactions are eliminated by using MAS, which leads to narrower line widths of spectra. However, in some cases, anisotropic interactions are too large (the line widths exceed into the MHz region) to be approached by MAS. NMR signals of this range are known as ultra-wide line. In most cases, ultra-wide line NMR not only suffers from the broad range of frequencies, but they also have a low natural abundance and gyro-magnetic ratio (*i.e.,* ^{207}Pb). One of the methods to acquire the ultra-wide spectra is the variable offset cumulative spectrum (VOCS) [77, 78]. In VOCS, the main spectrum can be collected in multiple slices (sub-spectra) at different transmitter frequencies.

3.8 Refractive Index

Refractive indices of all glass samples were measured via ATAGO's multi-wavelength Abbe refractometer (DR-M4/1550) at 656 nm. The desirable sample dimension is a glass sample which is 40mm in length, 8mm in width and 1 to 10mm in thickness. Proper contact liquid and interface filter frame were first chosen based on an estimated sample refractive index (The refractive index of contact liquid must be higher than the sample). After that, the sample was placed on contact liquid drip on the center of the prism. The refractive index can be measured with high accuracy (four decimal numbers) by adjusting the boundary line.

3.9 Stress Optic Measurement

The sign of C was determined using a PS-100 Polariscope (Strainoptic) which is also known as a light table. The value of C was measured with the Senarmont compensator method. The PS-100 polariscope is comprised of a light table, linear polarizer, quarter-wave plate and analyzer which are all set up vertically. The loading stage, which includes a stressed sample, is placed on top of the light table and the linear polarizer, while the quarter wave plate and analyzer are attached to a pole standing above them. The induced stress fringe in the sample and corresponding angle are determined visually by rotating the analyzer. Both the Senarmont compensator method and the light table employ the same principle in obtaining the sign and value of C which is illustrated in Figure 3.7.

In the Senarmont method, the light source is 670nm laser diode. The loading stage which includes the stressed sample is placed on a goniometer in accurate alignment with the laser beam. The laser beam initially passes through a linear polarizer and a pinhole to be linearly polarized at 45° with respect to the direction of the uniaxial stress. Then, it will pass through the stressed sample and turn out to be circularly polarized. This elliptical polarization should be linearly polarized again by passing through a liquid crystal variable retarder (LCVR) which acts as a quarter-wave plate. At the end, the intensity of laser beam is measured with a computer-controlled analyzer which can rotate by 20° on both sides of minimum intensity. The intensities are plotted and parabolically fit against different angles to find the extinction angle, θ (minimum transmitted angle). The phase shift Δ can then be calculated by having the intensity of minimum angle through the following equation:

$$\Delta = -2\theta \pm \frac{\pi}{2}, \tag{3.16}$$

and finally the stress-optic coefficient can be found as a slope of σ against Δ plot through the following equation:

$$\Delta = \frac{2\pi d}{\lambda} C\sigma, \tag{3.17}$$

where λ is the wavelength of the laser source, σ is the applied mechanical stress and d is the thickness of the sample.

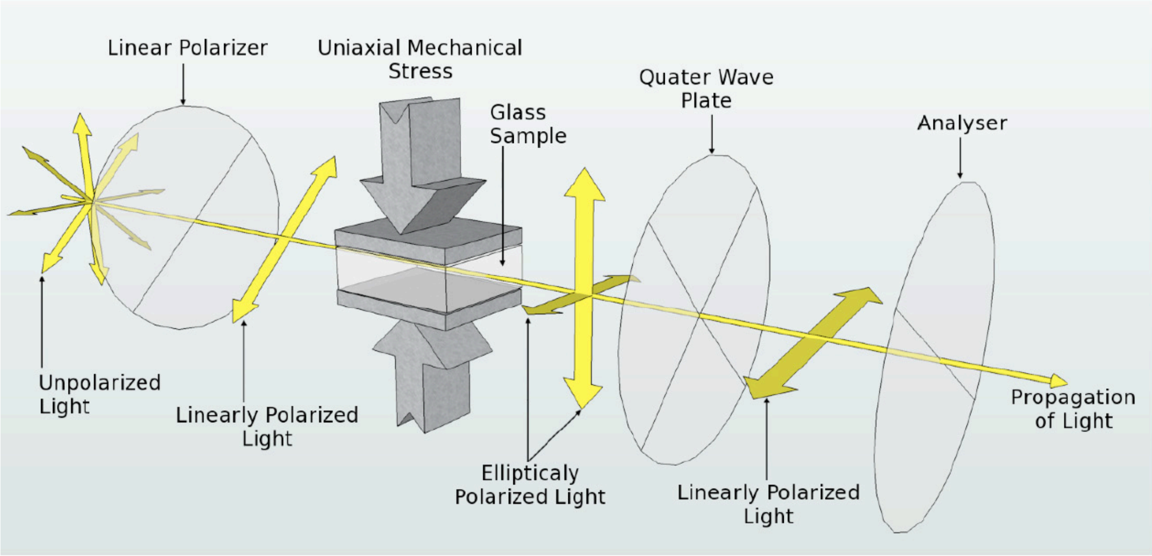

Figure 3.7: Representation of the experimental apparatus to measure the sign and value of C. Reprinted with the permission from Dr. Vincent Martin [31].

Chapter 4

Structural studies, elastic and photoelastic properties

4.1 Introduction

This chapter contains the experimental results and a discussion of the glass systems that have been investigated throughout this study. The results and discussion are presented in the following order: glass preparation, elemental analysis, density measurements, solid-state Nuclear Magnetic Resonance (ssNMR), ultrasonic echography methods (USE), refractive index, and stress optic measurements.

4.2 Glass preparation

All of the glasses in this study were synthesized via the traditional melt-quenching technique. The stoichiometric amounts of the reagents used to produce 10 g of each composition are reported in Table 4.1. The glass making procedure to produce binary and ternary glass families were explained in details in the experimental techniques (see section 3.2). Glass families which were synthesized in this study along with their melting and annealing temperatures, as well as the time required for each steps can be seen in Table 4.2. The range of compositions of interest for this study are reported in Table 1.1.

4.3 X-ray Diffraction

Four samples from each series of glass were selected for the X-ray powder diffraction technique to confirm the amorphous nature of their structure. All diffraction measuremnets in this study were conducted using Siemens D500 equipped with a Cu anode, X-ray tube and monochromator. Angular steps of 0.04^o and dwell times of 1s have been used in this work. Figure 4.1 shows the diffraction pattern of $(PbO)_{0.30}(BaO)_{0.20}(P_2O_5)_{0.50}$, $(PbO)_{0.20}(BaO)_{0.30}(P_2O_5)_{0.50}$, $(PbO)_{0.50}(P_2O_5)_{0.50}$ and

Table 4.1: Mass in grams of the reagents used. See also Table 1.1 for abbreviated names.

Sample	PbO (g)	BaO (g)	$NH_4H_2PO_4$ (g)
60Pb40P	7.0227	0.0000	4.8257
55Pb45P	6.5776	0.0000	5.5470
50Pb50P	6.1127	0.0000	6.3005
40Pb10Ba50P	5.0847	0.8732	6.5513
30Pb20Ba50P	3.9716	1.8188	6.8228
20Pb30Ba50P	2.7622	2.8462	7.1178
10Pb40Ba50P	1.4435	3.9665	7.4394
50Ba50p	0.0000	5.1928	7.7915
55Ba45p	0.0000	5.6901	6.9855

Table 4.2: Melting time and temperature as well as the annealing temperature in a ternary and binary glass families.

Glass family	Melting temperature	Melting time	Annealing temperature
Barium phosphates	$1100 - 1200^oC$	2 hr	$450 - 550^oC$
Lead phosphates	1000^oC	1-2 hr	150^oC
Lead barium phosphates	$1050 - 1200^oC$	2 hr	400^oC

$(BaO)_{0.55}(P_2O_5)_{0.45}$ compositions. None of the spectra show sharp diffraction peaks, which is consistent with amorphous patterns.

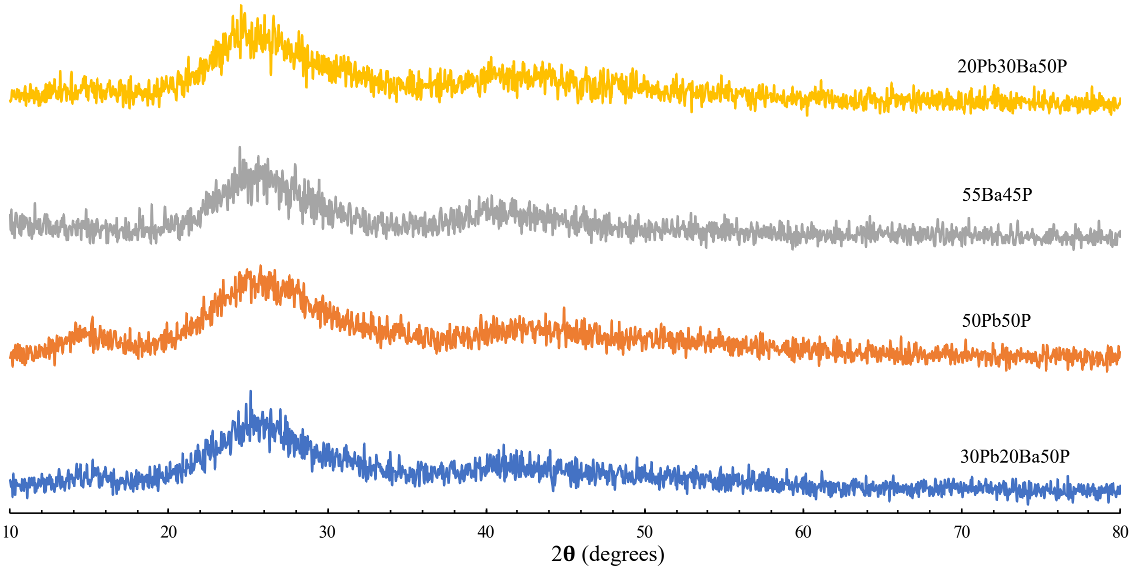

Figure 4.1: X-ray diffraction pattern of $(PbO)_{0.30}(BaO)_{0.20}(P_2O_5)_{0.50}$, $(PbO)_{0.20}(BaO)_{0.30}(P_2O_5)_{0.50}$, $(PbO)_{0.50}(P_2O_5)_{0.50}$ and $(BaO)_{0.55}(P_2O_5)_{0.45}$ compositions. See also Table 1.1 for abbreviated names.

4.4 Elemental Analysis

As described in chapter 3.2, the first series of binary and ternary glass samples (reported in Table 1.1) were synthesized by using $BaCO_3$ as a source of BaO. However, after performing the elemental analysis (WDS) on almost all of the samples, most of them were around 7% far from their nominal compositions, which was a result of the volatile nature of P_2O_5. Due to fact that $BaCO_3$ requires a higher calcination temperature and a longer calcination time compared to other reagents, P_2O_5 could evaporate during this process. To overcome this issue, the calcination procedure for $BaCO_3$ was avoided by using pure barium oxide (BaO, 99.99% trace metals basis, Sigma-Aldrich) as a source of BaO in all the glass families containing BaO. Furthermore, the melting time and temperature were decreased in comparison to the first series. In addition, platinum crucible with a lid was used to prevent the P_2O_5 mass loss. With these procedures, the analyzed sample compositions were brought into much closer agreement with the desired compositions. Quantitative comparison is

Table 4.3: Comparison between experimental and nominal compositions. See also Table 1.1 for abbreviated names.

Sample	PbO (mol%)		BaO (mol%)		P_2O_5 (mol%)	
	Nom.	Expt.($\pm$1)	Nom.	Expt.($\pm$1)	Nom.	Expt.($\pm$1)
50Pb50P	50	52	0	0	50	48
40Pb10Ba50P	40	44	10	9	50	46
30Pb20Ba50P	30	33	20	18	50	47
20Pb30Ba50P	20	23	30	29	50	47
10Pb40Ba50P	10	13	40	39	50	48
50Ba50P	0	0	50	51	50	49

Table 4.4: Density and molar volume of the binary and ternary samples in comparison to the literature results on the same compositions. See also Table 1.1 for abbreviated names.

Sample	Density ($g.cm^{-3}$)	Density($g.cm^{-3}$) [24]	Molar volume ($cm^3.mol^{-1}$)
60Pb40P	5.398(5)	5.42	35.33(3)
55Pb45P	5.008(2)	5.02	37.27(1)
50Pb50P	4.640(3)	4.65	39.34(2)
40Pb10Ba50P	4.453(2)	4.39	39.43(1)
30Pb20Ba50P	4.228(1)	4.19	39.876(9)
20Pb30Ba50P	4.020(1)	4.00	40.20(1)
10Pb40Ba50P	3.808(1)	3.80	40.60(1)
50Ba50p	3.608(1)	3.65	40.92(1)
55Ba45p	3.796(1)	3.84	39.04(1)

provided in Table 4.3 and Figure 4.2 for the 50 mol % P_2O_5 tie-line.

4.5 Density measurements

Densities of all the binary and ternary glass samples were measured via Archimedes' principle. This method was performed using a Mettler Toledo density kit, absolute ethanol and analytical balance. The complete description of the density measurement procedure is explained in section 3.5 of this dissertation. The density of each sample was measured three times showing an acceptable error $<$ 1%. The molar volume of all glass samples were calculated using the acquired density results based on the equation 3.3.

The measured densities and the calculated molar volumes as well as, the density values from the literature [24] on the same compositions are given in Table 4.4.

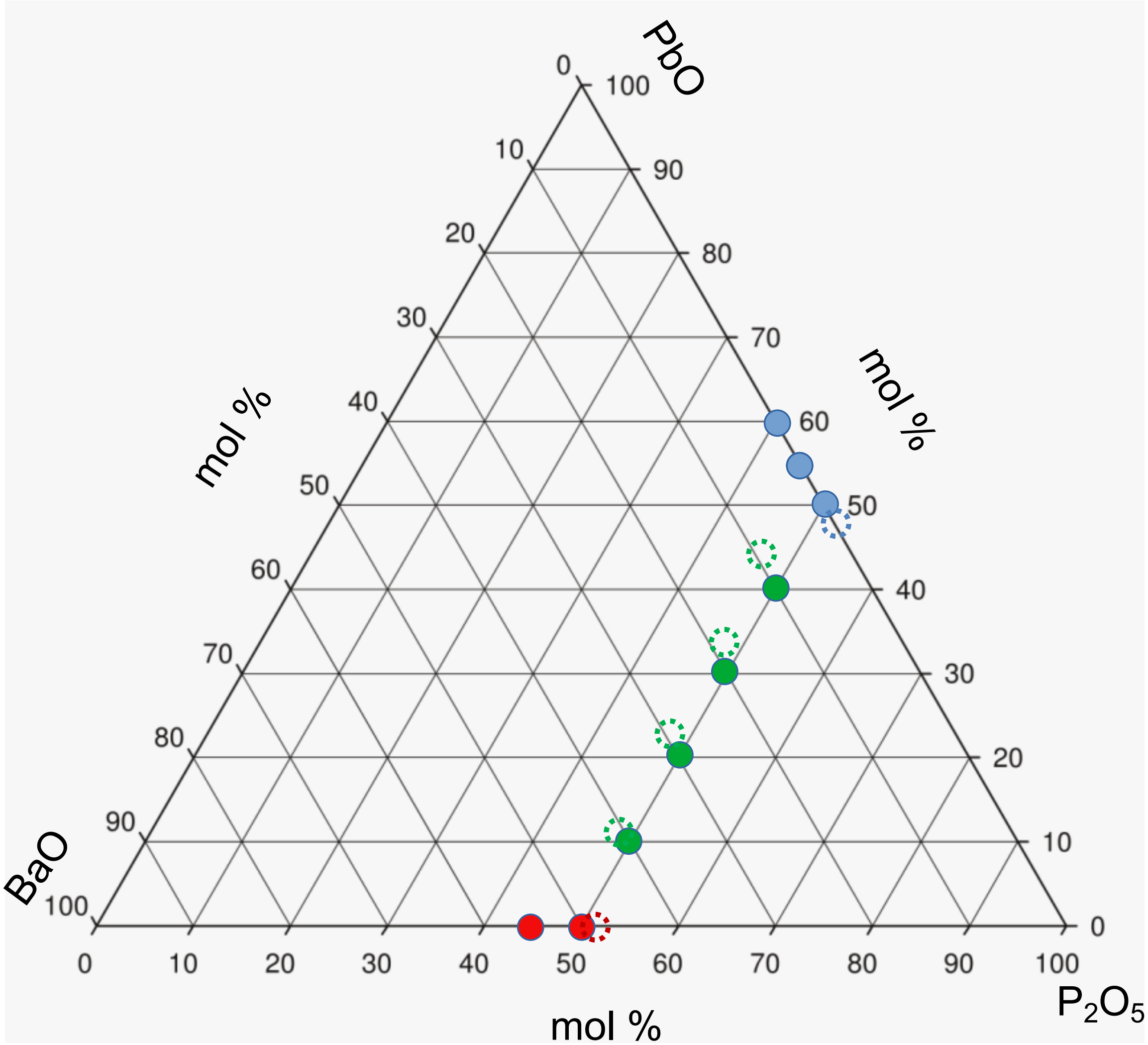

Figure 4.2: Comparison between experimental and nominal compositions. The filled dots are the nominal compositions and the unfilled dots are the experimental compositions.

Almost all of the measured density values are consistent with the literature values, indicating that the measurement procedure was conducted accurately. In all binary and ternary compositions, the increase of PbO content results in an increase in density or decrease in molar volume. The atomic volume and atomic mass of the constituent element can be used to explain this trend. The atomic masses of the Pb, Ba and P atoms are 207.20, 137.33 and 30.97 $g.mol^{-1}$ and their atomic radii are 1.75, 2.17 and 1.10 $\mathring{A}$, respectively. Therefore, the addition of PbO or BaO followed by the decrease in P_2O_5 content in binary lead phosphate or barium phosphate glasses give

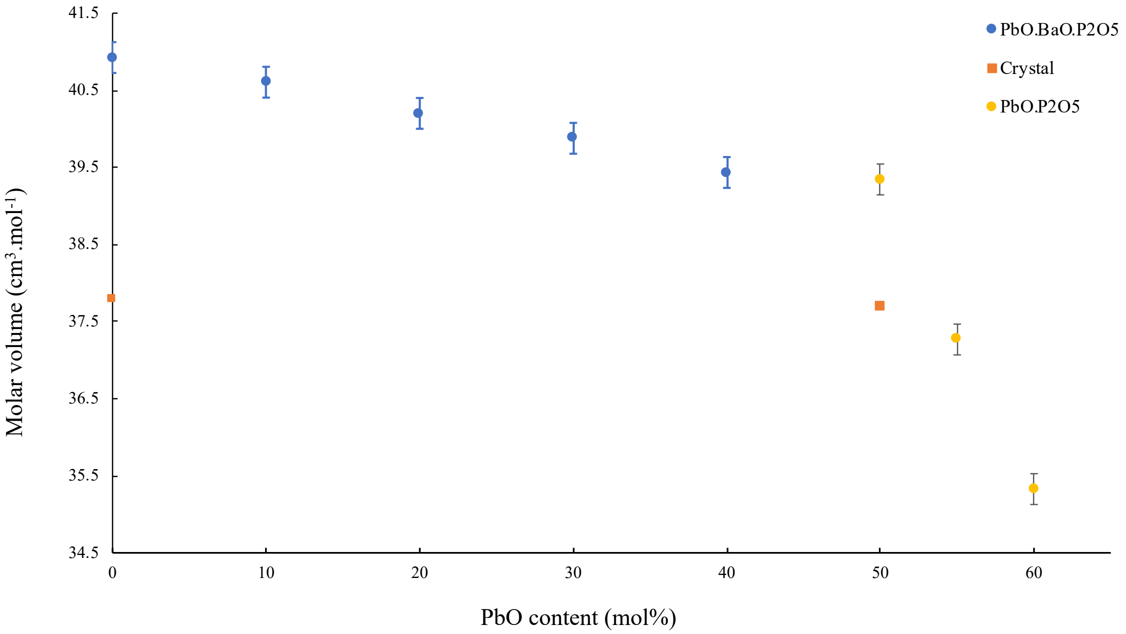

Figure 4.3: Variation of molar volume of all samples as a function of PbO contents.

rise to an increase in their densities and a decrease in their molar volume. It can also be concluded that the incorporation of Pb^{2+} and Ba^{2+} alter the glass structure to have less open space and be more compact by the formation of NBOs in the network. Formation of NBOs can also decrease the network connectivity and network dimensionality of the glass structure.

Due to the fact that the lead has a higher atomic mass and lower atomic radius in comparison to the barium, substitution of the PbO for BaO while the P_2O_5 content remains the same in ternary glass, leads to an increase in their densities and a decrease in their molar volume. Molar volume as a function of PbO and BaO content are shown in Figure 4.3.

Molar volume decreases linearly by replacing BaO with PbO content while P_2O_5 content remains the same. The coordination number of phosphorous and lead remain the same in all of the samples based on the ^{31}P and the ^{207}Pb ssNMR results which are given in section 4.6. One of the main reasons for the change in molar volume can be attributed to the fact that Pb cations have a higher field strength and attract oxygen ions more so than Ba cations in phosphate glasses (Ba-O bond length is longer than Pb-O [2]). Therefore, it is concluded that the substitution of BaO for PbO results in a more compact and less connected structure.

As was explained in section 2.6, crystal structures corresponding to our glass compositions were extracted with the purpose of being compared to our glass. Crystalline compounds density and their derived molar volume values are reported in Table 4.5.

Table 4.5: Density and molar volume of crystalline compounds.

Crystal	Density ($g.cm^{-3}$)	Molar volume ($cm^3.mol^{-1}$)
PbP_2O_6	4.844	37.691
$Pb_2P_2O_7$	6.409	30.595
BaP_2O_6	3.908	37.781
$Ba_2P_2O_7$	4.139	36.124
$BaPbP_2O_7$	5.034	34.328

The density of crystalline compounds is higher than their corresponding glass sample (V_m is lower) due to the fact that the structure of glass is more open than their corresponding crystals. The density of crystalline compounds increases by increasing the PbO or BaO content followed by a reduction in P_2O_5 content. This trend was also observed in Table 4.4 which is pronounced based on the atomic volume and atomic masses of their constituent elements.

As it is reported in Table 4.4, the addition of PbO or BaO content in binary glass compositions results in a decrease trend in their molar volume values which is also observed in their corresponding crystalline compounds (See Table 4.5). The molar volume of lead phosphate crystalline compounds decreases from 37.691 to 30.595 $cm^3.mol^{-1}$ and the molar volume of barium phosphate crystalline compounds decreases from 36.124 to 34.328 $cm^3.mol^{-1}$. This trend is caused by the formation of more NBOs in the structure which alters the structure to have less free space and be more compact. It is also concluded that lead cations can compact the structure more than barium cations. This is explained by the fact that lead cations have a higher field strength which allows them to attract the oxygen atoms more so than barium cations.

Unfortunately, only one crystalline phase corresponding to our ternary glass compositions was found for the purpose comparison. Therefore, we are not able to compare the structural behavior of $BaPbP_2O_7$ compound to different PbO and BaO contents in ternary glass compositions. However, it is concluded that $BaPbP_2O_7$

structure is more compact than the barium phosphate crystalline compounds, but less compact than high lead content crystal ($Pb_2P_2O_7$).

4.6 Solid-State Nuclear Magnetic Resonance

4.6.1 ^{31}P Nuclear Magnetic Resonance Spectroscopy

The ^{31}P ssNMR results were obtained by loading glass powder into a 2.5 mm diameter sample rotor on a Bruker Avance NMR spectrometer with a 9.4 T magnet (162.02 MHz ^{31}P Larmor frequency) using magic angle spinning (see Figure 4.4 to Figure 4.12). $NH_4H_2PO_4$ was used as a secondary reference to scale a ^{31}P chemical shift at 0.81 ppm. Samples were spun at 18 kHz and the final 1-D MAS spectra was obtained with a 0.75 μs pulse. The 90 degree pulse time was determined based on the 20 degree flip angle at 74 kHz r.f. field strength and a 60s recycle delay. All of the spectra with their spinning side bands were fitted by the program Dmfit 20150521 [79].

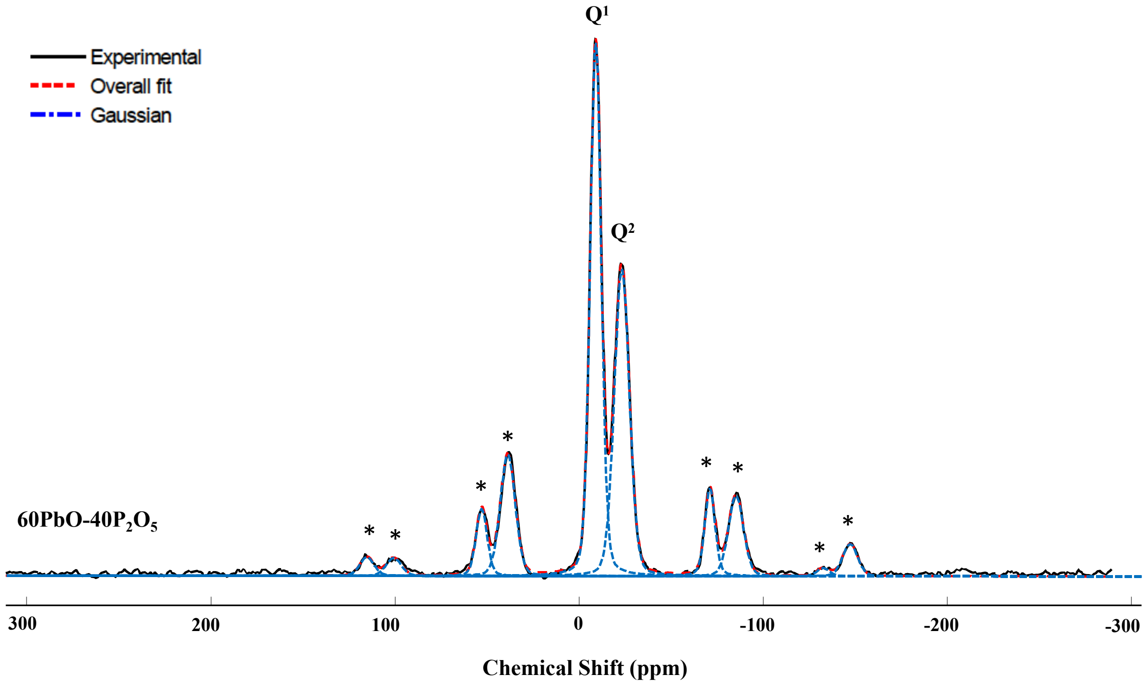

Figure 4.4: Deconvoluted ^{31}P MAS NMR spectra of $(PbO)_{0.60}(P_2O_5)_{0.40}$ glass. The gaussians peaks used to fit the spectrum as well as the spinning side bands.

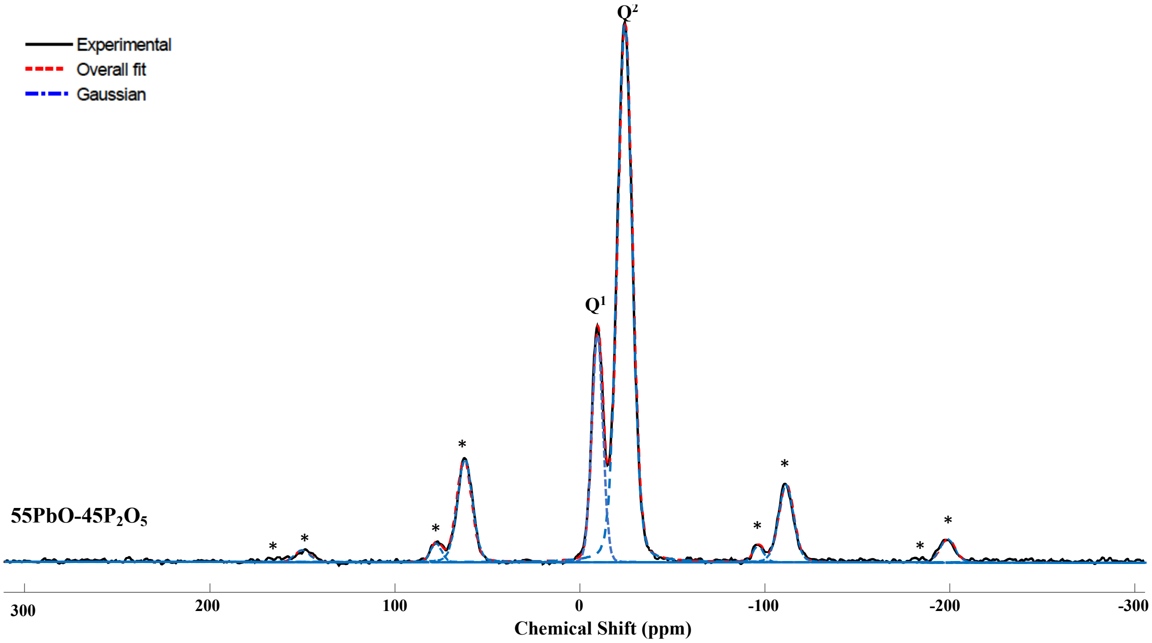

Figure 4.5: Deconvoluted ^{31}P MAS NMR spectra of $(PbO)_{0.55}(P_2O_5)_{0.45}$ glass. The gaussians peaks used to fit the spectrum as well as the spinning side bands.

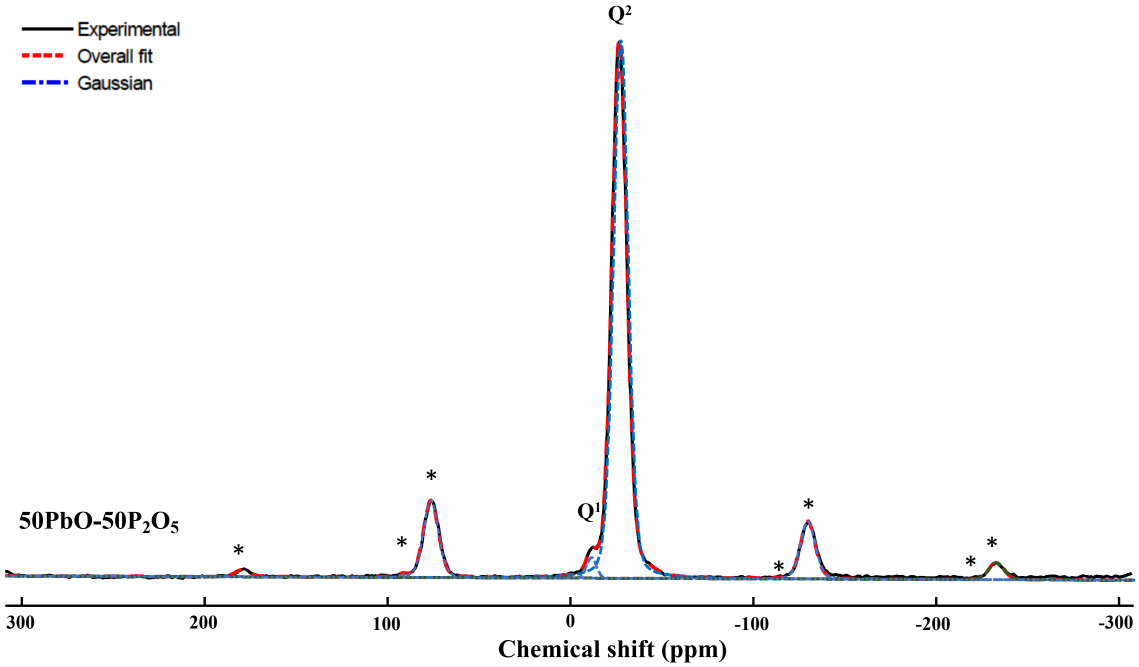

Figure 4.6: Deconvoluted ^{31}P MAS NMR spectra of $(PbO)_{0.50}(P_2O_5)_{0.50}$ glass. The gaussians peaks used to fit the spectrum as well as the spinning side bands.

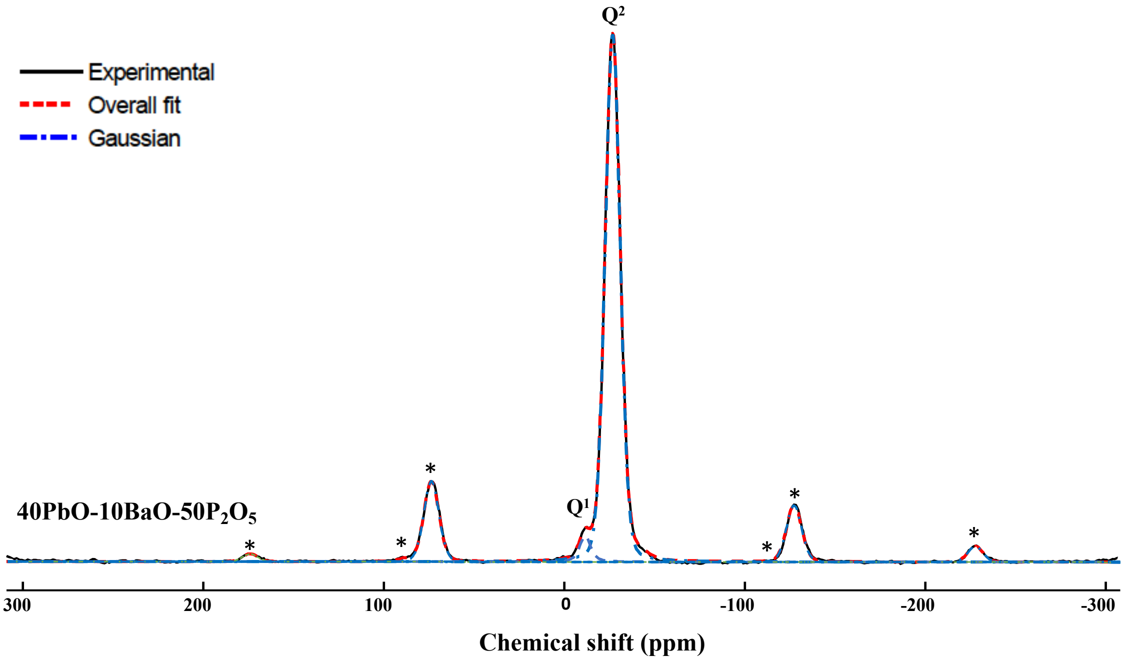

Figure 4.7: Deconvoluted ^{31}P MAS NMR spectra of $(PbO)_{0.40}(BaO)_{0.10}(P_2O_5)_{0.50}$ glass. The gaussians peaks used to fit the spectrum as well as the spinning side bands.

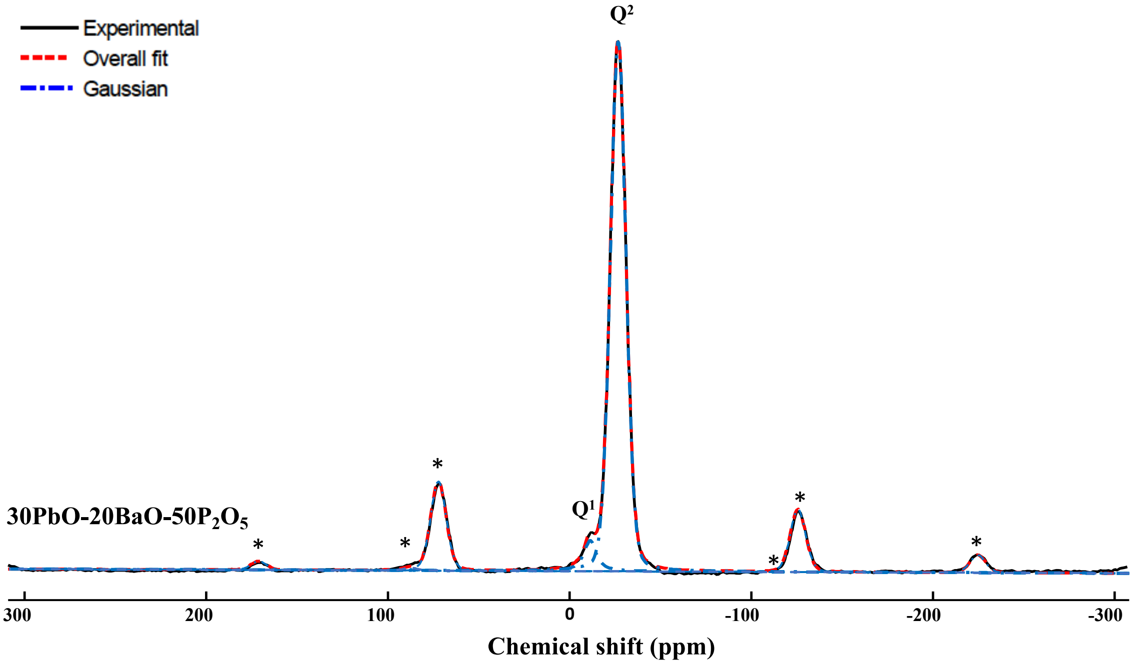

Figure 4.8: Deconvoluted ^{31}P MAS NMR spectra of $(PbO)_{0.30}(BaO)_{0.20}(P_2O_5)_{0.50}$ glass. The gaussians peaks used to fit the spectrum as well as the spinning side bands.

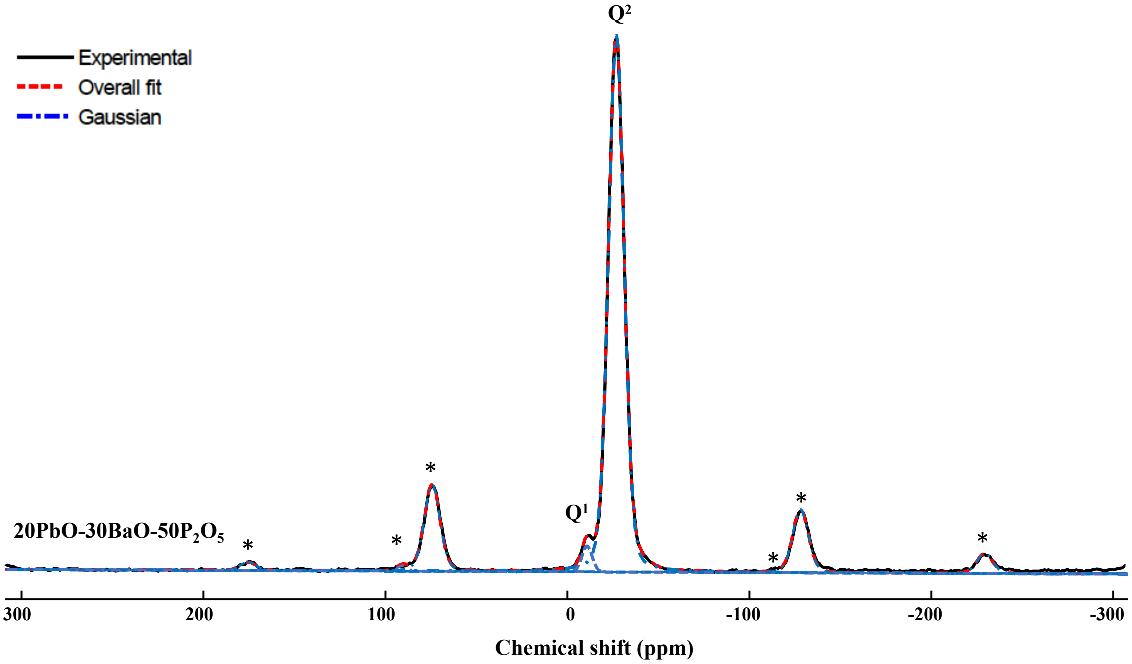

Figure 4.9: Deconvoluted ^{31}P MAS NMR spectra of $(PbO)_{0.20}(BaO)_{0.30}(P_2O_5)_{0.50}$ glass. The gaussians peaks used to fit the spectrum as well as the spinning side bands.

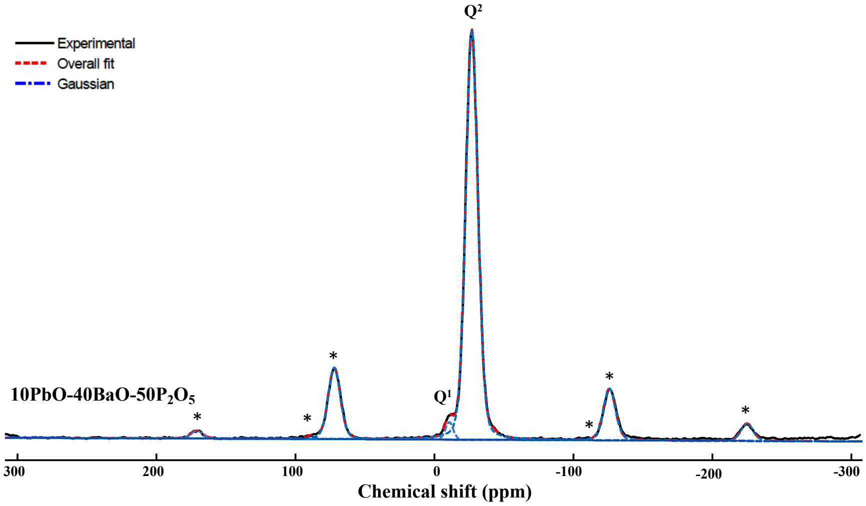

Figure 4.10: Deconvoluted ^{31}P MAS NMR spectra of $(PbO)_{0.10}(BaO)_{0.40}(P_2O_5)_{0.50}$ glass. The gaussians peaks used to fit the spectrum as well as the spinning side bands.

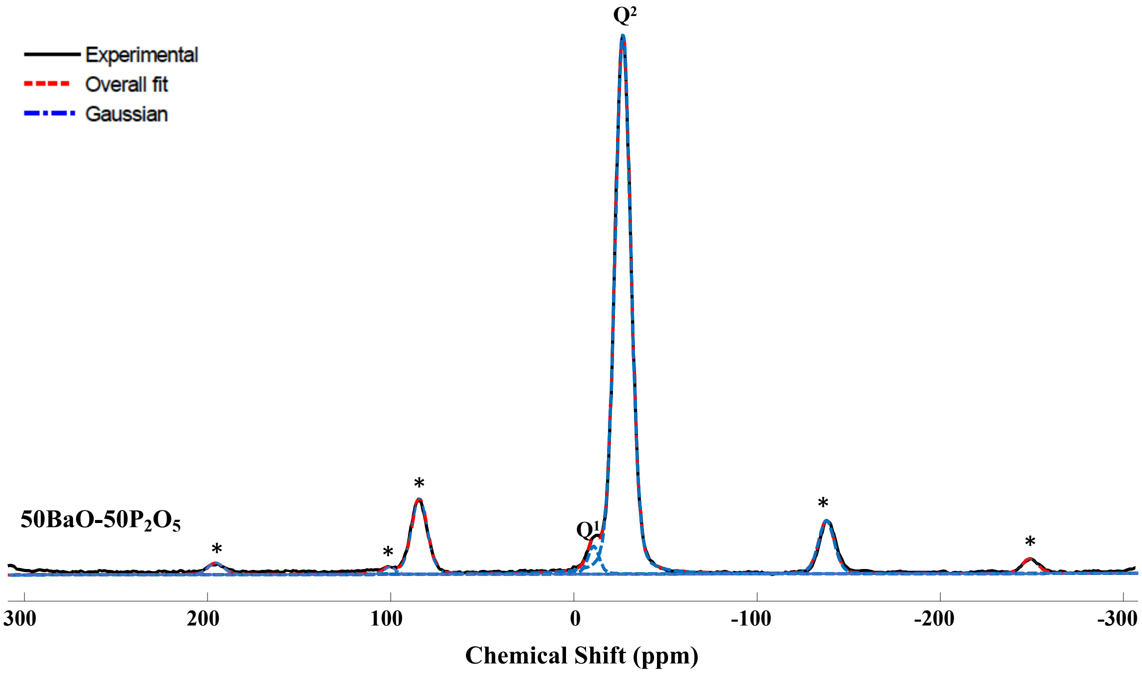

Figure 4.11: Deconvoluted ^{31}P MAS NMR spectra of $(BaO)_{0.50}(P_2O_5)_{0.50}$ glass. The gaussians peaks used to fit the spectrum as well as the spinning side bands.

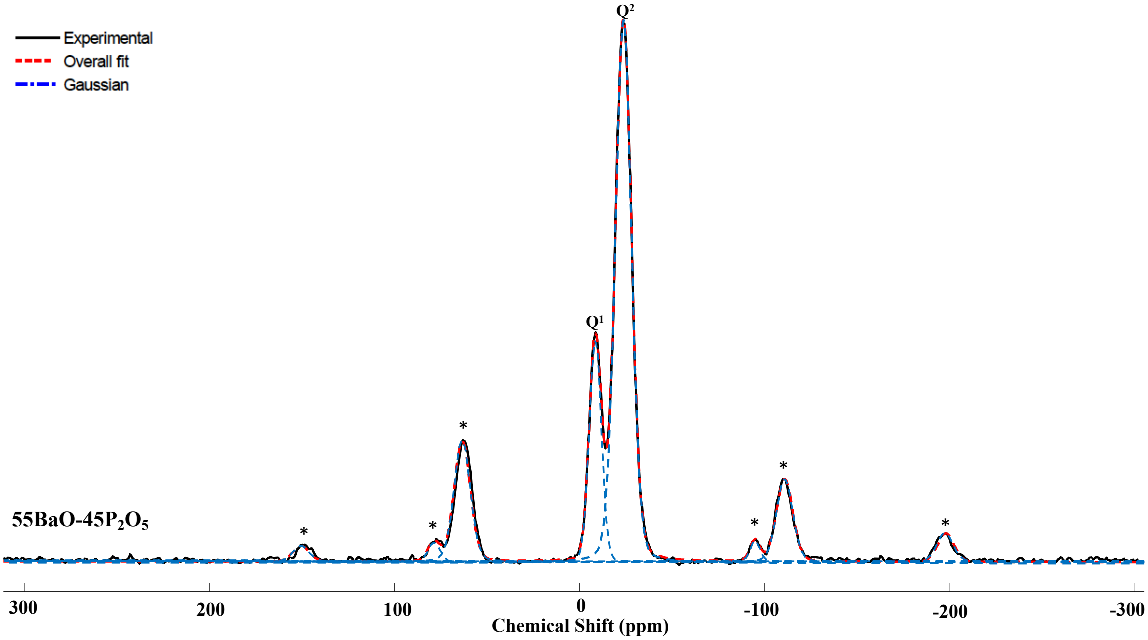

Figure 4.12: Deconvoluted ^{31}P MAS NMR spectra of $(BaO)_{0.55}(P_2O_5)_{0.45}$ glass. The gaussians peaks used to fit the spectrum as well as the spinning side bands.

Table 4.6: ^{31}P isotropic chemical shifts of Q^n species and their fraction. See also Table 1.1 for abbreviated names.

Composition	Q^1		Q^2	
	δ(ppm)	Fraction (%)	δ(ppm)	Fraction (%)
60Pb40P	-9.05	41.11	-23.25	50.85
55Pb45P	-9.51	18.42	-24.31	80.28
50Pb50P	-11.43	2.96	-26.71	96.95
40Pb10Ba50P	-11.51	3.42	-26.74	96.24
30Pb20Ba50P	-11.23	4.77	-26.69	94.85
20Pb30Ba50P	-10.72	2.83	-26.8	96.65
10Pb40Ba50P	-10.61	2.12	-26.86	97.17
50Ba50P	-10.68	3.57	-26.7	96.43
55Ba45P	-8.69	18.26	-23.87	81.32

The ^{31}P MAS NMR revealed the presence of three overlapping isotropic peaks with δ values around -11, -26 and -40 ppm for all the binary and ternary lead phosphate glasses containing 50% mol P_2O_5 content with their associated spinning side bands (labeled with asterisks). These three isotropic peaks are referred to Q^1, Q^2 and Q^3 sites based on the ^{31}P chemical shift in a previous investigation on lead phosphate glasses [80]. The ^{31}P spectra were fitted with Gaussian line shapes for each Q^n species. The isotropic chemical shifts along with their fraction of each Q^n sites were extracted for each glass composition. Assignment of the ^{31}P isotropic chemical shifts of Q^n species as well as their fraction are shown in Table 4.6.

As reported in Table 4.6, the ^{31}P isotropic chemical shifts varies with the glass compositions. The ^{31}P isotropic chemical shifts of the individual peaks increase slightly (become less shielded) with the addition of PbO and BaO content in binary lead phosphate and barium phosphate glasses. This trend was also observed in other binary phosphate glass compositions [19, 37, 38]. The increase in chemical shifts is explained by a decrease in the average bond order (π-bonding within the P-O bonds), which is caused by the formation of more NBOs as well as the increase in the ionic nature of NBOs [37]. Furthermore, in binary glasses, the amount of Q^1 species increases significantly with the addition PbO and BaO content. This variation is caused by the termination of Q^2 units which leads to the depolymerization of the phosphate network. This depolymerization is caused by the creation of more NBOs and a progressive reduction in a phosphate chain length [2].

The termination of Q^2 species has been observed based on the crystalline phases of their corresponding glass compositions. As shown in Figure 2.7 and Figure 2.5, crystalline compounds corresponding to 50 mol% P_2O_5 are comprised of long chain and rings of PO_4 tetrahedra which are coordinated with the cations through the weaker ionic bonds. However, the addition of PbO and BaO above 50 mol% creates more NBOs with an increase in the Ba-O and Pb-O coordination numbers. Therefore, the length of phosphate chains and rings becomes shorter and shorter until the structure is comprised of diphosphate anions ($[P_2O_7]$(See Figure 2.8 and Figure 2.6).

Consistent with previous investigations, as well as the crystalline phases given in section 2.6, the ^{31}P MAS NMR spectrum of the phosphate glasses with around 50%mol P_2O_5 are associated with an intense isotropic peak at around -24 ppm which corresponds to dominant Q^2 sites involved in polymer-like chains or rings [81]. These chains or rings are linked by an ionic bonds between lead or barium cations and NBOs that can also be seen in their corresponding crystalline compounds (PbP_2O_6 in Figure 2.7 and BaP_2O_6 in Figure 2.5).

The last isotropic chemical shift at about -40 ppm which corresponds to the Q^3 sites. Its fraction is negligible in comparison to other units even though it was taken into account in our simulation.

^{31}P MAS NMR spectra of the binary and ternary glasses containing 50% mol P_2O_5 content are shown in Figure 4.13. Due to the fact that P_2O_5 content remains constant in all of the ternary compositions, the isotropic chemical shifts and their fraction for both Q^1 and Q^2 units are approximately similar throughout the samples.

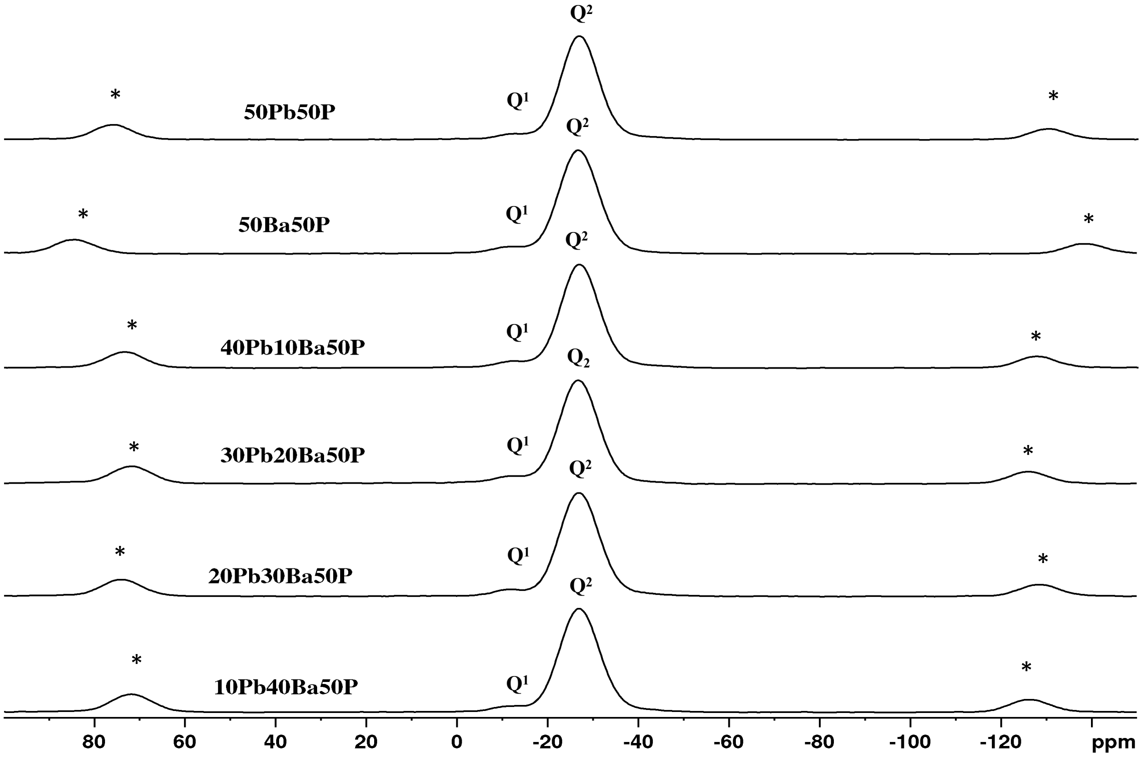

Figure 4.13: ^{31}P MAS NMR spectra (18 kHz spinning speed) of binary and ternary phosphate glasses containing 50% mol P_2O_5 content. The asterisks mark spinning sidebands. See also Table 1.1 for abbreviated names.

4.6.2 ^{207}Pb Nuclear Magnetic Resonance Spectroscopy

^{207}Pb ssNMR spectra of all binary and ternary glasses were obtained with a Bruker Avance NMR spectrometer on a 9.4 T (83.7 MHz ^{207}Pb Larmor frequency)(see Figure 4.14 to 4.20). Samples were loaded into 7 mm glass bulb rotors after being finely ground in a mortar and pestle. All of the ssNMR spectra were acquired by implementing the WCPMG pulse sequence under static conditions [74]. The WURST-800 pulses of 15μm duration with 500 kHz width were implemented to perform a homogeneous excitation. The number of echoes were collected based on the T_2 relaxation time of each sample which were roughly between 60 to 250. The transmitter offset of either 50 kHz or 100 kHz were conducted to acquire spectral slices. Based on the lead content of the sample, between 128 and 800 number of scans per slice were used. The total experimental time was around 2 hours, depending on the optimized recycle delay (5 sec), number of scans and number of slices. ^{207}Pb chemical shifts were referenced to $Pb(NO_3)_2$ solid and all of the spectra were fitted by the program Dmfit 20150521 [79].

All of the ^{207}Pb ssNMR spectra were decomposed to 3 Gaussian peaks which were reported in Table 4.7. All samples express ultra wide peaks typical of ^{207}Pb ssNMR. For binary compositions, a slight evolution from a lower chemical shift to a higher one was observed by increasing the molar fraction of PbO, which is consistent with previous studies [82–84]. For ternary systems, the chemical shifts remain the same throughout different compositions. Consequently, the lead environment and the Pb-O coordination number remained unchanged. However, the intensity of the spectrum increased with the increase of PbO content (See Figure 4.21). At $(PbO)_{0.60}(P_2O_5)_{0.40}$ composition, only two Gaussian peaks with low chemical shifts were required to fit the spectrum. A third Gaussian peak appeared in all other compositions.

At high content, lead was expected to act ionically with a high coordination number as $[PbO_6]$ to $[PbO_9]$ based on its corresponding crystalline phases (PbP_2O_6 and $Pb_2P_2O_7$) which can be seen in Figure 2.7 and Figure 2.8.

The ^{207}Pb WCPMG NMR spectra also indicate that the ionic environment of lead does not evolve with the composition. An estimate of lead coordination number was obtained based on its chemical shift which was obtained from an investigation by Fayon *et al.* [83]. The lead coordination number was found to be 6 or 7 based on

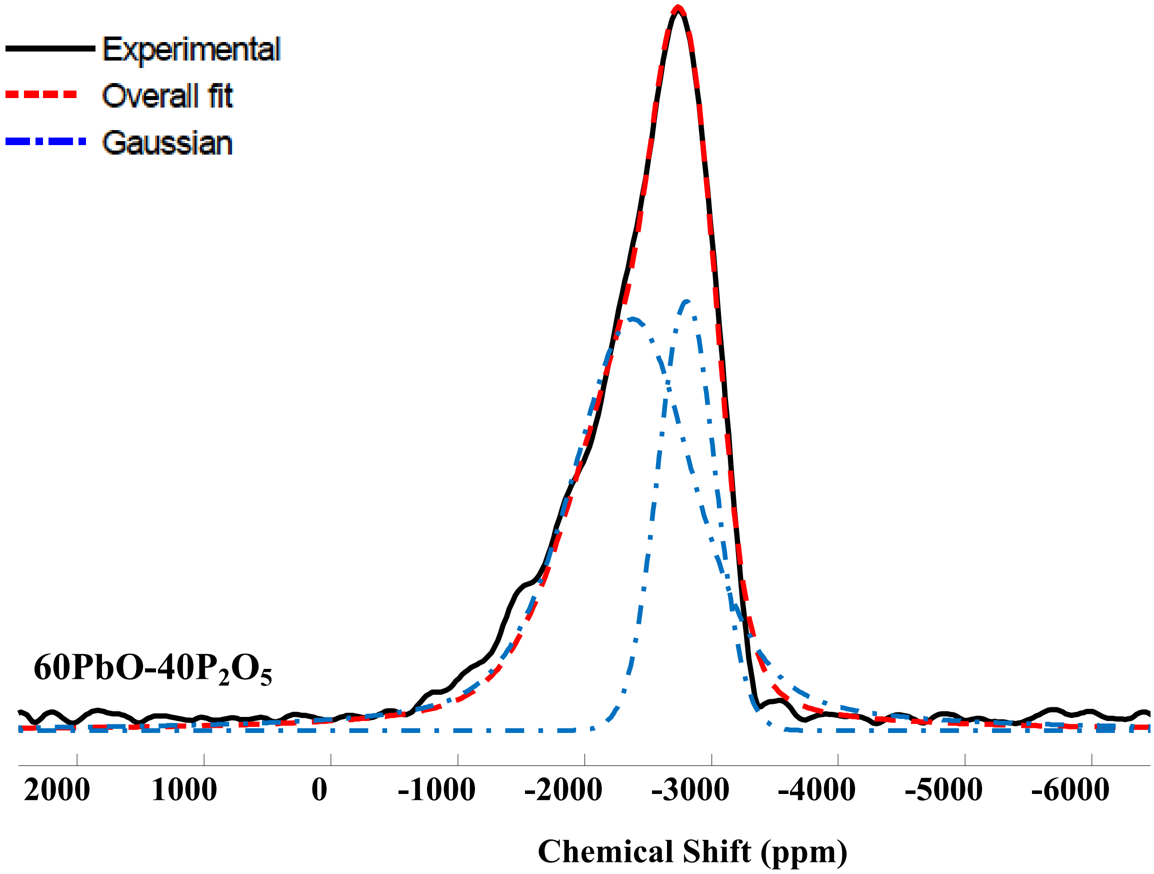

Figure 4.14: Deconvoluted ^{207}Pb NMR spectra of $(PbO)_{0.60}(P_2O_5)_{0.40}$ glass. The Gaussian peaks used to fit the spectrum are also displayed. The parameters used to fit this spectrum are reported in Table 4.7.

the low chemical shift region. This estimation is consistent with other investigations on lead environment that used various spectroscopic methods, such as ^{207}Pb NMR [82, 83, 85], ^{31}P MAS NMR [80], Raman and infrared spectroscopy [19] and EXAFS [86]. Furthermore, all of the investigations on lead local environment confirmed that an increase in PbO content in lead phosphate glasses give rise to a progressive depolymerization of phosphate networks and a decrease in the Pb-O bond length.

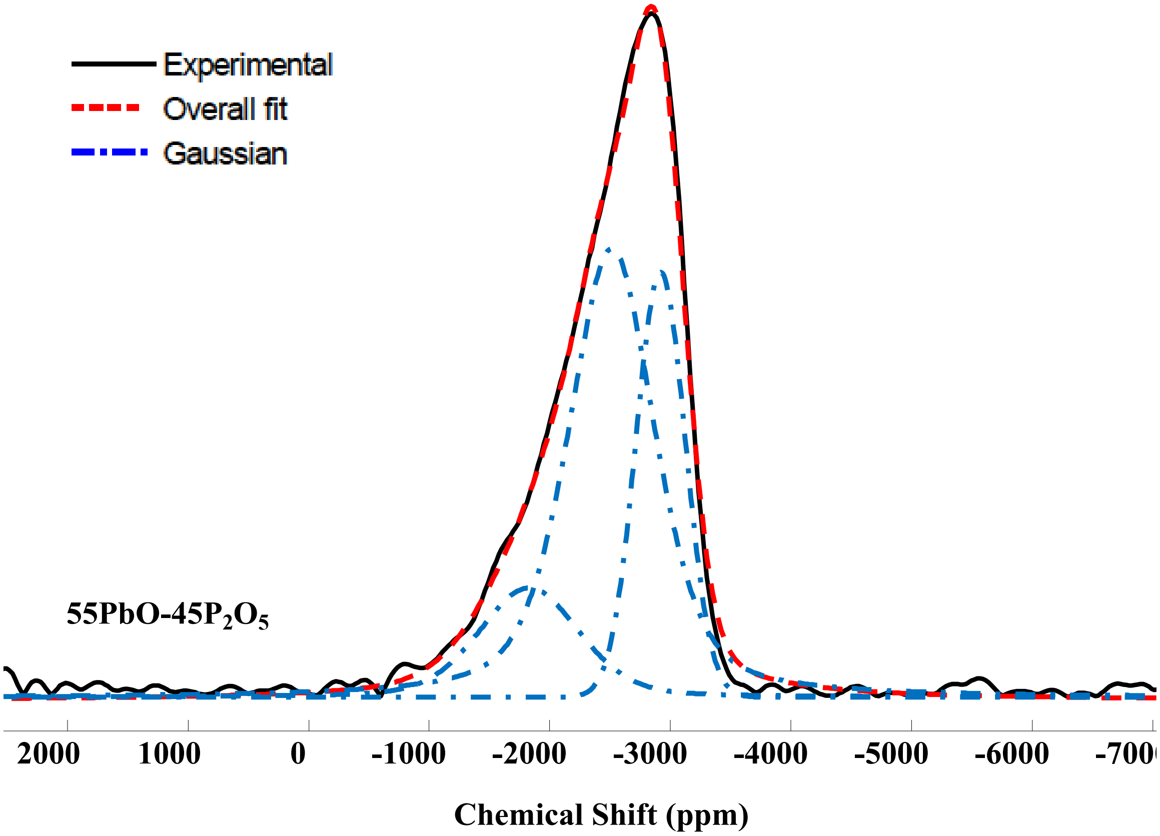

Figure 4.15: Deconvoluted ^{207}Pb NMR spectra of $(PbO)_{0.55}(P_2O_5)_{0.45}$ glass. The Gaussian peaks used to fit the spectrum are also displayed. The parameters used to fit this spectrum are reported in Table 4.7.

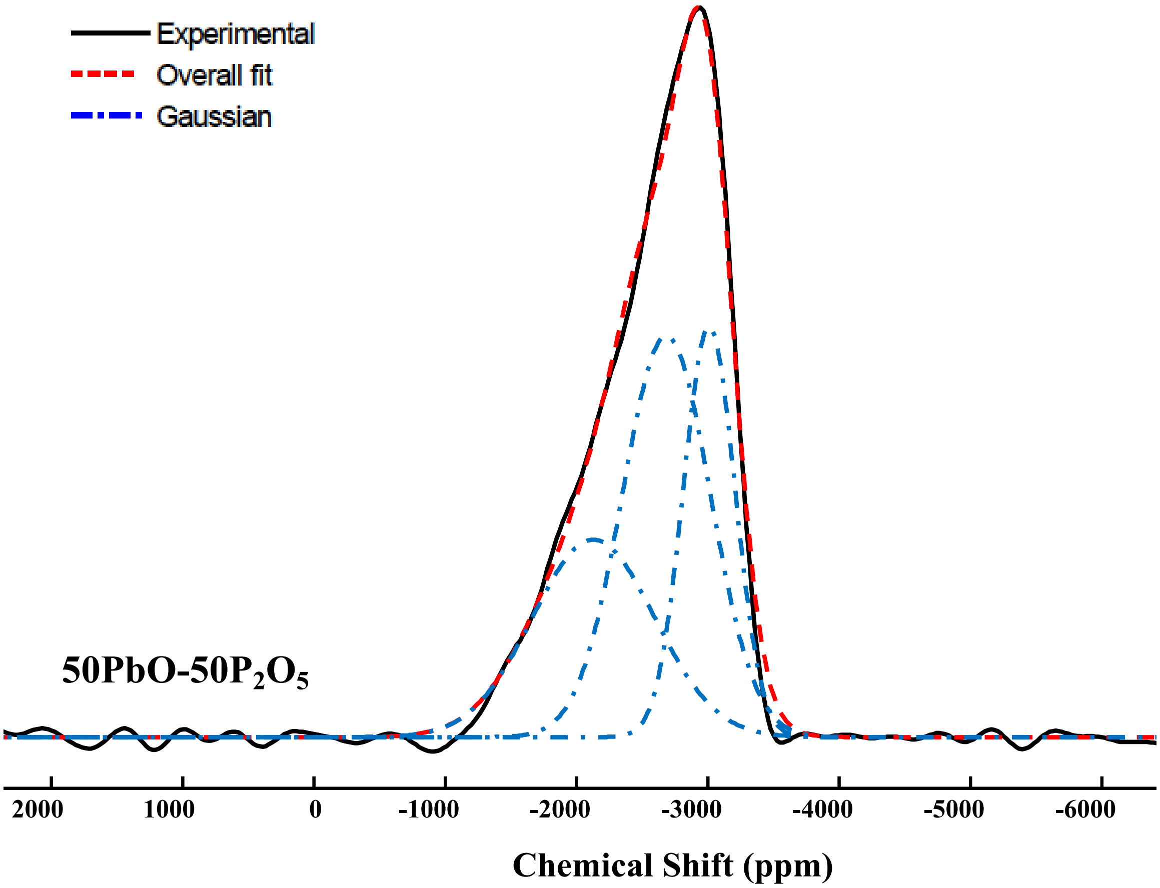

Figure 4.16: Deconvoluted ^{207}Pb NMR spectra of $(PbO)_{0.50}(P_2O_5)_{0.50}$ glass. The Gaussian peaks used to fit the spectrum are also displayed. The parameters used to fit this spectrum are reported in Table 4.7.

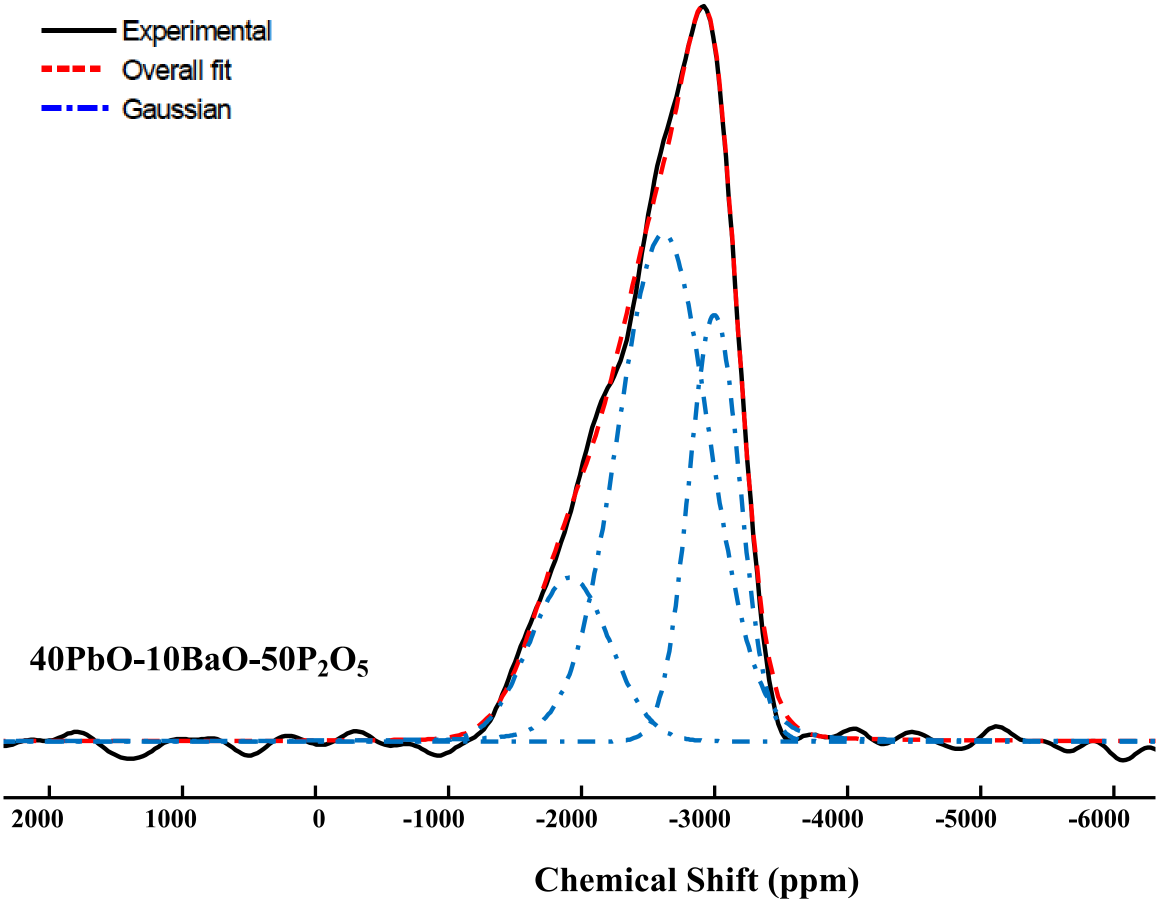

Figure 4.17: Deconvoluted ^{207}Pb NMR spectra of $(PbO)_{0.40}(BaO)_{0.10}(P_2O_5)_{0.50}$ glass. The gaussians peaks used to fit the spectrum are also displayed. The parameters used to fit this spectrum are reported in Table 4.7.

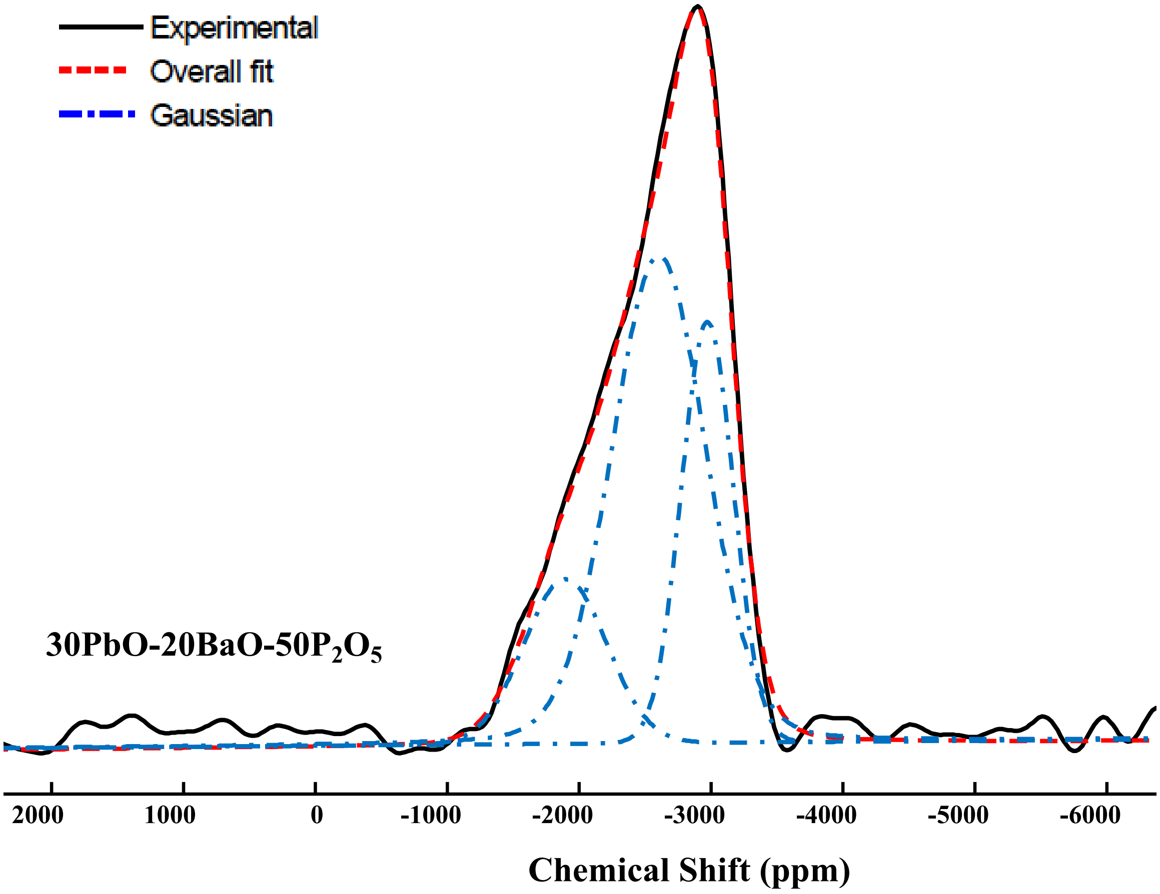

Figure 4.18: Deconvoluted ^{207}Pb NMR spectra of $(PbO)_{0.30}(BaO)_{0.20}(P_2O_5)_{0.50}$ glass. The Gaussian peaks used to fit the spectrum are also displayed. The parameters used to fit this spectrum are reported in Table 4.7.

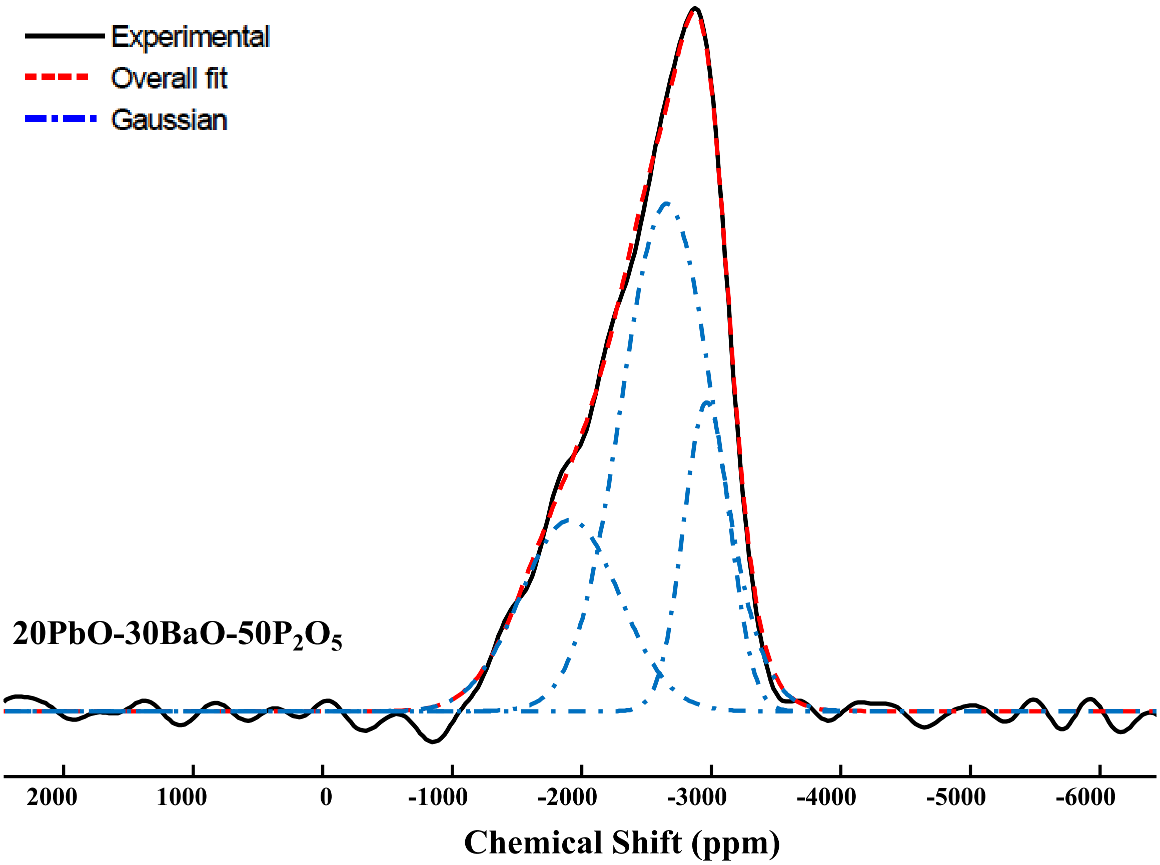

Figure 4.19: Deconvoluted ^{207}Pb NMR spectra of $(PbO)_{0.20}(BaO)_{0.30}(P_2O_5)_{0.50}$ glass. The Gaussian peaks used to fit the spectrum are also displayed. The parameters used to fit this spectrum are reported in Table 4.7.

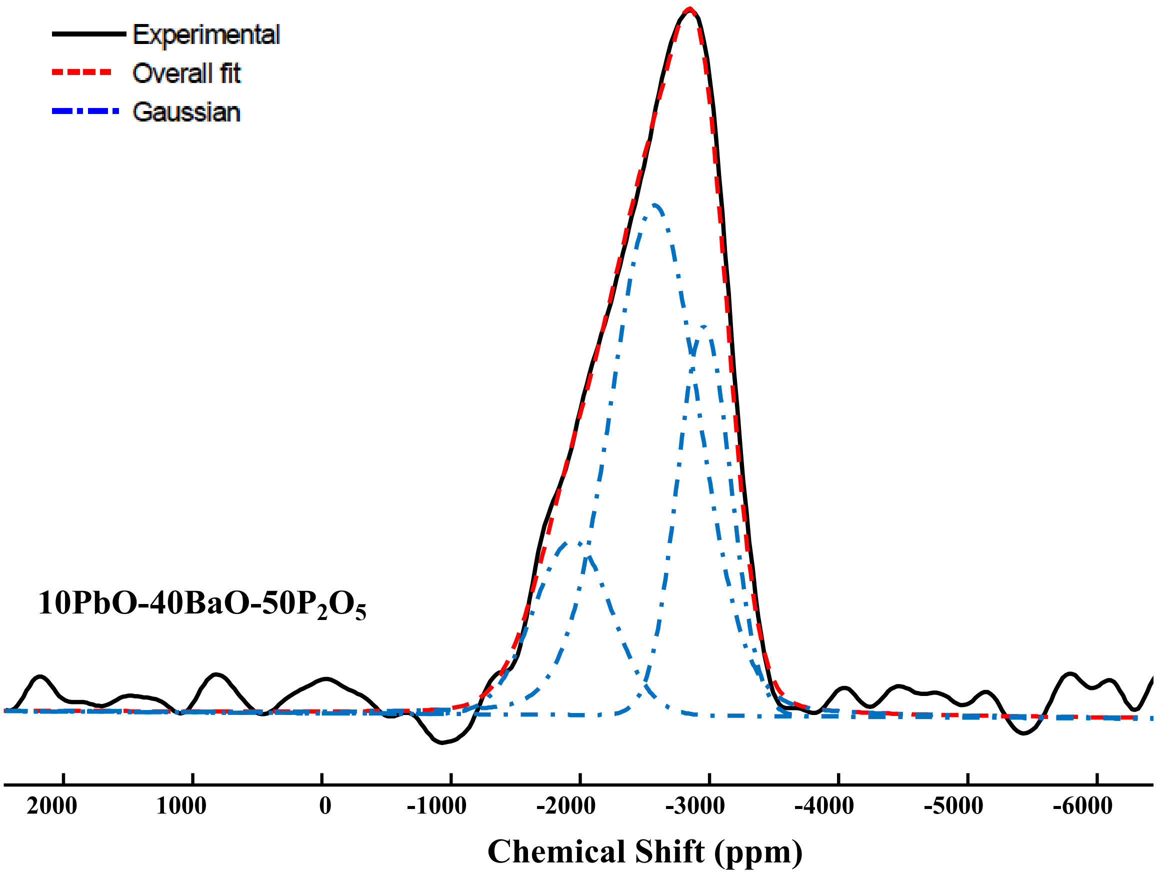

Figure 4.20: Deconvoluted ^{207}Pb NMR spectra of $(PbO)_{0.10}(BaO)_{0.40}(P_2O_5)_{0.50}$ glass. The Gaussian peaks used to fit the spectrum are also displayed. The parameters used to fit this spectrum are reported in Table 4.7.

Table 4.7: Deconvolution of the ^{207}Pb WCPMG NMR spectrum (Figure 4.14 to 4.20). The table columns include glass composition, chemical shift of Gaussian δ, width of Gaussian $\Delta\delta$, relative area of each Gaussian peak, and coordination number of Pb-O N_c. See also Table 1.1 for abbreviated names.

Glass sample	δ ppm, $\pm$140	$\Delta\delta$ ppm, $\pm$240	Area	N_c
60Pb40P	-2802	532	28.7	7
	-2381	1168	71.3	6
55Pb45P	-2918	482	26.4	7
	-2513	846	58.2	6
	-1826	980	15.3	6
50Pb50P	-3010	464	26.3	7
	-2684	789	43.8	6
	-2129	1096	29.9	6
40Pb10Ba50P	-2997	453	26.3	7
	-2615	813	57.9	6
	-1911	710	15.9	6
30Pb20Ba50P	-2972	466	26.1	7
	-2604	842	57.6	6
	-1894	740	16.2	6
20Pb30Ba50P	-2966	424	18	7
	-2658	835	58.3	6
	-1909	902	23.7	6
10Pb40Ba50P	-2957	487	25.3	7
	-2574	805	58.2	6
	-1938	708	16.5	6

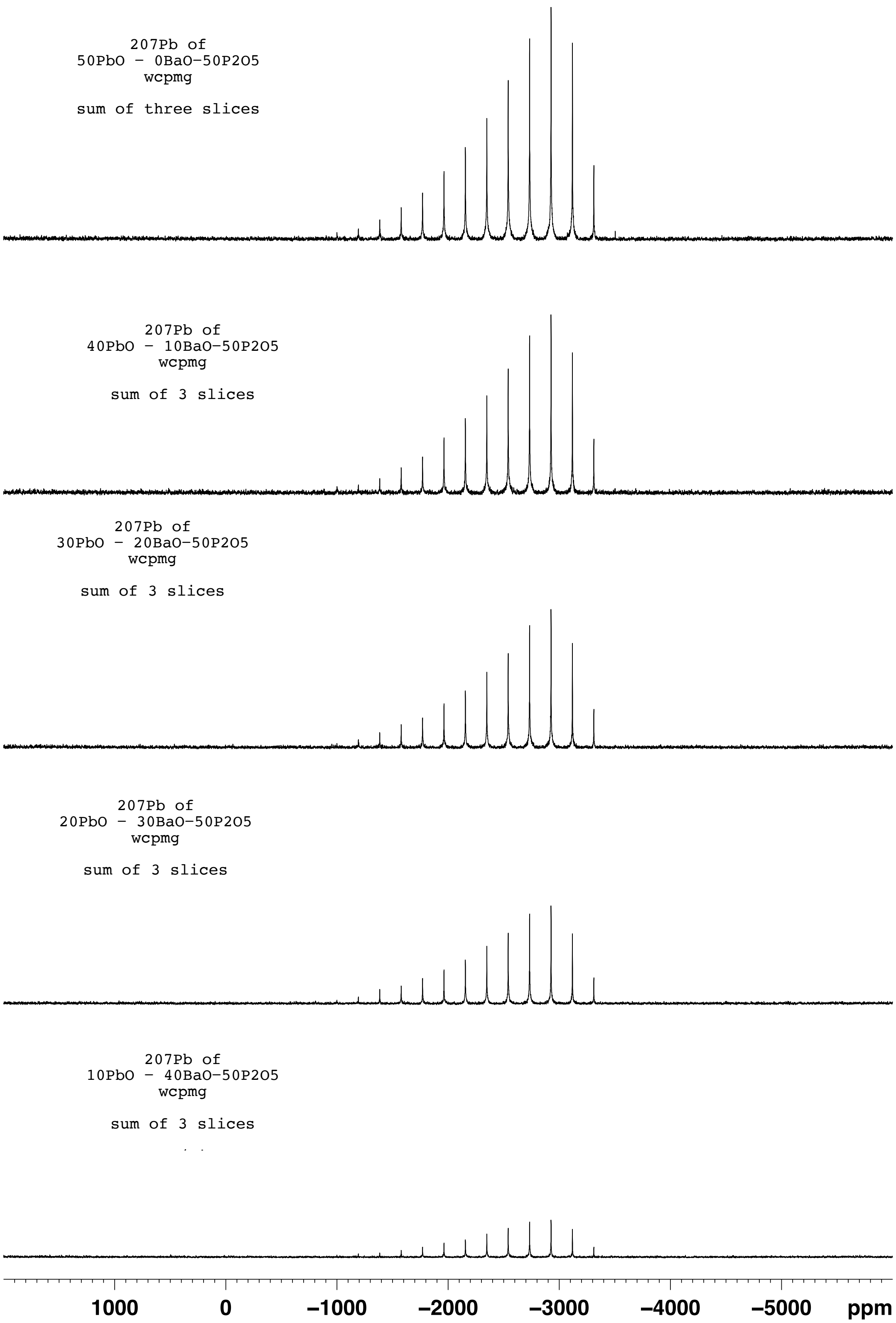

Figure 4.21: The ^{207}Pb WCPMG NMR spectra for all samples containing 50% mol P_2O_5 content at 9.4T. The spectra are provided as WCPMG spikelet patterns with relative intensities.

4.7 Elastic properties

The molar volume (V_m) of the binary and ternary samples, along with their longitudinal and transverse sound velocities (V_l and V_t), calculated elastic constants (Longitudinal modulus (C_{11}) and Shear modulus ($C_{44} = G$)), Poisson ratio (ν), Bulk modulus (K), and Young's modulus (E) are reported in Table 4.8.

The longitudinal (v_L) and shear (v_T) velocities in binary and ternary compositions with different PbO content(mol%) are depicted in Figure 4.22. The measured longitudinal and transverse velocity values were approximate to the measured v_L and v_T values of the same compositions from other studies [23, 24], which confirms that the ultrasonic velocity measurements was conducted accurately.

For almost all of our samples, both velocities v_L and v_T decrease slightly with the increase of PbO or BaO content. It has been proven that the speed of sound in solids is inversely proportional to their densities [87]. Therefore, based on our density values reported in Table 4.4, the addition of PbO in both binary and ternary compositions results in an increase in density and decrease in v_L and v_T.

Figure 4.23 shows the variation of elastic moduli: C_{11}, C_{44}, K and E as a function of mol% of PbO. On one hand, the values of elastic moduli depict an increasing pattern with the increase of PbO content in binary $(PbO)_x(P_2O_5)_{100-x}$ (x from 50 to 60) compositions which was observed in another investigation on similar compositions [6]. On the other hand, the values of elastic moduli show a decreasing trend by replacing BaO with PbO content in ternary $(PbO)_x(BaO)_{50-x}(P_2O_5)_{50}$ (x=10 to 50) compositions.

The interstitial incorporation of Pb or Ba ions followed by a creation of NBOs result in the depolymerization of the phosphate network and the breakdown of the P-O-P bonds which are replaced by ionic bonds between Pb or Ba ions and singly bonded oxygen (formation of P-O-Pb or P-O-Ba linkages) [2].

Table 4.8: The glass compositions, molar volume (V_m), longitudinal and transverse sound velocities (V_l and V_t), calculated elastic constants (Longitudinal modulus (C_{11}) and Shear modulus ($C_{44} = G$)), Poisson ratio (ν), Bulk modulus (K), and Young's modulus (E) of binary and ternary glass samples. See also Table 1.1 for abbreviated names.

Compositions	V_m ($cm^3.mol^{-1}$)	V_l ($km.s^{-1}$)	V_t ($km.s^{-1}$)	C_{11} (GPa)	C_{44} (GPa)	ν	K (GPa)	E (GPa)
60Pb40P	35.33(3)	3.311(1)	1.745(4)	59.14(1)	16.43(1)	0.308(4)	37.26(1)	42.9(4)
55Pb45P	37.27(1)	3.317(1)	1.785(5)	55.10(1)	15.96(2)	0.296(5)	33.83(2)	41.4(6)
50Pb50P	39.34(2)	3.330(4)	1.837(1)	51.46(2)	15.676(3)	0.281(4)	30.55(2)	40.2(3)
40Pb10Ba50P	39.43(1)	3.437(3)	1.832(3)	52.60(2)	14.94(1)	0.302(4)	32.67(1)	38.9(3)
30Pb20Ba50P	39.876(9)	3.567(1)	1.91(4)	53.85(1)	15.42(1)	0.299(4)	33.28(2)	40.1(4)
20Pb30Ba50P	40.20(1)	3.730(3)	2.016(5)	55.93(2)	16.34(2)	0.294(5)	34.15(1)	42.3(6)
10Pb40Ba50P	40.60(1)	3.834(1)	2.084(5)	56.36(2)	16.54(2)	0.290(5)	34.30(2)	42.7(6)
50Ba50P	40.92(1)	4.022(1)	2.147(1)	58.36(1)	16.629(4)	0.301(1)	36.184(5)	43.3(1)
55Ba45P	39.04(1)	4.149(6)	2.276(1)	65.36(4)	19.664(4)	0.309(6)	39.14(4)	44.9(7)

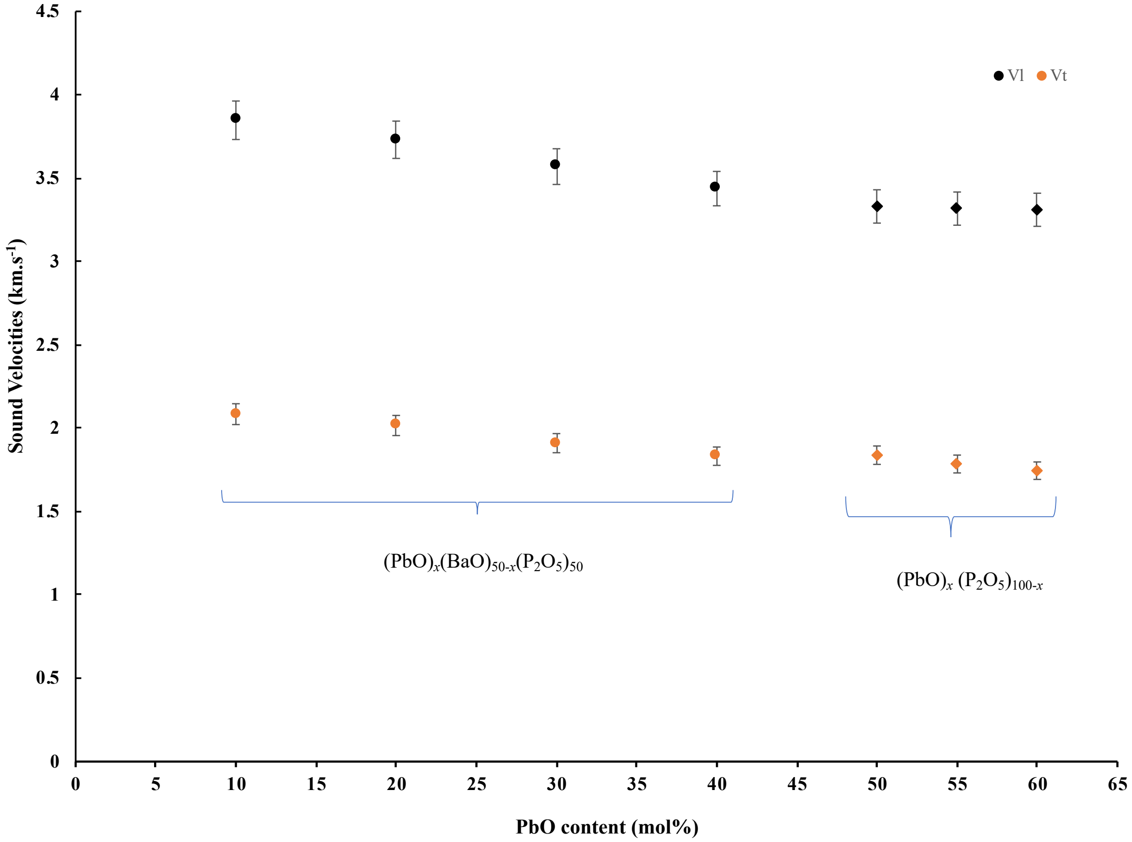

Figure 4.22: Longitudinal and transverse sound velocities (v_L and v_T) as a function of PbO content(mol%) in binary and ternary compositions.

As for the ^{31}P ssNMR results of $(PbO)_{50}(P_2O_5)_{50}$ and $(BaO)_{50}(P_2O_5)_{50}$ compositions which are reported in section 4.6.2, their networks are comprised of phosphate chains and rings(Q^2 tetrahedra) which are connected through ionic bonds between Pb or Ba cations and NBOs. The addition of PbO or BaO above 50 mol% causes more ions to fill up the network and the length of phosphate chains become shorter (termination of Q^2 by Q^1 tetrahedra) [2].

All of the ^{207}Pb ssNMR data in section 4.6.2 along with the coordination number of Pb in the lead phosphate crystalline phases (reported in section 2.6) as well as the Raman and infrared spectroscopy of another investigation on the same compositions [19], confirm that lead acts ionically with high coordination numbers (6 or 7) in all of our glass structures and the Pb-O bond length decreases as the lead content increases.

Crystalline phases of barium phosphate (BaP_2O_6 and BaP_2O_7) which are given

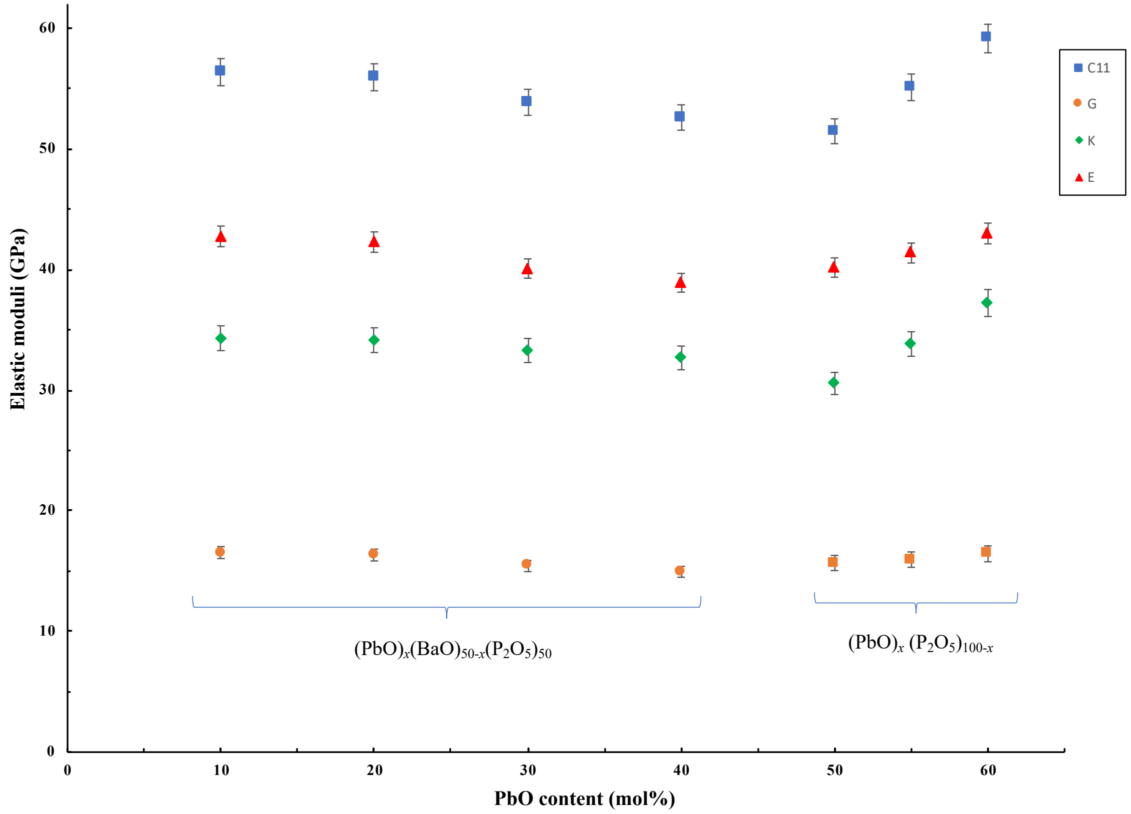

Figure 4.23: Variation of elastic moduli (GPa) as a function of PbO content (mol%) in binary and ternary compositions.

in section 2.6 combined with the information from other studies confirm that Ba ions enter the glass network interstitially and can coordinate ionically with 8 or 9 oxygen atoms [2, 32, 50]. Therefore, the incorporation of Pb and Ba cations alter the glass structure to be more compact and less connected which is consistent with a decrease trend observed in their molar volume values (reported in Table 4.8 and Table 4.5).

Although the rupture of the phosphate network is supposed to reduce the elastic moduli, simultaneous incorporation of Pb and Ba ions (the increase in packing density) reduce the average atomic spacing and increase the inter-atomic forces during the elastic deformation. This leads to an increasing trend in elastic moduli. This trend was also observed in another study on the same compositions [6].

Elastic properties of various glass compositions have been found to be simultaneously correlated to their molar volume V_m and their inter-atomic bonding energy [45]. For instance, the bulk modulus of a solid (K) can be expressed based on the following equation [88]:

$$K = V_o(\frac{\partial^2 U}{\partial V^2})_{V_o} = \frac{mn}{9V_o}U_o, \tag{4.1}$$

where V_o is the equilibrium atomic volume, $V_m \sim N_A V_o$, N_A is the Avogadro number , U_o is the atomic bonding energy and m and n are the exponents explaining the attractive and the repulsive terms. Figure 4.24 shows a different correlation between K and V_m for ternary compositions from $(PbO)_{0.10}(BaO)_{40.0}(P_2O_5)_{0.50}$ to $(PbO)_{40.0}(BaO)_{0.10}(P_2O_5)_{0.50}$, and binary compositions from $(PbO)_{0.50}(P_2O_5)_{0.50}$ to $(PbO)_{60.0}(P_2O_5)_{0.40}$.

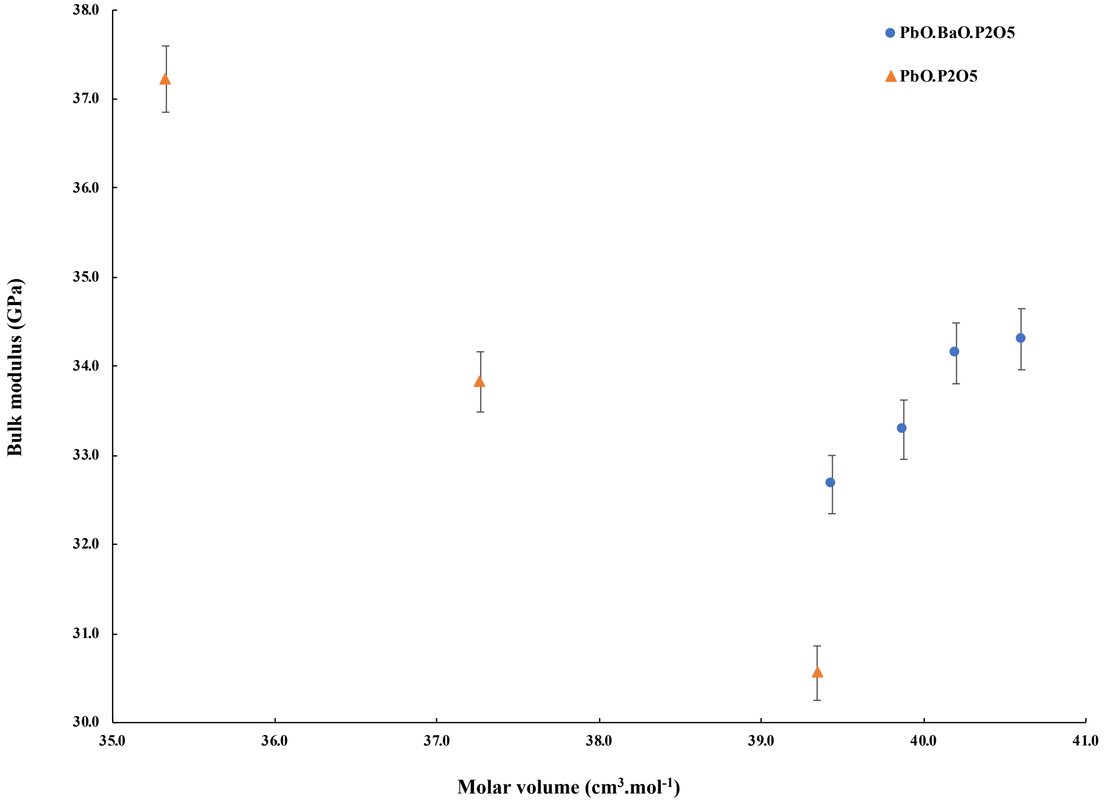

Figure 4.24: Variation of Bulk modulus as a function of molar volume V_m for ternary compositions from $(PbO)_{0.10}(BaO)_{40.0}(P_2O_5)_{0.50}$ to $(PbO)_{40.0}(BaO)_{0.10}(P_2O_5)_{0.50}$, and binary compositions from $(PbO)_{0.50}(P_2O_5)_{0.50}$ to $(PbO)_{60.0}(P_2O_5)_{0.40}$

As it is shown in Figure 4.24, the bulk modulus decreases from 37.226 to 30.555 GPa by increasing the molar volume for binary glasses which can be explained by the inverse effect of their molar volume on the bulk modulus based on the equation 4.1. However, the bulk modulus increases by increasing the molar volume for ternary glasses. This trend can be explained based on the higher inter-atomic bonding energy of Ba-O in comparison to Pb-O ($U_{oBa-O}(562 \text{ kJ/mol}) > U_{oPb-O}(382 \text{ kJ/mol})$) [89], which can compensate the inverse effect of molar volume on bulk modulus and increase them from 32.673 to 34.305 GPa. The same correlation was observed in other glasses [6, 45].

Figure 4.25 and Figure 4.26 depict a similar tendency between shear modulus (G) and Young's modulus(E) with molar volume V_m for ternary and binary compositions. These trends were observed in an investigation of similar compositions [6].

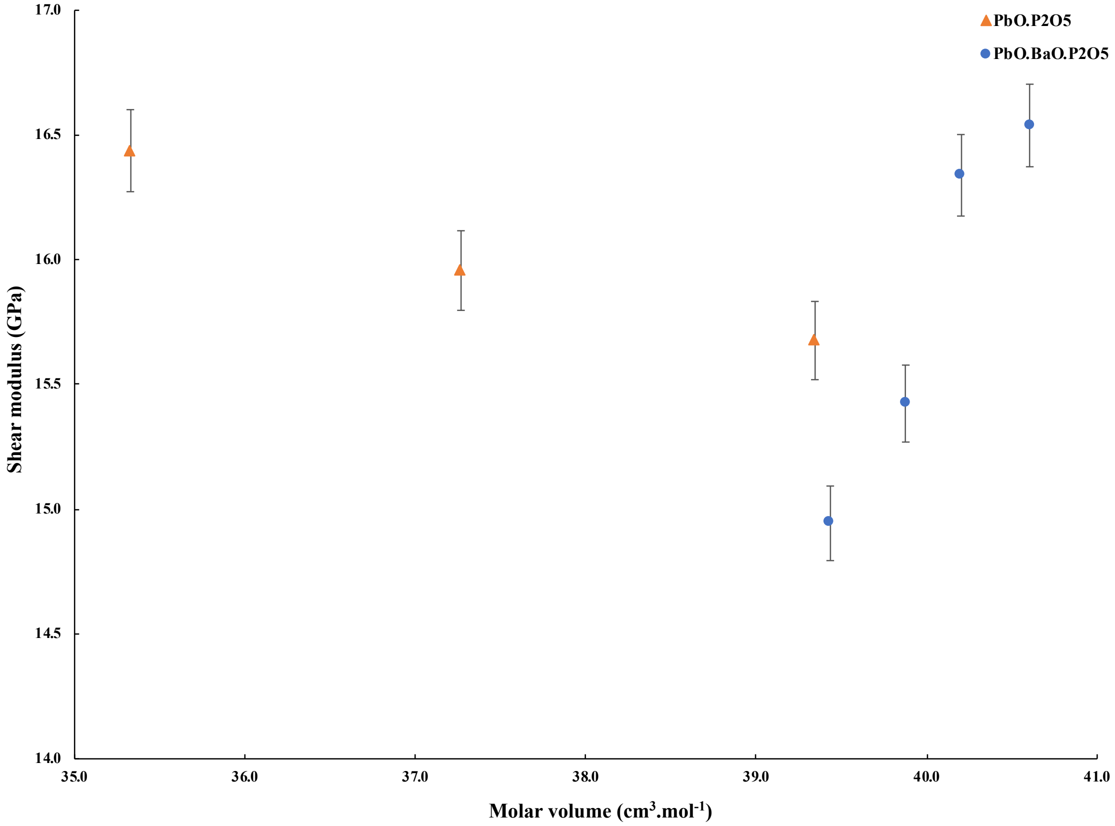

Figure 4.25: Variation of shear modulus G as a function of molar volume V_m for ternary compositions from $(PbO)_{0.10}(BaO)_{40.0}(P_2O_5)_{0.50}$ to $(PbO)_{40.0}(BaO)_{0.10}(P_2O_5)_{0.50}$, and binary compositions from $(PbO)_{0.50}(P_2O_5)_{0.50}$ to $(PbO)_{60.0}(P_2O_5)_{0.40}$

The comparison between Figure 4.24 and Figure 4.25 shows that the correlation between K and V_m is slightly stronger than the one between G and V_m. The different tendencies between K and G with V_m motivates us to determine the correlation between the Poisson ratio and V_m for our compositions. Figure 4.27 shows a clear trend between the Poisson ratio and molar volume of ternary compositions from

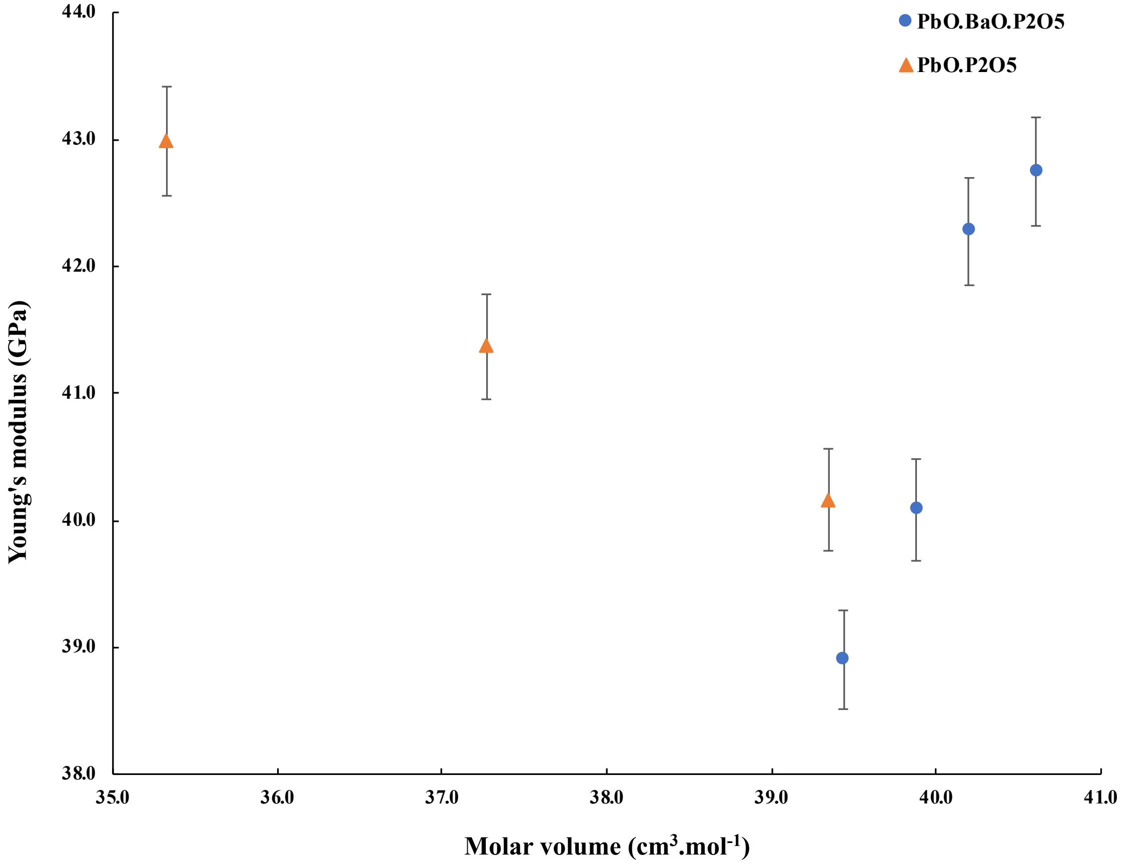

Figure 4.26: Variation of Young's modulus E as a function of molar volume V_m for ternary compositions from $(PbO)_{0.10}(BaO)_{40.0}(P_2O_5)_{0.50}$ to $(PbO)_{40.0}(BaO)_{0.10}(P_2O_5)_{0.50}$, and binary compositions from $(PbO)_{0.50}(P_2O_5)_{0.50}$ to $(PbO)_{60.0}(P_2O_5)_{0.40}$.

$(PbO)_{0.10}(BaO)_{40.0}(P_2O_5)_{0.50}$ to $(PbO)_{40.0}(BaO)_{0.10}(P_2O_5)_{0.50}$, and binary compositions from $(PbO)_{0.50}(P_2O_5)_{0.50}$ to $(PbO)_{60.0}(P_2O_5)_{0.40}$. It was observed in a comprehensive study on various metallic glasses, that glass containing smaller molar volume values possess a larger Poisson ratio [90], which is consistent with our compositions (See Figure 4.27).

Figure 4.28 shows the variation of the Poisson ratio as a function of PbO mol% content. The Poisson ratio increases from 0.281 to 0.308 by increasing the PbO content in our binary compositions and increases from 0.290 to 0.302 in our ternary compositions by replacing BaO with PbO content. Poisson ratio has been found to be correlated with the molar volume (packing density) and network dimensionality of glass.

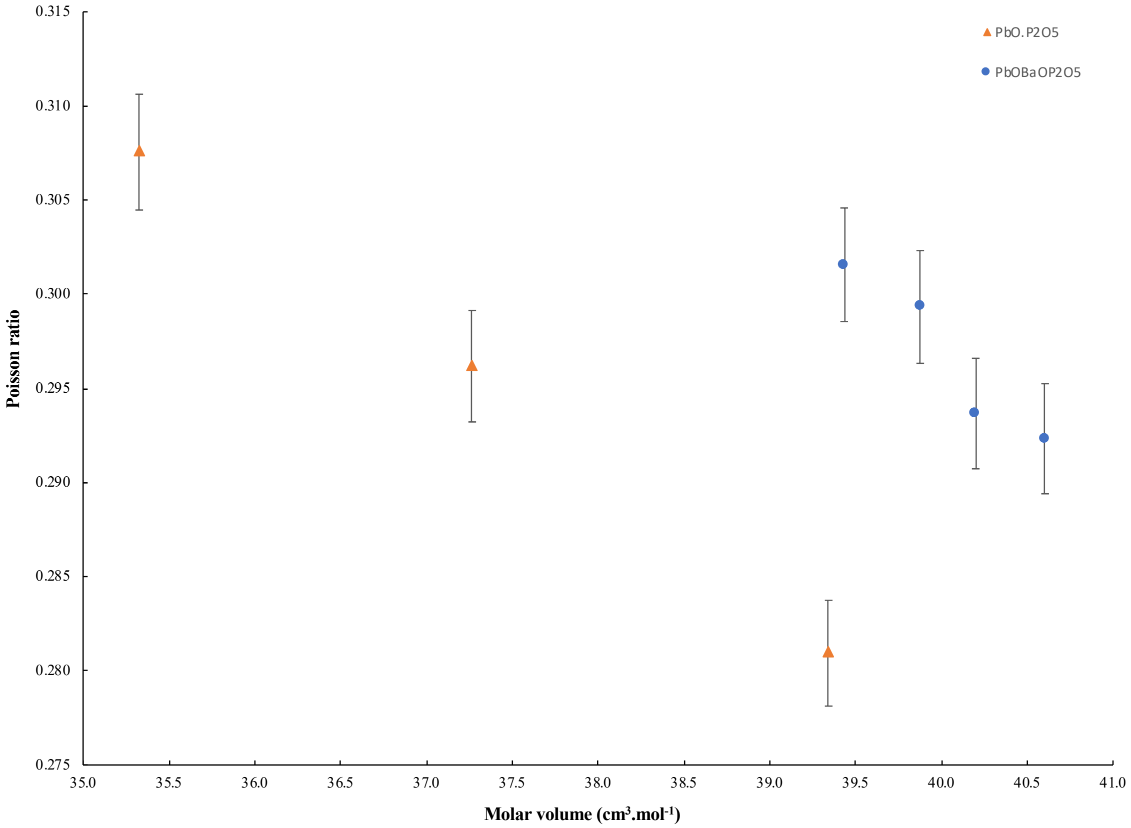

Figure 4.27: Variation of Poisson ratio as a function of molar volume V_m for ternary compositions from $(\mathrm{PbO})_{0.10}(\mathrm{BaO})_{40.0}(\mathrm{P_2O_5})_{0.50}$ to $(\mathrm{PbO})_{40.0}(\mathrm{BaO})_{0.10}(\mathrm{P_2O_5})_{0.50}$, and binary compositions from $(\mathrm{PbO})_{0.50}(\mathrm{P_2O_5})_{0.50}$ to $(\mathrm{PbO})_{60.0}(\mathrm{P_2O_5})_{0.40}$.

Pb cations have a higher field strength and attract the oxygen ions more than Ba cations (Pb-O bond length is shorter than Ba-O one [2]). This gives rise to a decrease in the size of the interstices and a more compact structure which is shown in their molar volume values (See Fig 4.3). Therefore, substituting BaO with PbO content in ternary compositions results in more compact structures and an increase trend of Poisson ratio.

Based on our ^{31}P ssNMR results, the phosphate structure of those glasses with 50 mol% of P_2O_5 content remains the same and expresses the polymer-like chains and rings which corresponds to 2D structure. Based on the previous studies [45, 52], this structure is supposed to possess a Poisson ratio around 0.3 which is consistent with our measured Poisson ratio.

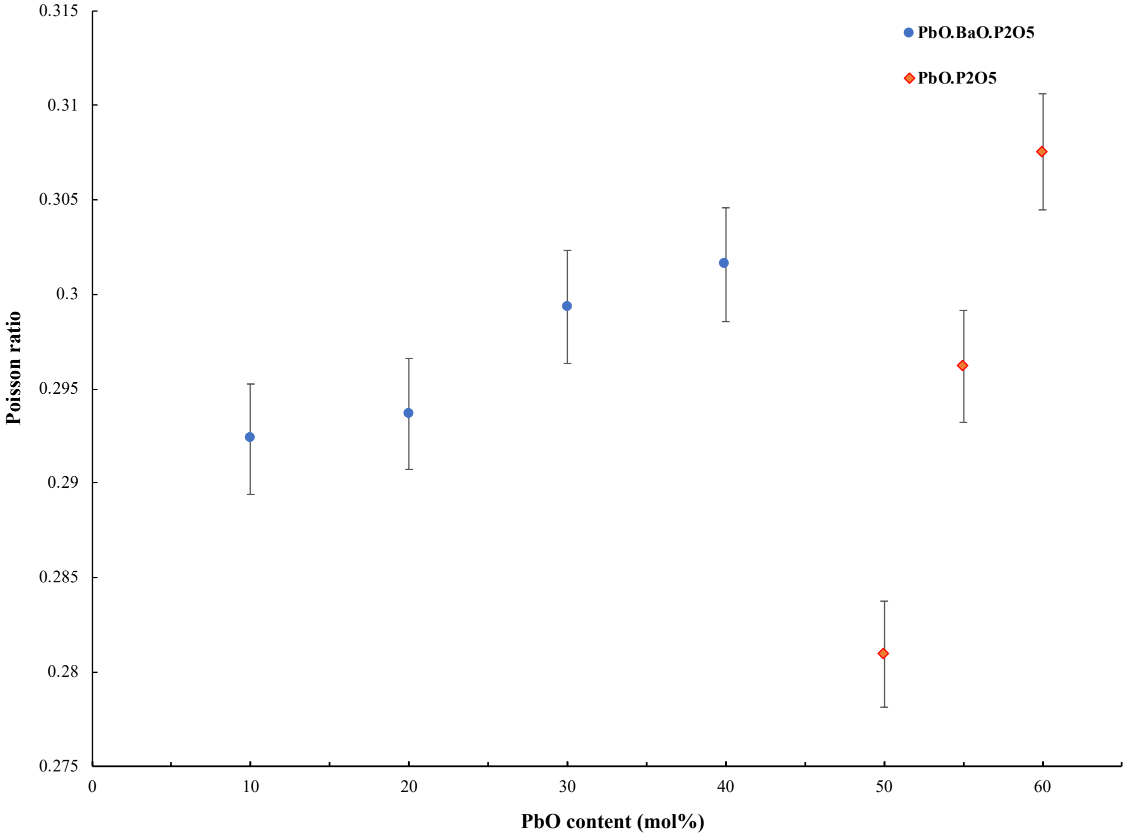

Figure 4.28: Variation of Poisson ratio as a function of PbO content (mol%) in binary and ternary compositions.

4.8 Optical and Photoelastic properties

4.8.1 Refractive Index Measurement

Refractive indices of all samples were measured via ATAGO's multi-wavelength Abbe refractometer (DR-M4/1550) at 656nm described in section 3.8. Table 4.9 lists the glass compositions and their refractive indices which are consistent with the index of refraction values from another investigation on the same compositions [23, 24].

Table 4.9: The glass compositions and index of refraction at 656nm. See also Table 1.1 for abbreviated names.

Compositions	Refractive Index
60Pb40P	1.800
55Pb45P	1.761
50Pb50P	1.697
40Pb10Ba50P	1.692
30Pb20Ba50P	1.667
20Pb30Ba50P	1.640
10Pb40Ba50P	1.610
50Ba50P	1.585
55Ba45P	1.599

It has been proven that an increase in electron density and polarizability of glass constituent ions give rise to an increase in its refractive index [28]. Due to the fact that NBOs are more polarizable than BOs, the addition of PbO or BaO in binary compositions increases their refractive indices. It has been shown that Pb-O has significantly higher polarizability in comparison to Ba-O which can be seen in higher refractive indices of lead phosphate glasses in comparison to the barium phosphate glasses [23]. Therefore, the substitution of BaO with PbO in ternary compositions results in an increasing trend of refractive indices from 1.610 to 1.692.

4.8.2 Stress Optic Measurement

The stress optic coefficient (C) of each sample was determined by the laser based Senarmont method of compensation. Its sign was confirmed by the PS-100 Polariscope which is also known as a light table (detailed description is given in section 3.9). Figure 4.29 depicts a phase shift as a function of applied stress from all trials for the

$(PbO)_{0.60}(P_2O_5)_{0.40}$ glass composition. Based on equation 3.17 as well as the knowledge of λ, d and A of our sample, the stress-optic coefficient is determined from the slope of the phase shift vs applied stress. Due to the high precision but low accuracy of the laser based Senarmont method, the sign of C for each sample was confirmed by the light table.

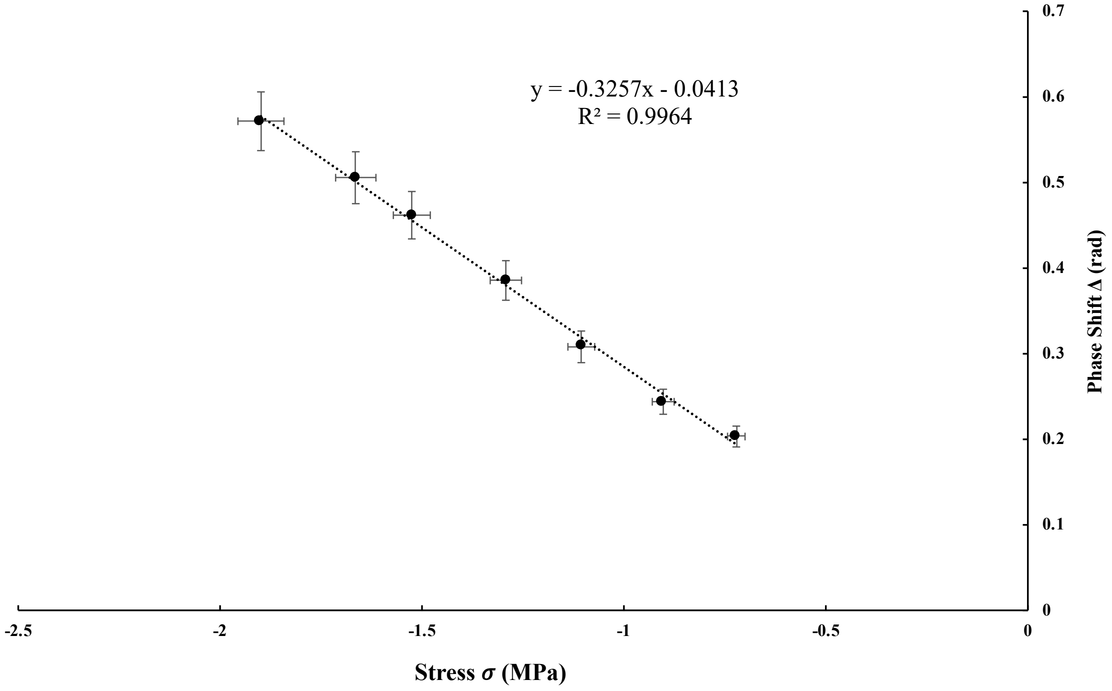

Figure 4.29: Phase shift as a function of applied stress from all trials for $(PbO)_{0.60}(P_2O_5)_{0.40}$ glass composition. Based on equation 3.17, the stress-optic coefficient is determined from the slope of phase shift vs applied stress.

Table 4.10 lists the glass compositions and the value of C of each sample. The sign of C for each sample was consistent with the investigation of Galbraith *et al.* on the same compositions with except to the $(PbO)_{0.40}(BaO)_{10.0}(P_2O_5)_{0.50}$ which shows a negative sign even though it was reported to has a positive value [24]. This contradiction may be rooted in the discrepancy of the compositions of previous investigation. We were able to resolve this discrepancy and a detailed description of this can be seen in section 3.2 and section 4.4. The stress-optic coefficient in binary lead phosphate glasses show a negative trend while a positive trend appears in binary barium phosphate glasses.

Table 4.10: The glass compositions and the stress optic coefficient. Uncertainties are in parentheses. See also Table 1.1 for abbreviated names.

Compositions	C (Brewsters)
60Pb40P	-3.48(7)
55Pb45P	-1.27(8)
50Pb50P	-0.55(6)
40Pb10Ba50P	-0.22(5)
30Pb20Ba50P	+0.13(1)
20Pb30Ba50P	+0.37(5)
10Pb40Ba50P	+0.52(4)
50Ba50P	+0.80(5)
55Ba45P	+0.47(4)

Figure 4.30 shows the variation of the stress-optic coefficient, C, as a function of PbO mol% content. The addition of PbO reduces the stress-optic coefficient of all PbO containing glasses until it yields zero-stress optic composition at x≈35, and ends with a negative stress-optic response.

4.8.3 Empirical model of photoelasticity

The empirical model of photoelasticity can predict the sign of the stress-optic coefficient of glass based on its composition and the structure of its constituents [58]. The focal point of this model is to describe the stress-optic response of glass based on the chemical bonding (anion-cation bond length), d, and the coordination number of its constituent, N_c.

According to this model, glass with a high d/N_c ratio (high metallicity and low coordination number) has a negative or zero stress-optic coefficient, whereas glass with a low d/N_c ratio (lower metallicity and higher coordination number) has a positive stress-optic coefficient. Therefore, the sign of the stress-optic coefficient and the zero-stress optic glass was predicted based on equation 2.27. For glasses with $(d/N_c) > 0.5$ $\mathring{A}$, C has a negative value, whereas glasses with $(d/N_c) \leq 0.5$ $\mathring{A}$ have positive C.

Table 4.11 lists the structural data for each constituents of our glass compositions. The anion-cation bond length (d) is derived from a combination of crystal data and previous literature on structural studies of phosphate-based glass [2, 37]. The coordination number of cations (N_c) was derived from a combination of crystal data and ssNMR results of ^{207}Pb and ^{31}P (see section 4.6.2 and section 4.6.1).

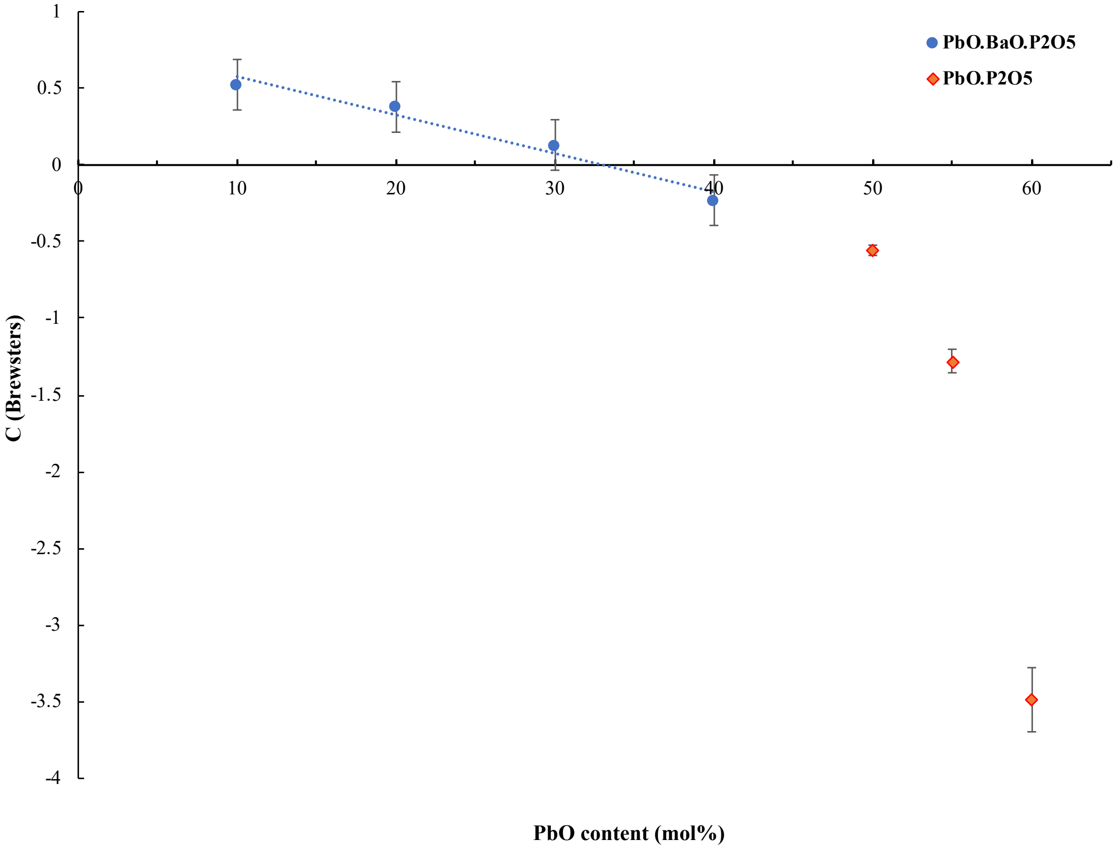

Figure 4.30: Variation of stress-optic coefficient (C) as a function of PbO content for all binary and ternary glass compositions containing PbO.

Table 4.11: Bond lengths (d) are derived from X-ray and neutron diffraction [91, 92], coordination numbers (N_c) are derived from NMR and crystalline compounds [2, 40, 41], and d/N_c ratio for all oxide components of glasses investigated in this work.

Compound	d ($\mathring{A}$)	N_c	d/N_c ($\mathring{A}$)
PbO	2.47(2)	6.5(5)	0.38(3)
BaO	2.79(4)	8	0.349(5)
P_2O_5	1.59(3)	4	0.397(7)

Table 4.12 lists the glass compositions, the average molar d/N_c ratio for stoichiometric families, predicted sign of C (derived from Table 4.11 data and equation 2.27) and the experimental sign of C (derived from Table 4.10).

Table 4.12: The glass compositions, the molar averaged d/N_c ratio for stoichiometric families, predicted sign of C (derived from Table 4.11 data and equation 2.27) and experimental sign of C (derived from Table 4.10). See also Table 1.1 for abbreviated names.

Compositions	<d/N_c> ($\mathring{A}$)	Predicted sign of C	Experimental sign of C
60Pb40P	0.385(18)	+	-
55Pb45P	0.387(16)	+	-
50Pb50P	0.389(13)	+	-
40Pb10Ba50P	0.385(24)	+	-
30Pb20Ba50P	0.381(19)	+	+
20Pb30Ba50P	0.379(16)	+	+
10Pb40Ba50P	0.375(15)	+	+
50Ba50P	0.372(6)	+	+
55Ba45P	0.371(4)	+	+

The empirical model, thus far is consistent with known glass families and it is able to predict the sign of C and zero-stress optic compositions [23, 24, 32, 58, 59]. Typically, the incorporation of better data (coordination number) from ssNMR to the empirical model results in a more accurate prediction of C [31]. For instance, in borate glasses, using a mixture of 3 and 4 coordination number for boron (derived from ssNMR) instead of 3 gives rise to a more accurate prediction of C [32]. However, we observed that the addition of a more accurate coordination number of lead (6 instead of 4) to lead phosphate glasses results in an inaccurate prediction of the sign of C. This implicates that we need to go beyond the empirical model to predict the sign of C for lead phosphate glasses.

Chapter 5

Conclusions and Future Work

The initial goal of this study was to find the correlation between elastic properties, glass structure and compositions. The second goal of this work was to explore the photoelastic properties of our glass families of interest and confirm the reliability of the empirical model for our samples. To achieve these goals, we first examined the correlation between elastic properties and network structures in various types of glasses. It was found that glass elastic properties are strongly correlated to its molar volume (or atomic packing density), interatomic bonding energies, and glass network dimentionality (or coordination number) [45, 90]. To confirm our hypothesis, we explored the local environment of constituent atoms, network compactness and connectivity as well as elastic properties by the use of advanced experimental techniques.

A series of lead phosphate, barium phosphate and lead barium phosphate glass systems were synthesized via the traditional melt and quench technique and their compositions were verified by elemental analysis (WDS). The glass network compactness and connectivity were determined via density measurements which enabled us to derive the molar volume values (described in section 4.5). We then compared our values to molar volume values of their corresponding crystals.

The addition of PbO or BaO followed by a decrease in P_2O_5 content in binary compositions and lead phosphate crystals result in an increase in their densities and a decrease in their molar volume. It is concluded that the incorporation of Pb^{2+} and Ba^{2+} cations alter the glass structure and their corresponding crystalline compounds to have less open space and more compact in structure by the formation of NBOs in the network. Formation of NBOs can also decrease the network connectivity and network dimensionality of the glass structure. In ternary compositions, the substitution of PbO for BaO leads to an increase in their densities and a decrease in their molar volume values. This trend is explained by the fact that lead cations have a higher field strength which allows them to attract the oxygen atoms more so than barium cations.

The ^{31}P ssNMR results (described in section 4.6.1) revealed that the ^{31}P chemical shifts of the individual peaks increase slightly (become less shielded) with the addition of PbO and BaO content in binary compositions. The increase in chemical shifts is explained by a decrease in the average bond order (π-bonding within the P-O bonds), which is caused by the formation of more NBOs as well as the increase in the ionic nature of NBOs [37]. Furthermore, the amount of Q^1 species increases significantly with the addition PbO and BaO content. This variation is caused by the termination of Q^2 units which leads to the depolymerization of the phosphate network. This depolymerization is caused by the creation of NBOs and a progressive reduction in the phosphate chain length [2]. These chains or rings are linked by ionic bonds between Pb or Ba cations and the NBOs. Due to the fact that P_2O_5 content remains constant in all of our ternary compositions, the isotropic chemical shifts and their fraction for both Q^1 and Q^2 units remain approximately similar throughout the samples.

The ^{207}Pb WCPMG ssNMR spectra (depicted in section 4.6.2) indicate that lead acts ionically with a high coordination number (either 6 or 7) which does not evolve with the composition and gives rise to a progressive depolymerization of the phosphate network and a decrease of the Pb-O bond length.

The longitudinal and transverse wave velocities were determined using the ultrasonic method (described in section 4.7). The experimental density values along with v_L and v_T were then used to calculate the elastic properties in each series of glass systems. In binary compositions, their networks are comprised of phosphate chains and rings (Q^2 tetrahedra) which are connected through ionic bonds between Pb or Ba cations and NBOs. The interstitial incorporation of Pb and Ba above 50 mol% followed by the formation of more NBOs leads to a decreases in the average atomic spacing and an increase in the inter-atomic forces during the elastic deformation. This leads to an increase in elastic moduli and Poisson ratio.

In ternary compositions, the elastic moduli decreases by replacing BaO with PbO mol% content, which shows an opposite trend in comparison to the binary samples based on an increasing pattern in their molar volumes. Therefore, it is concluded that although the glass network structure becomes more compact by substitution of PbO with BaO, the inverse effect of molar volume can be compensated by the higher interatomic bonding energy of Ba-O in comparison to Pb-O (U_{oBa-O}(562 kJ/mol) $>$ U_{oPb-O}(382 kJ/mol)) [89]. The Poisson ratio of binary and ternary compositions both confirmed an existing strong correlation between ν and molar volumes [45, 90]. Their correlation indicates that the Poisson ratio increases by increasing the molar volume values (having a less compact and connected structure).

Last but not least, the increase in PbO mol% content in both binary and ternary samples leads to an increase in refractive indices. This is due to the higher level of polarizability in Pb-O and NBOs in comparison to Ba-O and BOs. Furthermore, the incorporation of better data (coordination number) from ssNMR to the empirical model typically results in a more accurate prediction of C [31]. However, we observed that the addition of a more accurate coordination number of lead (6 instead of 4) to lead phosphate glasses results in an inaccurate prediction of the sign of C. This implicates that we need to go beyond the empirical model to predict the sign of C for lead phosphate glasses.

5.1 Future Work

The local environment of lead and phosphorus were investigated with the aid of ^{207}Pb and ^{31}P ssNMR in this study. However, the coordination number of barium was estimated based on their corresponding crystals which can be experimentally confirmed by the synchrotron X-ray or neutron diffraction techniques. Furthermore, due to the X-ray diffraction patterns observed from our samples, there is a possibility of the formation of nanocluser which could be confirmed with the use of scanning electron microscope (SEM). Transmission electron microscope (TEM) could also be employed to observe the nanostructure of glasses and determine whether the samples are homogeneous or physical mixtures. The correlation between elastic properties and glass compositions and structures have been discussed in this dissertation. However, different computational approaches could be implemented in future work to confirm the existing correlation which allows us to predict the properties of glass which have not been produced yet or are toxic to synthesize.

The empirical model of photoelasticity allows us to predict the sign of C and a zero-stress optic glass composition. Due to environmental and safety concerns, use of lead is prohibited in all materials, including glass. In order to produce lead-free zero stress-optic glass, it is essential to confirm the reliability of the empirical model for various types of glass compositions. Therefore, a major field of investigation could be focused on understanding the origin of the empirical model limitation in predicting the sign of C for lead phosphate compositions. Moreover, independent elasto-optic tensor elements (P_{11} and P_{12}) and its correlation to ternary lead barium phosphate compositions can be investigated in the future.

Bibliography

[1] A. Blin, Y. Vaills G. Saout, P. Simon, F. Fayon. Raman and infrared study of $(PbO)_x(P_2O_5)_{(1-x)}$ glasses. *Journal of Raman Spectroscopy*, 33(9):740–746, 2002.

[2] R. K. Brow. Review: the structure of simple phosphate glasses. *Journal of Non-Crystalline Solids*, 263-264:1–28, 2000.

[3] B. C. Sales. Phosphate glasses. *MRS Bulletin*, 12(5):32–35, 1987.

[4] B. Eraiah, S. G. Bhat. Optical properties of samarium doped zinc–phosphate glasses. *Journal of Physics and Chemistry of Solids*, 68(4):581–585, 2007.

[5] G. Gongyi, C. Yuli. Formation and properties of a lead-barium-aluminum phosphate glass. *Journal of the American Ceramic Society*, 78(2):501–503, 1995.

[6] Kh. A. Matori, M. H. M. Zaid, S. H. A. Aziz, H. M. Kamari, Z. A. Wahab. Study of the elastic properties of $(PbO)_x(P_2O_5)_{1-x}$ lead phosphate glass using an ultrasonic technique. *Journal of Non-Crystalline Solids*, 361:78–81, 2013.

[7] L. L. Hench, R. J. Splinter, W. C. Allen, T. K. Greenlee. Bonding mechanisms at the interface of ceramic prosthetic materials. *Journal of Biomedical Materials Research*, 5(6):117–141, 1971.

[8] I. W. Donald. Immobilisation of radioactive and non-radioactive wastes in glass-based systems: an overview. *Glass technology*, 48(4):155–163, 2007.

[9] M. Ojovan, W. E. Lee, S. N. Kalmykov. *An introduction to nuclear waste immobilisation*. Elsevier, 2019.

[10] T. Y. Wei, Y. Hu, L. G. Hwa. Structure and elastic properties of low-temperature sealing phosphate glasses. *Journal of Non-Crystalline Solids*, 288(1-3):140–147, 2001.

[11] M. I. Abd El-Ati. Electrical conductivity and optical properties of gamma-irradiated niobium phosphate glasses. *Journal of Materials Science*, 35(24):6175–6180, 2000.

[12] V. Sudarsan, S. K. Kulshreshtha. Study of structural aspects of $PbO–P_2O_5–Sb_2O_3$ glasses. *Journal of Non-Crystalline Solids*, 286(1-2):99–107, 2001.

[13] D. J. Thompson, M. A. Salim, A. B. Hallak, M. A. Daous G. D. Khattak, E. E. Khawaja, L. E. Wenger. Composition-dependent loss of phosphorus in the formation of transition-metal phosphate glasses. *Journal of Non-Crystalline Solids*, 194(1-2):1–12, 1996.

[14] B. Eraiah, M. G. Smitha, R. V. Anavekar. Elastic properties of lead-phosphate glasses doped with samarium trioxide. *Journal of Physics and Chemistry of Solids*, 71(3):153–155, 2010.

[15] Ch. Srinivasa Rao, K. Upendra Kumar, P. Babu, C. K. Jayasankar. Optical properties of Ho^{3+} ions in lead phosphate glasses. *Optical Materials*, 35(2):102–107, 2012.

[16] O. Cozar, D. A. Magdas, L. Nasdala, I. Ardelean, G. Damian. Raman spectroscopic study of some lead phosphate glasses with tungsten ions. *Journal of Non-Crystalline Solids*, 352(28):3121 – 3125, 2006.

[17] P. Y. Shih. Properties and FTIR spectra of lead phosphate glasses for nuclear waste immobilization. *Materials Chemistry and Physics*, 80(1):299–304, 2003.

[18] C. Dayanand, G. Bhikshamaiah, V. J. Tyagaraju, M. Salagram, A. S. R. Murthy. Structural investigations of phosphate glasses: a detailed infrared study of the $(PbO)_x - (P_2O_5)_{1-x}$ vitreous system. *Journal of Materials Science*, 31(8):1945–1967, 1996.

[19] G. Saout, P. Simon, F. Fayon, A. Blin, Y. Vaills. A multispectroscopic study of $PbO_xZnO_{0.6-x}(P_2O_5)_{0.4}$ glasses. *Journal of Non-Crystalline Solids*, 293-295:657–662, 2001.

[20] M. H. Kharita, R. Jabra, S. Yousef, T. Samaan. Shielding properties of lead and barium phosphate glasses. *Radiation Physics and Chemistry*, 81(10):1568–1571, 2012.

[21] M. H. Misbah, H. Doweidar, K. El-Egili, G. El-Damrawi, M. El-Kemary. Structure and some properties of $xBaO.(50-x)PbO50P_2O_5$ glasses. *Journal of Non-Crystalline Solids*, 534:119945, 2020.

[22] M. Guignard, L. Albrecht, J. W. Zwanziger. Zero-stress optic glass without lead. *Chemistry of Materials*, 19(2):286–290, 2007.

[23] M. Aldridge, J. Kieffer J. Galbraith, L. Chapman, J. W. Zwanziger. Elasto-optic coefficients of borate, phosphate, and silicate glasses: Determination by brillouin spectroscopy. *The Journal of Physical Chemistry C*, 120(38):21802–21810, 2016.

[24] J. Galbraith, J. W. Zwanziger. Designing glass with non-dispersive stress-optic response. *Journal of Non-Crystalline Solids*, 433:82–86, 2016.

[25] H. H. Paetsch. *Untersuchungen über das System* $PbO\text{-}SiO_2\text{-}P_2O_5$. PhD thesis, 1955.

[26] R. A McCauley, F. A. Hummel. Phase relations in a portion of the system barium oxide-phosphorus pentoxide. *Transactions of the British Ceramic Society*, 67:619–628, 1968.

[27] A. K. Varshneya. *Fundamentals of Inorganic Glasses.* Academic Press, New York, 1994.

[28] J. E. Shelby. *Introduction to Glass Science and Technology.* Royal Society of Chemistry, 2007.

[29] H. Scholze. *Glass: Nature, Structure and Properties.* Springer-Verlag, New York, 1991.

[30] W. H. Zachariasen. The atomic arrangement in glass. *Journal of the American Chemical Society*, 54(10):3841–3851, 1932.

[31] V. Martin. *Composition and structure dependence of the photoelastic response of oxide glass.* Dalhousie University, Halifax, Nova Scotia, Canada, 2011.

[32] V. Martin, B. Wood, U. Werner-Zwanziger, J. W. Zwanziger. Structural aspects of the photoelastic response in lead borate glasses. *Journal of Non-Crystalline Solids*, 357(10):2120–2125, 2011.

[33] T. Takaishi, J. Jin, T. Uchino, T. Yoko. Structural study of PbO-B_2O_3 glasses by X-ray diffraction and ^{11}B MAS NMR techniques. *Journal of the American Ceramic Society*, 83(10):2543–2548, 2004.

[34] D. W. J. Cruickshank. The rôle of 3d-orbitals in π bonds between (a) silicon, phosphorus, sulphur, or chlorine and (b) oxygen or nitrogen. *J. Chem. Soc.*, pages 5486–5504, 1961.

[35] J. R. Van Wazer. *Phosphorus and its Compounds*, volume 1. Interscience, New York, 1958.

[36] P. Losso, B. Schnabel, C. Jäger, U. Sternberg, D. Stachel, D. O. Smith. ^{31}P NMR investigations of binary alkaline earth phosphate glasses of ultra phosphate composition. *Journal of Non-Crystalline Solids*, 143:265 – 273, 1992.

[37] R. K. Brow, D. R. Tallant, J. J. Hudgens, S. W. Martin, A. D. Irwin. The short-range structure of sodium ultraphosphate glasses. *Journal of Non-Crystalline Solids*, 177:221–228, 1994.

[38] T. M. Alam, R. K. Brow. Local structure and connectivity in lithium phosphate glasses: a solid-state ^{31}P MAS NMR and 2D exchange investigation. *Journal of Non-Crystalline Solids*, 223(1-2):1–20, 1998.

[39] J. C. Boyat, M. T. A. Pouchot, J. C. Guitel. Structure cristalline du polyphosphate de baryum γ: $Ba(PO_3)$. *Acta Crystallographica Section B: Structural Crystallography and Crystal Chemistry*, 34(9):2689–2692, 1978.

[40] D. Zakaria, F. Erragh, A. Oudahmane, M. El-Ghozzi, D. Avignant. α-$Ba_2P_2O_7$. *Acta Crystallographica Section E*, 66(11):76–77, 2010.

[41] K. H. Jost. Die Struktur des Bleipolyphosphats $[Pb(PO_3)_2]_x$ und allgemeiner Überblick über Polyphosphatstrukturen. *Acta Crystallographica*, 17(12):1539–1544, 1964.

[42] D. F. Mullica, H. O. Perkins, D. A. Grossie, L. A. Boatner, B. C. Sales. Structure of dichromate-type lead pyrophosphate, $Pb_2P_2O_7$. *Journal of Solid State Chemistry*, 62(3):371 – 376, 1986.

[43] A. Elmarzouki, A. Boukhari, E. M. Holt, A. Berrada. Structural order in complexes of the $A^{II}B^{II}P_2O_7$ series: $BaPbP_2O_7$, $PbCoP_2O_7$, $PbMnP_2O_7$ and $PbCuP_2O_7$. *Journal of Alloys and Compounds*, 227(2):125 – 130, 1995.

[44] L. Wondraczek, J. C. Mauro, J. Eckert, U. Kühn, J. Horbach, J. Deubener, T. Rouxel. Towards ultrastrong glasses. *Advanced Materials*, 23(39):4578–4586, 2011.

[45] T. Rouxel. Elastic properties and short-to medium-range order in glasses. *Journal of the American Ceramic Society*, 90(10):3019–3039, 2007.

[46] G. N. Greaves. EXAFS and the structure of glass. *Journal of Non-Crystalline Solids*, 71(1-3):203–217, 1985.

[47] A. Makishima, J. D. Mackenzie. Direct calculation of Young's modulus of glass. *Journal of Non-Crystalline Solids*, 12(1):35–45, 1973.

[48] R. D. Shannon, C. T. Prewitt. Effective ionic radii in oxides and fluorides. *Acta Crystallographica Section B Structural Crystallography and Crystal Chemistry*, 25(5):925–946, 1969.

[49] W. F. Hosford. *Mechanical behavior of materials.* Cambridge University Press, 2010.

[50] K. H. Sun. Fundamental condition of glass formation. *Journal of the American Ceramic Society*, 30(9):277–281, 1947.

[51] A. Makishima , J. D. Mackenzie. Calculation of bulk modulus, shear modulus and Poisson's ratio of glass. *Journal of Non-Crystalline Solids*, 17(2):147–157, 1975.

[52] B. Bridge, N. D. Patel, D. N. Waters. On the elastic constants and structure of the pure inorganic oxide glasses. *Physica Status Solidi (a)*, 77(2):655–668, 1983.

[53] J. H. Konnert, J. Karle, G. A. Ferguson. Crystalline ordering in silica and germania glasses. *Science*, 179(4069):177–179, 1973.

[54] H. G. Jerrard. Optical compensators for measurement of elliptical polarization. *Journal of the Optical Society of America*, 38(1):35, 1948.

[55] H. J. Hoffman. *The Properties of Optical Glass.* Springer, 1998.

[56] H. Mueller. The theory of photoelasticity. *Journal of the American Ceramic Society*, 21(1):27–33, 1938.

[57] T. Komatsu R. Yokota K. Matusita, Ch. Ihara. Photoelastic effects in silicate glasses. *Journal of the American Ceramic Society*, 67(10):700–704, 1984.

[58] M. Guignard, L. Albrecht, J. W. Zwanziger. Zero-stress optic glass without lead. *Chemistry of Materials*, 19(2):286–290, 2007.

[59] N. Yamamoto, A. Saitoh, H. Takebe. Zero photoelastic zinc tin phosphate glass without lead oxide. *Optics Letters*, 37(20):4203, 2012.

[60] L. Reimer. Scanning electron microscopy: Physics of image formation and microanalysis, second edition. *Measurement Science and Technology*, 11(12):1826–1826, 2000.

[61] R. F. Egerton. Physical Principles of Electron Microscopy. 2005.

[62] K. P. Severin. *Energy Dispersive Spectrometry of Common Rock Forming Minerals*. Springer-Verlag GmbH, 2005.

[63] J. I. Goldstein, D. E. Newbury, D. C. Joy, C. E. Lyman, P. Echlin, E. Lifshin. *Scanning Electron Microscopy and X-Ray Microanalysis*. Springer US, 2003.

[64] W. H. Bragg, W. L. Bragg. The reflection of X-rays by crystals. *Proceedings of the Royal Society A: Mathematical, Physical and Engineering Sciences*, 88(605):428–438, 1913.

[65] R. H. Perry. *Perry's Chemical Engineers Handbook*. McGraw Hill, New York, 6 edition, 1984.

[66] P. Paufler. Physical properties of Crystals. *Crystal Research and Technology*, 21(12):1508–1508, 1986.

[67] R. E. Newnham. *Properties of Materials: Anisotropy, Symmetry, Structure*. Oxford University Press, 2004.

[68] W. Voigt. *Lehrbuch Der Kristallphysik (mit Ausschluss Der Kristalloptik)*. Leipzig, Berlin, B. G. Teubner, 1910.

[69] E. R. Andrew. Magic angle spinning. *International Reviews in Physical Chemistry*, 1(2):195–224, 1981.

[70] M. Feike, D. Demco, R. Graf, J. Gottwald, S. Hafner, H. W. Spiess. *J. Magn. Reson. A*, 122:214, 1996.

[71] E. L. Hahn. Spin echoes. *Phys. Rev.*, 80:580–594, 1950.

[72] H. Y. Carr, E. M. Purcell. Effects of diffusion on free precession in nuclear magnetic resonance experiments. *Phys. Rev.*, 94:630–638, 1954.

[73] S. Meiboom, D. Gill. Modified spin-echo method for measuring nuclear relaxation times. *Review of Scientific Instruments*, 29(8):688–691, 1958.

[74] L. A. O'Dell, R. W. Schurko. QCPMG using adiabatic pulses for faster acquisition of ultra-wideline NMR spectra. *Chemical Physics Letters*, 464(1-3):97–102, 2008.

[75] E. Kupce, R. Freeman. Adiabatic pulses for wideband inversion and broadband decoupling. *Journal of Magnetic Resonance, Series A*, 115(2):273 – 276, 1995.

[76] E. Kupce, R. Freeman. Stretched adiabatic pulses for broadband spin inversion. *Journal of Magnetic Resonance, Series A*, 117(2):246–256, 1995.

[77] R. W. Schurko. Ultra-wideline solid-state NMR spectroscopy. *Accounts of Chemical Research*, 46(9):1985–1995, 2013.

[78] A. Mede, V. Frydman, L. Frydman. Central transition nuclear magnetic resonance in the presence of large quadrupole couplings: Cobalt-59 nuclear magnetic resonance of Cobaltophthalocyanines . *The Journal of Physical Chemistry A*, 103(25):4830–4835, 1999.

[79] D. Massiot, F. Fayon, M. Capron, I. King, S. Calve, B. Alonso, J. Durand, B. Bujoli, Z. Gan, G. Hoatson. Modelling one- and two-dimensional solid-state NMR spectra. *Magnetic Resonance in Chemistry*, 40(1):70–76, 2001.

[80] F. Fayon, C. Bessada, J. Coutures, D. Massiot. High-resolution double-quantum ^{31}P MAS NMR study of the intermediate-range order in crystalline and glass lead phosphates. *Inorganic Chemistry*, 38(23):5212–5218, 1999.

[81] S. Prabhakar, K. J. Rao, C. N. R. Rao. A magic-angle spinning ^{31}P NMR. *Chemical Physics Letters*, (1):96 – 102.

[82] F. Fayon, C. Bessada, A. Douy, D. Massiot. Chemical bonding of lead in glasses through isotropic vs anisotropic correlation: PASS shifted echo. *Journal of Magnetic Resonance*, 137(1):116–121, 1999.

[83] F. Fayon, I. Farnan, C. Bessada, J. Coutures, D. Massiot, J. P. Coutures. Empirical correlations between ^{207}Pb NMR chemical shifts and structure in solids. *Journal of the American Chemical Society*, 119(29):6837–6843, 1997.

[84] J. L. Shaw, U. Werner-Zwanziger, J. W. Zwanziger. Correlation of lead borate glass structure with photoelastic response. *Physics and Chemistry of Glasses*, 47:513–517, 2006.

[85] J. M. Gibson, F. G. Vogt, A. S. Barnes, K. T. Mueller. Investigation of lead borosilicate glass structure with ^{207}Pb and ^{11}B solid-state NMR. *MRS Proceedings*, 658:22, 2000.

[86] G. N. Greaves, S. J. Gurman, L. F. Gladden, C. A. Spence, P. Cox, B. C. Sales, L. A. Boatner, R. N. Jenkins. A structural basis for the corrosion resistance of lead-iron-phosphate glasses: An X-ray absorption spectroscopy study. *Philosophical Magazine B*, 58(3):271–283, 1988.

[87] L. E. Kinsler, A. R. Frey, A. B. Coppens, J. V. Sanders. *Fundamentals of acoustics.* New York : Wiley, 2000.

[88] T. Courtney. *Mechanical Behavior of Materials.* McGraw-Hill Education, 2000.

[89] D. R. Lide. *Handbook of Chemistry and Physics.* Taylor Francis, New York, 2005-2006.

[90] W. H. Wang. The elastic properties, elastic models and elastic perspectives of metallic glasses. *Progress in Materials Science*, 57(3):487 – 656, 2012.

[91] U. Hoppe, G. Walter, D. Stachel, A. Hannon. Short-range order details of metaphosphate glasses studied by pulsed neutron scattering. *Zeitschrift für Naturforschung A*, 50:684–692, 1995.

[92] U. Hoppe, D. Stachel, D. Beyer. The oxygen coordination of metal ions in phosphate and silicate glasses studied by a combination of x-ray and neutron diffraction. *Physica Scripta*, T57:122–126, 1995.

5.2 Appendix A Copyright Permission

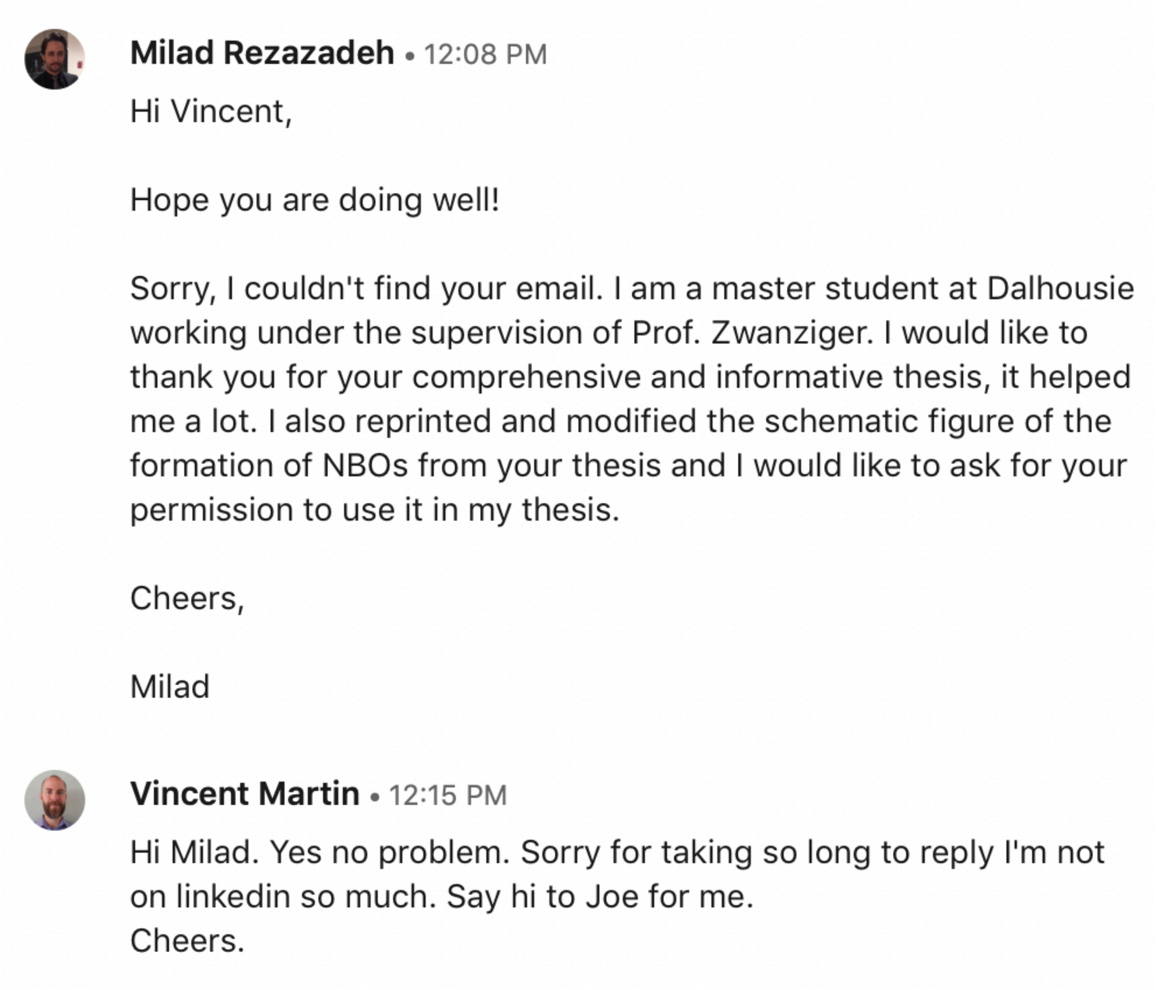

Milad Rezazadeh • 12:08 PM

Hi Vincent,

Hope you are doing well!

Sorry, I couldn't find your email. I am a master student at Dalhousie working under the supervision of Prof. Zwanziger. I would like to thank you for your comprehensive and informative thesis, it helped me a lot. I also reprinted and modified the schematic figure of the formation of NBOs from your thesis and I would like to ask for your permission to use it in my thesis.

Cheers,

Milad

Vincent Martin • 12:15 PM

Hi Milad. Yes no problem. Sorry for taking so long to reply I'm not on linkedin so much. Say hi to Joe for me.
Cheers.

Figure 5.1: Permission to reproduce Figure 2.3.

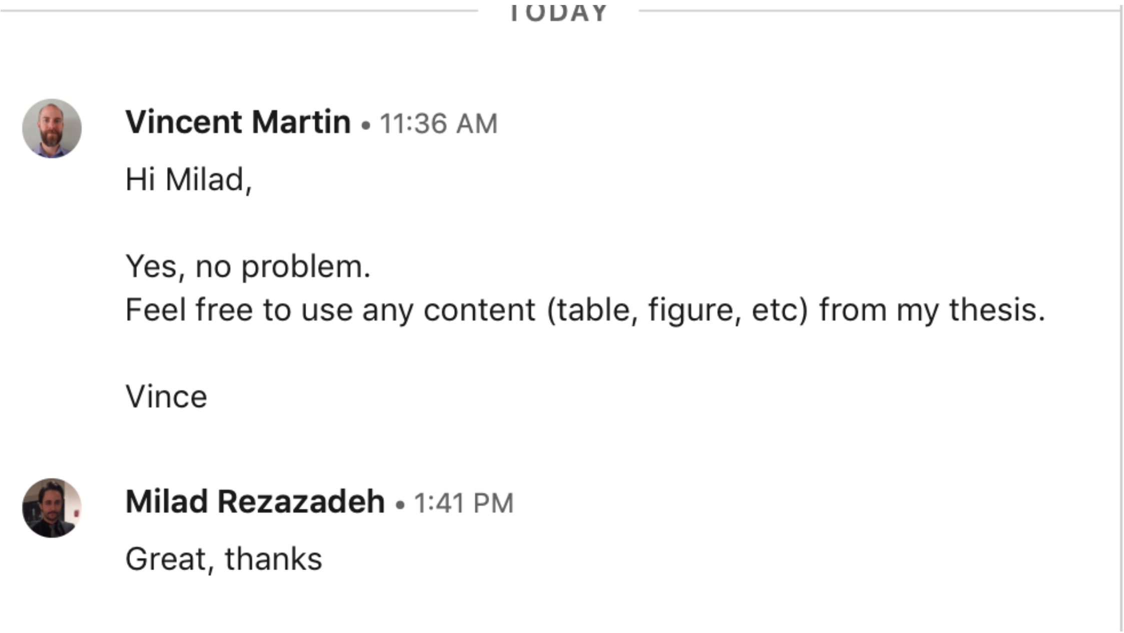

Vincent Martin • 11:36 AM

Hi Milad,

Yes, no problem.
Feel free to use any content (table, figure, etc) from my thesis.

Vince

Milad Rezazadeh • 1:41 PM

Great, thanks

Figure 5.2: Permission to reproduce Figure 3.4 and Figure 3.7.